



National Library  
of Canada

Bibliothèque nationale  
du Canada

Canadian Theses Service

Services des thèses canadiennes

Ottawa, Canada  
K1A 0N4

## CANADIAN THESES

### NOTICE

The quality of this microfiche is heavily dependent upon the quality of the original thesis submitted for microfilming. Every effort has been made to ensure the highest quality of reproduction possible.

If pages are missing, contact the university which granted the degree.

Some pages may have indistinct print especially if the original pages were typed with a poor typewriter ribbon or if the university sent us an inferior photocopy.

Previously copyrighted materials (journal articles, published tests, etc.) are not filmed.

Reproduction in full or in part of this film is governed by the Canadian Copyright Act, R.S.C. 1970, c. C-30.

**THIS DISSERTATION  
HAS BEEN MICROFILMED  
EXACTLY AS RECEIVED**

## THÈSES CANADIENNES

### AVIS

La qualité de cette microfiche dépend grandement de la qualité de la thèse soumise au microfilmage. Nous avons tout fait pour assurer une qualité supérieure de reproduction.

S'il manque des pages, veuillez communiquer avec l'université qui a conféré le grade.

La qualité d'impression de certaines pages peut laisser à désirer, surtout si les pages originales ont été dactylographiées à l'aide d'un ruban usé ou si l'université nous a fait parvenir une photocopie de qualité inférieure.

Les documents qui font déjà l'objet d'un droit d'auteur (articles de revue, examens publiés, etc.) ne sont pas microfilmés.

La reproduction, même partielle, de ce microfilm est soumise à la Loi canadienne sur le droit d'auteur, SRC 1970, c. C-30.

**LA THÈSE A ÉTÉ  
MICROFILMÉE TELLE QUE  
NOUS L'AVONS REÇUE**

THE UNIVERSITY OF ALBERTA

Evaluation of the Combustibility of  
Hydropyrolysis Chars

by

Kevin J. Knill

A Thesis

Submitted to the Faculty of Graduate Studies and Research in partial fulfillment  
of the requirements for the degree of Master's of Science

Department of Mechanical Engineering

Edmonton, Alberta

Spring 1987

Permission has been granted to the National Library of Canada to microfilm this thesis and to lend or sell copies of the film.

The author (copyright owner) has reserved other publication rights, and neither the thesis nor extensive extracts from it may be printed or otherwise reproduced without his/her written permission.

L'autorisation a été accordée à la Bibliothèque nationale du Canada de microfilmer cette thèse et de prêter ou de vendre des exemplaires du film.

L'auteur (titulaire du droit d'auteur) se réserve les autres droits de publication; ni la thèse ni de longs extraits de celle-ci ne doivent être imprimés ou autrement reproduits sans son autorisation écrite.

ISBN 0-315-37768-2

# THE UNIVERSITY OF ALBERTA

## RELEASE FORM

*NAME OF AUTHOR:* Kevin James Knill

*TITLE OF THESIS:* Evaluation of the Combustibility of Hydropyrolysis Chars.

*DEGREE:* Master's of Science

*YEAR THIS DEGREE WAS GRANTED:* 1987

Permission is hereby granted to THE UNIVERSITY OF ALBERTA to reproduce single copies of this thesis and to lend or sell such copies for private, scholarly or scientific research purposes only.

The author reserves other publication rights, and neither the thesis nor extensive extracts from it may be printed or otherwise reproduced without the author's written permission.

Kevin Knill


(Student's signature)

5112 112 Street

Edmonton, Alberta, T6H 3J2

THE UNIVERSITY OF ALBERTA  
FACULTY OF GRADUATE STUDIES AND  
RESEARCH

The undersigned certify that they have read, and recommend to the Faculty of Graduate Studies and Research for acceptance, a thesis entitled Evaluation of the Combustibility of Hydropyrolysis Chars submitted by Kevin J. Knill in partial fulfilment of the requirements for the degree of Master's of Science.

  
(Supervisor)

2 

3 

4 

Date: January 7, 1987

# Abstract

Hydropyrolysis is the thermal fragmentation of high molecular weight compounds in the presence of high pressure hydrogen. When coal is hydropyrolysed, the volatile matter is simultaneously released and upgraded to light hydrocarbon liquids and gases, leaving a solid char. The hydropyrolysis of Alberta subbituminous coal has been investigated at the Alberta Research Council. In those experiments, char was the single major product representing 37 - 74% of the total yield. In order to ensure efficient utilization of the char, its combustion properties were evaluated in the present work to determine its suitability as a makeup fuel in a utility boiler.

The chemical oxidation reactivities of several chars were measured by thermogravimetric analysis at 600 - 650K. The intrinsic reactivity of the chars was unaffected by hydropyrolysis conditions. However, residual volatile matter present in some chars had an order of magnitude higher oxidation reactivity than the carbon residue.

The combustibility of chars was measured in an entrained flow combustor, operated at 1025 - 1335K. Chars with volatile matter content higher than 15% burned as rapidly as the parent coal. Chars with low volatile matter content also

burned rapidly if a large internal surface area was developed during hydrolysis.

Detailed surface characterization of several chars showed that sufficient internal surface area was only developed in chars processed at the highest conditions of hydrolysis temperature, hydrogen pressure and residence time.

It was concluded from the combustibility data that some chars may be suitable as makeup fuels in a utility boiler. The suitable chars would have volatile matter content in excess of 15%, or they would contain high internal surface area on which the oxidation reaction could be initiated. Further char combustion testing at larger scale in experimental units representative of full scale boilers was recommended in order to validate these conclusions.

# Acknowledgements

The author would like to thank the many individuals whose work has made this thesis possible. In particular, Donald Ungarian conducted all of the thermogravimetric analyses and combustibility tests. Ron Zacharkiw and Kim Nesbitt conducted the char particle characterization. Allan Chamberlain and John Mendiuk were responsible for the hydrolysis program and the char preparation. Prof. J. B. Dale reviewed the technical content of the thesis. Lori Wolff typed and Anna Knill reviewed the manuscript.

The author also gratefully acknowledges the financial support of the Alberta Research Council and the Alberta/Canada Energy Resources Research Fund administered by the Office of Coal Research and Technology of Alberta Energy. The author also acknowledges Petro Canada for supplying the mercury porosimeter and the Coal Technology Information Center maintained by the Alberta Research Council for collecting the relevant literature.



# Contents

|          |   |          |
|----------|---|----------|
| <b>1</b> | <b>Introduction</b>   | <b>1</b> |
| 1.1      | The ARC Hydropyrolysis Process . . . . .                      | 2        |
| 1.2      | Chemical Properties of Char Pertinent to Combustion . . . . . | 7        |
| 1.2.1    | Evaluation Criteria . . . . .                                 | 7        |
| 1.2.2    | Hydropyrolysis Char Properties . . . . .                      | 9        |
| 1.3      | Char Surface Characterization . . . . .                       | 12       |
| 1.3.1    | Description of Measurement Techniques . . . . .               | 12       |
| 1.3.2    | Coal and Char Surface Structure . . . . .                     | 18       |
| 1.4      | Evaluation of Coal and Char Combustibility . . . . .          | 21       |
| 1.4.1    | Pilot Scale Experiments . . . . .                             | 21       |
| 1.4.2    | Laboratory Scale Experiments . . . . .                        | 28       |
| 1.5      | Combustion Mechanisms . . . . .                               | 34       |
| 1.5.1    | Oxidation Reaction . . . . .                                  | 35       |
| 1.5.2    | Diffusion Effects . . . . .                                   | 38       |
| 1.5.3    | Controlling Mechanism . . . . .                               | 47       |
| 1.6      | Objectives of the Research . . . . .                          | 48       |

|   |            |
|---|------------|
| 1.7 Point of Departure . . . . .  | 48         |
| <b>2 Method Development</b>   | <b>50</b>  |
| 2.1 Surface Characterization . . . . .                                  | 50         |
| 2.2 Intrinsic Oxidation Reactivity - Thermogravimetric Analysis . . . . | 64         |
| 2.3 Combustibility - Entrained Flow Combustor Development . . . . .     | 71         |
| <b>3 Results and Discussion</b>   | <b>86</b>  |
| 3.1 Char Surface Characterization . . . . .                             | 86         |
| 3.2 Char Intrinsic Oxidation Reactivity . . . . .                       | 93         |
| 3.2.1 Nature of the TGA Oxidation . . . . .                             | 93         |
| 3.2.2 Intrinsic Char Chemical Reactivity . . . . .                      | 103        |
| 3.3 Char Combustibility . . . . .                                       | 108        |
| 3.4 Comparison of TGA and EFC Results . . . . .                         | 113        |
| 3.4.1 Average Pore Radius Model . . . . .                               | 114        |
| 3.4.2 Distributed Pore Size Model . . . . .                             | 115        |
| 3.5 Comparison with Previous Work . . . . .                             | 123        |
| <b>4 Conclusions</b>  | <b>124</b> |
| <b>5 Recommendations</b>  | <b>126</b> |
| <b>References</b>   | <b>127</b> |
| <b>A Statistical Analysis of Nitrogen Surface Area Technique</b>        | <b>138</b> |
| <b>B Oxidant Diffusion Limitations in the TGA</b>                       | <b>141</b> |

## **C Surface Characterization Data**

**144**

# List of Tables

|     |  |     |
|-----|--|-----|
| 1.1 | Range of Hydropyrolysis Product Yields . . . . .   | 4   |
| 1.2 | Variation of Hydropyrolysis Char Analyses . . . . .  | 10  |
| 1.3 | Operating Conditions for Select Coal Conversion Processes . . . . .                          | 22  |
| 1.4 | Ultimate and Proximate Analyses and N <sub>2</sub> Surface Area of Select<br>Chars . . . . . | 26  |
| 2.1 | Typical Mercury Porosimetry Data for Hydropyrolysis Chars . . . . .                          | 55  |
| 3.1 | Hydropyrolysis Char Process Conditions . . . . .   | 87  |
| 3.2 | Surface Characteristics of Hydropyrolysis Chars . . . . .                                    | 88  |
| 3.3 | Hydropyrolysis Char Pore Structural Parameters . . . . .                                     | 100 |
| 3.4 | Calculated Char Reaction Rates Using the Average Pore Size Model                             | 115 |
| 3.5 | Comparison of Calculated and Measured Char Combustion Rates .                                | 120 |
| A.1 | Statistical Parameters of the Surface Area Test . . . . .                                    | 139 |
| A.2 | ANOVA Table for Surface Area Test . . . . .  | 139 |
| C.1 | Nitrogen and Carbon Dioxide Surface Area Measurements . . . . .                              | 145 |
| C.2 | Mercury Porosimetry Data for Alberta Coal . . . . .  | 146 |

|   |     |
|---|-----|
| C.3 Mercury Porosimetry Data for Char A | 147 |
| C.4 Mercury Porosimetry Data for Char B | 148 |
| C.5 Mercury Porosimetry Data for Char C | 149 |
| C.6 Mercury Porosimetry Data for Char D | 150 |
| C.7 Mercury Porosimetry Data for Char E | 151 |
| C.8 Mercury Porosimetry Data for Char F | 152 |
| C.9 Mercury Porosimetry Data for Char G | 153 |

# List of Figures

|      |   |    |
|------|---|----|
| 1.1  | Schematic of the Hydropyrolysis Bench Unit. . . . .                       | 3  |
| 1.2  | Effect of Hydropyrolysis Test Conditions on Char Yield . . . . .          | 6  |
| 1.3  | Arrhenius Plot Showing Regions of Kinetic and Diffusion Control . . . . . | 30 |
| 1.4  | Effect of Thiele Number on the Effectiveness Factor . . . . .             | 42 |
| 2.1  | Schematic of the AutoPychometer 1320 . . . . .                            | 51 |
| 2.2  | Schematic of the Mercury Penetrometer . . . . .                           | 52 |
| 2.3  | Mercury Intrusion Graph . . . . .   | 53 |
| 2.4  | Schematic of the Surface Area Apparatus . . . . .                         | 57 |
| 2.5  | Desorption Peak for Nitrogen Surface Area . . . . .                       | 59 |
| 2.6  | Comparison of Measured and True $N_2$ Surface Area . . . . .              | 60 |
| 2.7  | Desorption Peak for $CO_2$ Surface Area . . . . .                         | 62 |
| 2.8  | Typical Dubinin-Polanyi Plot for $CO_2$ Surface Area . . . . .            | 63 |
| 2.9  | Schematic of the Thermogravimetric Analyser . . . . .                     | 65 |
| 2.10 | Rate of Weight Loss and Temperature for Initial TGA Tests . . . . .       | 66 |
| 2.11 | Effect of TGA Gas Flowrate on Reaction Rate . . . . .                     | 67 |
| 2.12 | Schematic of the Entrained Flow Combustor . . . . .                       | 73 |

|  |     |
|--|-----|
| 2.13 Schematic of the Fluidized Bed Coal Feeder . . . . .                        | 74  |
| 2.14 Detailed Entrained Flow Combustor Reactor Design . . . . .                  | 76  |
| 2.15 Detailed Suction Pyrometer Design . . . . .                                 | 78  |
| 2.16 Effect of Aspiration Rate on Gas Temperature Measurement . . . . .          | 79  |
| 2.17 CO <sub>2</sub> Tracer Measurement in the EFC . . . . .                     | 80  |
| 2.18 Temperature Profile in the EFC . . . . .                                    | 81  |
| 3.1 Effect of Hydropyrolysis Temperature on Char Density . . . . .               | 89  |
| 3.2 Pore Volume Distribution of Hydropyrolysis Chars . . . . .                   | 91  |
| 3.3 Surface Area Distribution of Hydropyrolysis Chars . . . . .                  | 91  |
| 3.4 Characteristic Forms of the TGA Reaction Rate . . . . .                      | 95  |
| 3.5 Reaction Order for the TGA . . . . .   | 99  |
| 3.6 Effect of $\psi$ on Surface Area Change with Conversion . . . . .            | 101 |
| 3.7 Comparison of Char Reaction Rate and Surface Area Development . . . . .      | 102 |
| 3.8 Effect of Char Volatile Matter on TGA Relative Reactivity . . . . .          | 104 |
| 3.9 Effect of Char Volatile Matter on $\overline{RR}$ . . . . .                  | 105 |
| 3.10 Effect of Temperature on TGA Reaction Rates of Chars A-G . . . . .          | 106 |
| 3.11 Effect of Temperature on TGA Reaction Rate for Char H . . . . .             | 107 |
| 3.12 Effect of Residence Time on Burnout @ 1035 K on the EFC . . . . .           | 109 |
| 3.13 Effect of Residence Time on Burnout @ 1335 K on the EFC . . . . .           | 111 |
| 3.14 Effect of Temperature on Char Reaction Rate with Constant $A_c$ . . . . .   | 117 |
| 3.15 Effect of Temperature on Effectiveness Factor with Constant $A_c$ . . . . . | 117 |
| 3.16 Effect of Temperature on Char Reaction Rate with TGA $A_c$ . . . . .        | 119 |

|   |     |
|---|-----|
| 3.17 Effect of Temperature on Effectiveness Factor with TGA $A_c$ . . . . . | 119 |
| 3.18 Effect of $E_c$ on Char Reaction Rate at 1500 K . . . . .              | 122 |
| A.1 Residual Plot for the Surface Area Test . . . . .                       | 140 |



# Nomenclature

## Upper case symbols

|             |  |
|-------------|--|
| $A$         | reactant gas species   |
| $A_c$       | preexponential factor ( $cm/s$ )                                     |
| $B$         | product gas species  |
| $B_1 - B_9$ | coefficients of response surface model for hydropyrolysis            |
| $C$         | factor relating heat of adsorption in successive layers to the first |
| $D_{AB}$    | bulk diffusivity ( $cm^2/s$ )  |
| $D_e$       | effective diffusivity in porous solids ( $cm^2/s$ )                  |
| $D_{Kn}$    | Knudsen diffusivity ( $cm^2/s$ )                                     |
| $E_c$       | activation energy ( $cal/mol$ )                                      |
| $E_d$       | deactivation energy ( $cal/mol$ )                                    |
| $G$         | pore size distribution ( $cm^{-3}$ )                                 |
| $H$         | heat of combustion reaction ( $J/g \times 10^7$ )                    |
| $J$         | mass flux ( $g/cm^2 \cdot s$ )                                       |
| $K$         | apparent overall rate coefficient ( $cm^3/g \cdot s$ )               |
| $L$         | pore length per unit volume ( $cm^{-2}$ )                            |

|                 |  |
|-----------------|--|
| $L_E$           | pore length with no pore overlap ( $cm^{-2}$ )                                   |
| $M_A$           | molecular weight of species A ( $g/gmol$ )                                       |
| $N, N_0, N_1$   | total available, unoccupied and occupied carbon sites respectively for oxidation |
| $P$             | pressure ( $Pa \times 10, atm$ )   |
| $R$             | radial distance from particle center ( $cm$ )                                    |
| $R_p$           | particle radius ( $cm$ )   |
| $RR$            | chemical reaction rate ( $s^{-1}$ or $hr^{-1}$ )                                 |
| $RR_v$          | chemical reaction rate per unit vol. ( $cm^{-3} \cdot s^{-1}$ )                  |
| $\overline{RR}$ | relative reactivity  |
| $R$             | universal gas constant ( $8.314 J/gmol \cdot K$ )                                |
| $S$             | surface area per unit volume ( $cm^{-1}$ )                                       |
| $S_E$           | surface area per unit vol. with no pore overlap ( $cm^{-1}$ )                    |
| $T$             | temperature ( $^{\circ}C, K$ )   |
| $V$             | pore volume per unit volume  |
| $V_E$           | pore volume per unit vol. with no pore overlap                                   |
| $W$             | compression work per unit vol. ( $J/cm^3$ )                                      |

#### Lower case symbols

|                |  |
|----------------|--|
| $b$            | ratio of adsorption and desorption rates     |
| $\overline{c}$ | gas concentration ( $g/cm^3$ )               |
| $c_p$          | specific heat of coal ( $cm^2/s^2 \cdot K$ ) |
| $f$            | functional form ( $cm$ )                     |

|                   |   |
|-------------------|---|
| $g$               | gravitational constant ( $980.6 \text{ cm}^2/\text{s}$ )                  |
| $m_c$             | mass of carbon per active site  |
| $\dot{m}$         | mass flowrate of char ( $\text{g/s}$ )                                    |
| $q'''$            | heat generation per unit volume ( $\text{J}/\text{cm}^3 \times 10^7$ )    |
| $q_{\text{conv}}$ | convective heat loss per unit vol. ( $\text{J}/\text{cm}^3 \times 10^7$ ) |
| $q_R$             | radiative heat loss per unit vol. ( $\text{J}/\text{cm}^3 \times 10^7$ )  |
| $r$               | pore radius ( $\text{cm}$ )   |
| $\bar{r}$         | average pore radius ( $\text{cm}$ )                                       |
| $\bar{r}_M$       | average macropore radius ( $\text{cm}$ )                                  |
| $S_{\text{CO}_2}$ | $\text{CO}_2$ surface area ( $\text{cm}^2/\text{g}$ )                     |
| $S_{\text{N}_2}$  | $\text{N}_2$ surface area ( $\text{cm}^2/\text{g}$ )                      |
| $S_M$             | macropore surface area ( $\text{cm}^2/\text{g}$ )                         |
| $v$               | volume gas adsorbed ( $\text{cm}^3/\text{g}$ )                            |
| $v_m$             | particle monolayer volume ( $\text{cm}^3/\text{g}$ )                      |
| $v_T$             | total pore volume ( $\text{cm}^3/\text{g}$ )                              |
| $\tau$            | thickness of adsorbed gas film ( $\text{cm}$ )                            |
| $x_1 - x_3$       | temperature, pressure and residence time used in response surface model   |

#### Greek symbols

|          |  |
|----------|--|
| $\alpha$ | particle diameter reduction exponent             |
| $\beta$  | particle density reduction exponent              |
| $\Gamma$ | Fraction of $\text{CO}_2$ in combustion products |

|                  |  |
|------------------|--|
| $\gamma$         | surface tension of mercury ( $\text{dyn/cm}$ )   |
| $\epsilon$       | work done by adsorption ( $\text{J/cm}^3 \times 10^7$ )  |
| $\varsigma$      | no. of gas molecules per unit vol. ( $\text{cm}^{-3}$ )  |
| $\eta$           | effectiveness factor   |
| $\Theta$         | contact angle between mercury and carbon ( $130^\circ$ )   |
| $\theta$         | particle porosity  |
| $\Lambda$        | stoichiometric mass ratio of oxygen to carbon in combustion<br>(1.33 for CO: 2.66 for $\text{CO}_2$ product) |
| $\mu$            | gas absolute viscosity ( $\overline{\text{g/cm} \cdot \text{s}}$ )   |
| $\rho_a$         | apparent particle density ( $\text{g/cm}^3$ )  |
| $\rho_T$         | true particle density ( $\text{g/cm}^3$ )  |
| $\sigma$         | particle size parameter  |
| $\tau$           | dimensionless reaction time  |
| $\tau_P$         | particle tortuosity ( $= 2$ )  |
| $\Phi_1, \Phi_2$ | heat transfer factors for convection and radiation, respectively   |
| $\phi$           | Thiele number  |
| $\varphi$        | molecular cross-sectional area ( $\text{cm}^2$ )   |
| $\chi$           | conversion   |
| $\psi$           | pore structure parameter   |

#### Subscripts

|     |              |
|-----|--------------|
| $A$ | reactant gas |
| $a$ | apparent     |

|                       |                 |
|-----------------------|-----------------|
| <i>c</i>              | chemical        |
| <i>CO<sub>2</sub></i> | carbon dioxide  |
| <i>d</i>              | deactivation    |
| <i>e</i>              | effective       |
| <i>ext</i>            | external        |
| <i>g</i> \            | gas             |
| <i>He</i>             | helium          |
| <i>Hg</i>             | mercury         |
| <i>i</i>              | initial         |
| <i>Kn</i>             | Knudsen         |
| <i>m</i>              | monolayer       |
| <i>max</i>            | maximum         |
| <i>N<sub>2</sub></i>  | nitrogen        |
| <i>o</i>              | free stream     |
| <i>P</i>              | particle        |
| <i>s</i>              | surface         |
| <i>T</i>              | total           |
| <i>V</i>              | per unit volume |
| <i>W</i>              | wall            |

# Chapter 1

## Introduction

Hydropyrolysis is the thermal fragmentation of high molecular weight compounds in high pressure hydrogen. When coal is hydropyrolysed, carbon enriched char and hydrogen enriched volatile matter are produced. The volatile matter consists of light oils, heavy aromatic tars, hydrocarbon gases, carbon oxides and water. Chakrabartty and du Plessis<sup>[1]</sup> suggested using the hydropyrolysis process for Alberta coal to extract valuable light oil products from the coal and to burn the remaining solid material in a utility boiler. As char is a major product of coal hydropyrolysis, it must be utilized in order to ensure the economic viability and thermal efficiency of the process. To technically evaluate this process as it pertained to Alberta coal utilization, a study of the reactivity of Alberta's coals under hydropyrolysis conditions and characterization of the combustion properties of the char product was required.

---

<sup>1</sup>Numbers in the brackets designate references

This thesis is concerned with the characterization of the combustion properties of the char product. Before detailing the experimental procedure and results obtained in this evaluation, a description of char properties pertinent to combustion and a review of previous char combustion studies is presented. In addition, the fundamental mechanisms of gas/solid reactions related to coal char combustion are described.

## 1.1 The ARC Hydropyrolysis Process

The hydropyrolysis bench unit of the Alberta Research Council (ARC) as shown in Figure 1.1 was used to evaluate the hydropyrolysis of subbituminous coal from the Highvale mine in Alberta. A description of the development, operation and results of this unit is available in previous reports [2,3]. The coal was pulverized in a hammer mill and mechanically sieved to obtain a  $-100 + 200$  mesh ( $74 - 149 \mu m$ ) particle size fraction. The  $-100 + 200$  mesh size fraction was loaded into a hopper and pressurized at the start of each run. The coal was fed with an auger into a preheated hydrogen stream and entrained with the gas through an externally heated tubular reactor. The evaluation conditions were temperatures of  $600 - 800^\circ C$ , hydrogen pressures of  $3.5 - 10.0 MPa$  and residence time from  $0.5 - 5.0$  seconds. After reaction at the preset test conditions, the char was separated from the gas stream in a cyclone and collected in a char pot. The cyclone was heated to  $400^\circ C$  to prevent tar recondensation on the char surface during separation. After each run, the char was removed from the char pot and stored in glass jars for further

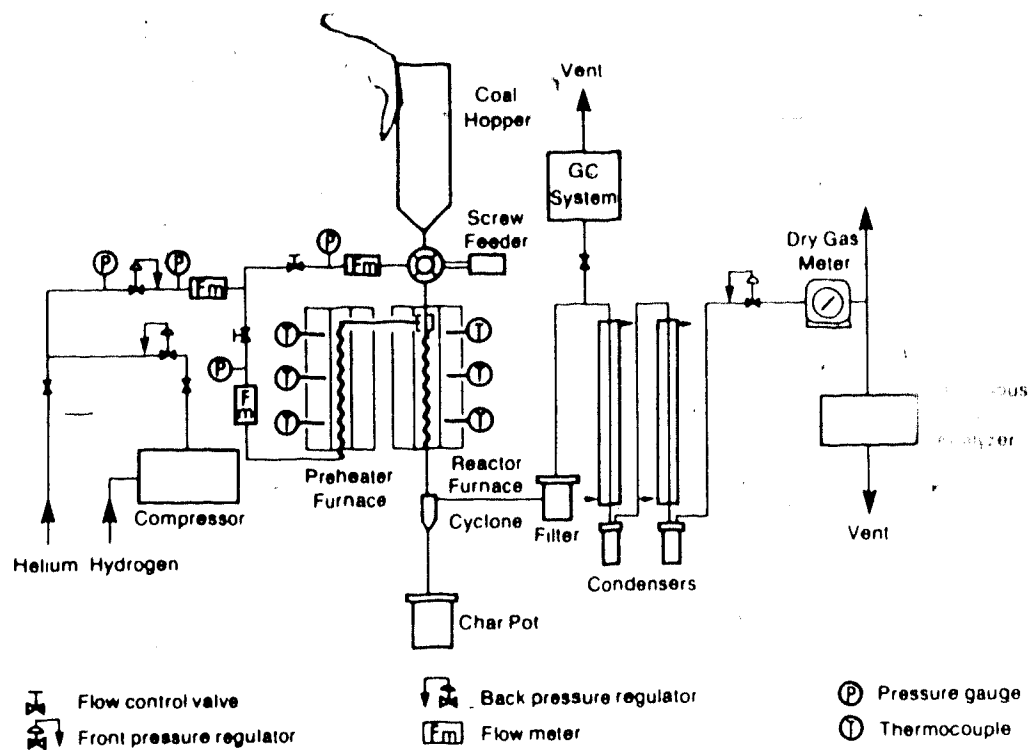


Figure 1.1: Schematic of the Hydropyrolysis Bench Unit

characterization. The yield range is shown in Table 1.1 for the major product groups. The light oil yield which predominately consisted of benzene, toluene, xylene and naphthalene, was the most valuable product from the process. The light oil yield increased from 0 to 11% by weight of the dry, ash free (daf) input coal as hydropyrolysis severity<sup>2</sup> increased. The C<sub>1</sub>-C<sub>5</sub> hydrocarbon gas yield, which was predominately methane and ethane, also increased with process severity from 6 to 20% by weight daf. The increase in light hydrocarbon oil and gas yield coincided with a decrease in heavy oil yield from 13 to 2%. Water, carbon monoxide and carbon dioxide accounted for the remaining volatile matter of 18 to 28% by weight of daf coal.

<sup>2</sup>Severity is defined here as the extreme high temperature, pressure, and residence time conditions used during the hydropyrolysis process.



Table 1.1: Range of Hydropyrolysis Product Yields

| Product             | Yields            |    |
|---------------------|-------------------|----|
|                     | wt% dry, ash free |    |
| Char                | 75                | 40 |
| Tar                 | 13                | 2  |
| Light Oil           | 0                 | 11 |
| Hydrocarbon Gas     | 6                 | 20 |
| CO, CO <sub>2</sub> | 6                 | 10 |
| Water               | 12                | 18 |

At all process conditions, char was the single major product accounting for 40 – 75% by weight of the input coal. The char yield was minimized at the most severe hydropyrolysis process conditions where most of the volatile matter had been stripped from the coal.

The effect of hydropyrolysis temperature, hydrogen pressure and residence time on product yields were studied simultaneously using a Box-Behnken test matrix approach [4]. Fifteen experiments were performed at various process conditions and the yield data were fitted to a quadratic response surface model of the form:

$$y = B_1 + B_2x_1 + B_3x_2 + B_4x_3 + B_5x_1x_2 + B_6x_1x_3 + B_7x_2x_3 + B_8x_1x_2x_3 \quad (1.1)$$

where  $y$  was the product yield expressed as a percentage of the daf coal feed,  $x_1$  was the temperature [°C],  $x_2$  was the pressure [MPa] and  $x_3$  was residence time [s]

Least squares regression was used to estimate the coefficients  $B_1$  through  $B_8$  in

this model for any specific product of interest. This technique resulted in a set of empirical relations to predict the product yields for hydropyrolysis at temperatures from 600 to 800°C, hydrogen pressured from 3.5 to 10.0 MPa and residence time from 0.5 to 5.0 sec.

The effect of hydropyrolysis test conditions on char yield is shown in the three graphs of Figure 1.2. Each graph is a plot of char yield versus gas pressure and residence time (at 600, 700 or 800°C) produced from Equation 1.1. The quadratic response surface model for char yield had a least squares regression value of 0.90 indicating a good fit of the polynomial Equation. The higher reactor temperature always favoured lower char yield as demonstrated from the change in the upper and lower bounds of the ordinate in the three plots. The hydrogen pressure and residence time had a complex affect on the char yield. At 3.5 MPa, the char yield passed through a minimum at 3 seconds, suggesting that some tar repolymerization was occurring on the solid surface at longer residence times. At 10.0 MPa, the char yield continued to decrease with residence time above 3 seconds. The high pressure hydrogen preventing tar recondensation on the char or char yield reduction by direct methanation, was significant at the higher pressure. The residence time reversed the apparent effect of pressure on the char yield. At 0.5 seconds, higher pressure increased the char yield as a result of incomplete devolatilization. At 5.0 seconds, devolatilization was complete at all pressures and the higher pressure favoured the further reduction of char yield by direct methanation.

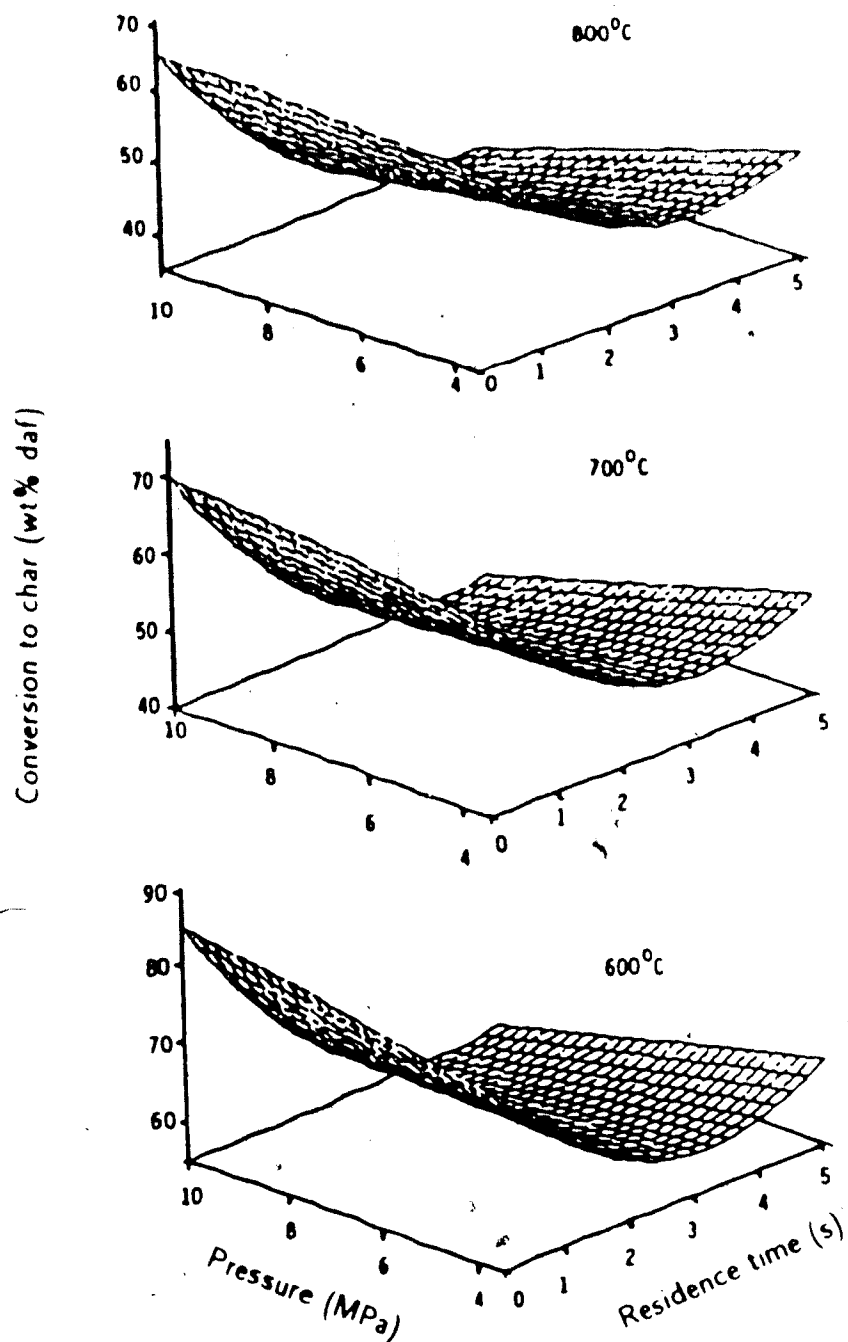


Figure 1.2: Effect of Hydrolysis Test Conditions on Char Yield

## 1.2 Chemical Properties of Char Pertinent to Combustion

### 1.2.1 Evaluation Criteria

Before testing a new coal in a boiler, several laboratory analyses are performed to characterize the chemical structure of the fuel. This information is used to determine a suitable boiler design with minimal operational problems. Proximate analysis is an ASTM standard test (ASTM D 3172M) to determine the moisture, ash and volatile matter content of the fuel. The moisture and ash content of the fuel are important because they are a non-combustible portion. Ash is also critical to the design and operation of the boiler. If not properly considered, buildups on the furnace walls, floor and in the convective tube banks may reduce the heat absorbed by the unit and increase energy loss. Selective components in the ash may corrode and erode boiler tubes eventually causing a shutdown of the unit for cleaning and maintenance [5]. High temperature viscosity measurements are made on ash components to evaluate the slagging tendency on boiler firewalls. The lower the viscosity at a given temperature, the greater would be the tendency to have slagging problems. A sintering test is performed to determine the compressive strength of sintered ash deposits. The lower the sintered strength, the lower is the tendency to have strong deposits. Various formulae based on the elemental composition of the ash have been used to predict the fouling and slagging tendencies of coal ash. The base to acid ratio is an empirical value determined from the

weight fraction of components in the ash and is proportional to the tendency for a coal ash to slag and foul a boiler. The ratio is [5]

$$\text{Ratio} = \frac{\text{Fe}_2\text{O}_3 + \text{CaO} + \text{MgO} + \text{Na}_2\text{O} + \text{K}_2\text{O}}{\text{SiO}_2 + \text{Al}_2\text{O}_3 + \text{TiO}_2} \quad (1.2)$$

The volatile matter content of the fuel has been related to the ease of fuel combustion. Coals with more than 30% volatile matter are generally more easily combusted than lower volatile coals. Volatile matter is released and burned in the boiler in less than 0.1 sec [6,7,8,9]. In comparison the char burnout may require up to 1.5 sec due to the slower rate of heterogeneous reactions and the depletion of oxygen in the boiler. As the volatile matter may contain up to 50% of the energy content of the fuel, the energy release rate is high in the early stages of combustion of high volatile coals. This phenomena ensures that coal particles are rapidly heated to reaction temperature and a flame front is stabilized near the burner quart. This allows the fuel input to be turned down by up to 75% without increasing the risk of extinguishing the flame in the boiler. Coals with less than 20% volatile matter are usually fired in a refractory lined arch type furnace to limit heat loss during the early stage of combustion thereby improving flame stability [10]. Otherwise, a supplementary fuel may be required to maintain the flame [7].

The prediction of combustion performance is not based solely on volatile matter content. Chars remaining after devolatilization have a wide range in combustion reactivity which would influence the overall particle burnout rate [11]. Combustion reactivity may be influenced by differences in chemical reactivity of the solid or

the extent of surface available for reaction. Since both of these parameters are a complex function of reaction conditions, the reactivity of devolatilized coals are normally measured in simulated combustion tests described in Section 1.4.

Ultimate analysis is a standard ASTM test (ASTM D 3176M) used to measure the carbon, hydrogen, oxygen, nitrogen and sulphur content of the fuel. This measurement is necessary to determine stoichiometric air requirements and the flue gas composition. The latter has important implications to gaseous emissions from coal flames. Sulphur emissions such as  $\text{SO}_2$  and  $\text{SO}_3$  are directly proportional to the sulphur content of the fuel and nitrogen emissions are strongly dependent on fuel nitrogen content.

### 1.2.2 Hydropyrolysis Char Properties

The ultimate and proximate analyses of Highvale subbituminous coal and typical hydropyrolysis chars are shown in Table 1.2. The effect of hydropyrolysis is to increase the carbon and nitrogen content of the solid while reducing the oxygen, sulphur and hydrogen. The chars have an elemental composition of 81 – 94% carbon, 3.9 – 2.5% hydrogen, 0.9 – 1.4% nitrogen, 0.0 – 0.3% sulphur and 13.3 – 1.2% oxygen. As a result of this distribution, the boiler flue gas from char combustion would have a similar composition to low volatile bituminous or anthracite coal combustion. Volatile nitrogen components, which have been shown to preferentially form  $\text{NO}_x$  emissions [12,13], and most sulphur compounds are removed in hydropyrolysis. Therefore, lower emissions would be expected from char combus-

Table 1.2: Variation of Hydropyrolysis Char Analyses

| Property           | Weight % daf    |
|--------------------|-----------------|
| Proximate          |                 |
| Ash (dry)          | 14 - 24         |
| Volatiles (daf)    | 10 - 28         |
| Fixed carbon (daf) | 90 - 72         |
| Ultimate (daf)     |                 |
| C                  | 81 - 94         |
| H                  | 2.5 - 3.9       |
| N                  | 0.9 - 1.4       |
| S                  | 0.0 - 0.3       |
| O                  | 1.2 - 13.3      |
| CV (kJ/kg)         | 26,300 - 28,900 |

tion. Also the lower sulphur gas and water vapour content of the flue gas would reduce fouling and low temperature corrosion problems.

The calorific values (CV) of the chars was calculated from their elemental composition using Dulong's formula 14:

$$CV = 33,830C + 144,281\left(H - \frac{O}{8}\right) + 9,420S \quad (1.3)$$

where carbon, C, nitrogen, N, oxygen, O, hydrogen, H and sulphur, S, refer to daf values for the solid fuel sample. This is an accepted formula which is used to predict the CV of coal and other carbonaceous solids within 5% of the CV measured using a bomb calorimeter. The calorific values were converted to a daf basis by multiplying Equation 1.3 by (1-ash weight fraction) where the ash content was determined from the proximate analysis. As shown in Table 1.2, the CV of chars on a dry basis was 26,300 – 28,900 kJ/kg which was typical of a medium volatile bituminous coal. The CV was up to 20% higher than the original coal due to selective removal of oxygen and sulphur from the solid. As a result, less total solid fuel would need to be fired in a utility boiler to obtain the same thermal load. The CV decreased with increased hydrolysis process conditions due to higher ash contents of the chars.

Since all of the coal ash remained in the solid residue, the ash content of the char was up to twice that of the parent coal. This could result in a proportional increase in boiler fouling assuming that all ash properties were unaffected during hydrolysis. Since hydrolysis temperature was always less than 800°C and metal cations within the ash do not volatilize below 1050°C, this was probably a



valid assumption.

The volatile matter was reduced from 41% on a daf basis for the coal to 9–28% for the chars. The low volatile matter content may inhibit flame stability due to less rapid energy release in the early stages of combustion. However, this conclusion must be verified experimentally since the chars may have significantly different physical properties and chemical reactivity than the parent coal which may affect the combustion rate.

## 1.3 Char Surface Characterization

### 1.3.1 Description of Measurement Techniques

Several analytical measurements are necessary to fully characterize the microporous structure of char particles. The particle size must be analysed in order to calculate the aerodynamic and heat transfer properties of the particles in a combustion flame, and to understanding the effect of high temperature flame conditions on particle morphology. The pore volume distribution must be measured to provide information on internal pore surface properties. These measurements may be used to calculate the extent of available surface for oxidation in a combustion environment.

The density of the particles is classified by its true,  $\rho_T$ , and apparent,  $\rho_a$ , values. The true density is the weight of a unit volume of the pore free solid. Since helium is the smallest molecule available, it could penetrate a solid particle

more deeply than any other molecule providing the most acceptable measure of the solid volume. Therefore, helium density has become synonymous with true density although it is not completely effective in penetrating the particle. To calculate the helium density of a solid, the difference in volume of helium occupying a vessel in the presence and absence of a known weight of sample is measured.

The apparent density is the weight of a unit volume of the solid including all its pores and cracks. The most common method of determining apparent density is by mercury displacement. To calculate the apparent density, the difference in volume of mercury occupying a vessel in the presence and absence of a known weight of sample is measured. For this measurement, the sample must be pressurized to approximately 0.4 MPa to ensure that interparticle voids are filled by the mercury and the volume of the particles is accurately determined [15,16].

The mercury displacement is also a useful technique to calculate the volume in pores of a given radius,  $r$ . From Laplace's equation of capillarity [17], the maximum pressure,  $P$ , required to force mercury into a pore of radius  $r$  with circular cross-section is given by the expression:

$$P_{Hg} = -\frac{2\gamma \cos \Theta}{r} \quad (1.4)$$

where  $\gamma$  is the surface tension of mercury and  $\Theta$  is the contact angle between the mercury and the solid. For coals and chars it has been shown that  $\gamma$  is 480 dyn/cm<sup>2</sup> and  $\Theta$  is 130° [16]. The mercury displaced in a solid is measured at increasing intrusion pressure. The change in volume displaced from an increment increase in pressure is related to the volume in pores of a given diameter by Equation 1.4.

The technique has been shown to be valid up to a pressure of 69 MPa at which point the compressibility of the solid becomes significant [16]. The 69 MPa limit corresponds to a pore size of 180 Å.

Although most of the pore volume is located in pores larger than 180 Å, most of the internal surface area is located in smaller pores. Surface area and pore volume distributions in pores smaller than 180 Å are commonly measured by adsorption of gases. Adsorption is an interaction between a solid and a gas whereby a gas molecule striking the surface loses its kinetic velocity and remains on the surface for some finite length of time before leaving the surface [18]. The average length of time that any molecule remains on the surface is a precise value for the solid and gas under a given set of conditions. Describing this process in terms of condensation and evaporation, Langmuir [19] proposed that the rates of these two processes must be in equilibrium. If the surface is assumed to consist of a number of sites  $N$  for which  $N_1$  are occupied and  $N_o$  are free, the rate of evaporation is proportional to  $N_1$  (equal to  $k_1 N_1$ ) and the rate of condensation is proportional to the free surface,  $N_o$ , and the total gas pressure,  $P_g$  (equal to  $k_2 P_g N_o$ ). At equilibrium:

$$k_1 N_1 = k_2 P_g N_o = k_2 P_g (N - N_1) \quad (1.5)$$

Assuming that all of the surface is covered by a monolayer of gas, then  $N$  may be replaced by  $v_m$ , the volumetric monolayer capacity of the surface, and  $N_1$  by  $v$ , the volume of gas adsorbed at the given gas pressure,  $P_g$ . Equation 1.5 may be

rewritten in the form:

$$v = \frac{v_m b P_g}{1 + b P_g} \quad (1.6)$$

where  $b = k_2/k_1$ . If adsorption occurs as a monolayer, then the surface area of a solid could be related to the monolayer capacity by the cross-sectional area of the adsorbed molecules. However, most solids adsorb gases in a multilayer which complicates the calculation of  $v_m$  from the Langmuir formulation. Brunauer, Emmett and Teller extended Langmuir's approach to multilayer adsorption resulting in the well known BET Equation [19,20].

$$v = \frac{v_m C x}{(1 - x)(1 + (C - 1)x)} \quad (1.7)$$

where  $x = P/P_0$  and  $C = \exp[(Q_1 - Q_u)/RT]$  is a factor relating the adsorption in the first layer to the heat of vaporization for all successive layers. In this expression,  $Q_1$  and  $Q_u$  are the heats of adsorption in the first and each successive layer, respectively,  $R$  is the universal gas constant and  $T$  is the particle temperature. For most surfaces the value of  $C$  is very large so that Equation 1.7 reduces to:

$$v = \frac{v_m}{1 - x} \quad (1.8)$$

The BET Equation has become a standard for calculating surface area using  $N_2$  adsorption data at 77 K [16]. Several studies summarized by Mahajan [16] have shown that the value of  $v_m$  for coals and chars may be calculated accurately from Equation 1.8 over the relative pressure range,  $x$ , from 0.05 to 0.30. The equation predicts too little adsorption at lower pressures and too much adsorption at higher pressures.

Having calculated  $v_m$ , the surface area of the solid is determined from the expression:

$$S_{N_2} = v_m \zeta \phi_{N_2} \quad (1.9)$$

where  $\zeta$  is the number of molecules per unit volume at the standard test conditions and  $\phi_{N_2}$  is the cross-sectional area of each molecule assuming that the molecules are hexagonal close packed on the surface. For nitrogen,  $\phi_{N_2}$  is assumed to be  $16.2 \text{ \AA}^2/\text{molecule}$  [16].

Nitrogen adsorption is suitable to measure surface areas in pores as small as  $12 \text{ \AA}$  in cross-sectional diameter, but in smaller pores the diffusion of nitrogen is too slow at  $77 \text{ K}$  to be completed in a reasonable length of time. There is also some question as to whether layer by layer filling as assumed in the BET Equation is applicable to pores smaller than  $12 \text{ \AA}$  in cross-sectional diameter since capillary condensation may predominate. Several investigators have reviewed this problem and determined that the adsorption of  $\text{CO}_2$  at  $298 \text{ K}$  gives a reasonable measure of total available surface area for pores as small as  $5 \text{ \AA}$  [15,16,21]. At a temperature of  $298 \text{ K}$ ,  $\text{CO}_2$  would not condense and vapourize as suggested by the BET Equation. Therefore, to relate adsorbed volume to total volume of the solid, the potential theory is used [22]. This theory which was first formalized by Polanyi [22], suggests that a potential field exists on the surface of the solid such that the adsorbed gas density decreases away from the adsorbent. For a gas in adsorption equilibrium with a surface, there must be no net free energy change when moving from one region to another. If  $\epsilon_z$  represents the work done by adsorption forces when a parcel

of gas is brought to a position,  $x$ , from the surface, then there is a corresponding increase in compression free energy according to

$$\epsilon_x = \int_{P_g}^{P_s} V dP \quad (1.10)$$

where  $P_g$  is the vapour pressure in equilibrium with the adsorbed phase. Assuming that the adsorbed phase may be approximated by a multilayer condensed film, then the thickness of the film,  $x$ , is related to the adsorbed liquid volume,  $v$ , by

$$v = \frac{s_{CO_2} x v_o}{v_l} \quad (1.11)$$

where  $v_o$  is the molar volume of the gas (24,320 cc/mol),  $v_l$  is the molar volume of the liquid and  $s_{CO_2}$  is the surface area of the solid. The potential  $\epsilon_x$  at  $x$  required to cause condensation on the interface is

$$\epsilon_x = RT \ln \left( \frac{P_o}{P_g} \right) \quad (1.12)$$

where  $P_o$  is the saturation pressure of the adsorbate. Equation 1.12 has been related semi-empirically by Dubinin[23] to the volume of gas adsorbed by the equation:

$$v = v_m \exp(-d\epsilon_x^2) \quad (1.13)$$

for extremely small micropores in which overlapping of the potential fields of opposite pore walls is prominent. In this equation,  $d$  is a constant and  $V_m$  is the monolayer capacity of the solid. Combining Equations 1.12 and 1.13 gave:

$$\ln v = \ln v_m - dR^2T^2 \left( \ln \frac{P_o}{P_g} \right)^2 \quad (1.14)$$

Calculation of the volume of gas adsorbed at several gas pressures,  $P_g$ , should yield a straight line on a  $\log v$  vs  $[\log P_0/P_g]^2$  plot with an intercept of  $\log v_m$ . Assuming, further, that most of the internal particle surface area is located in pores large enough for only one  $\text{CO}_2$  molecule to condense, the total surface area may be calculated from the expression

$$S_{\text{CO}_2} = v_m \times \varphi_{\text{CO}_2} \quad (1.15)$$

where  $\varphi_{\text{CO}_2}$ , the cross-sectional area of a  $\text{CO}_2$  molecule, is  $25 \text{ \AA}^2$ . In practice, the reported total surface area as measured by  $\text{CO}_2$  adsorption gives only a relative measure of effective internal area, since the assumption of adsorption in a monolayer cannot be tested.

### 1.3.2 Coal and Char Surface Structure

The surface structure of several Alberta subbituminous coals has been characterized by Parkash<sup>24</sup>. The true density ranged from 1.37 to 1.46 g/cc on a daf basis and the apparent density ranged from 1.1 to 1.3 g/cc. The total porosity,  $\theta$ , of the coals calculated from the expression:

$$\theta = 100 \left( 1 - \frac{\rho_a}{\rho_T} \right) \quad (1.16)$$

ranged from 10 to 20%. Total open pore volumes, calculated from the same data according to:

$$v_T = \frac{1}{\rho_a} - \frac{1}{\rho_T} \quad (1.17)$$

were 0.1 to 0.2 cc/g for Alberta subbituminous coals. The nitrogen and carbon dioxide surface areas were  $2-9 \text{ m}^2/\text{g}$  and  $75-300 \text{ m}^2/\text{g}$ , respectively. These values

of pore volume density and surface area are within the range of results reported by Gan et al [15] for similar American coals.

The effect of pyrolysis and hydrolyrolysis conditions on the surface structure of Alberta coals has not been previously investigated. However, it is known that these coals behave as thermosets and do not soften on heating up to 1600°C. For thermoset type coals the removal of volatiles results in an increase in porosity and solid surface area. The surface structural changes of Montana and North Dakota lignites, both of which behave as thermosets, during atmospheric pressure flash pyrolysis was investigated by Nsakala et al [25]. The pulverized coal was devolatilized at various residence times in an entrained flow reactor maintained at 965°C. The particle true density increased with residence time from 1.5 to 1.7 g/cm<sup>3</sup> in one second and the particle apparent density decreased from 1.3 to 0.9 g/cm<sup>3</sup> in 0.4 seconds. The particle porosity increased from 12% to 50% in approximately 0.5 seconds. The nitrogen surface area increased from less than 1 m<sup>2</sup>/g to 30 m<sup>2</sup>/g and the carbon dioxide surface area increased from 200 to 370 m<sup>2</sup>/g in one second. Ashu [26] using the same devolatilization apparatus, measured the surface areas of chars from selected high pressure coal conversion processes which were rapidly heated to 800°C in nitrogen. The gasification chars used by Ashu had nitrogen and carbon dioxide surface areas in the range of 200 – 470 m<sup>2</sup>/g and 520 – 775 m<sup>2</sup>/g respectively. Gasification chars used by Wells [27] prepared from American sub-bituminous coal in the Occidental atmospheric pressure flash pyrolysis process had nitrogen surface area of 200 – 300 m<sup>2</sup>/g and porosity of 55%. Johnson [28]



gasified American lignite and subbituminous coals in hydrogen at a pressure of 35 atmospheres and 925°C using a fixed bed reactor. He found that char  $\text{CO}_2$  surface area increased from 500 to 750  $\text{m}^2/\text{g}$  as carbon conversion increased to 20%. The surface area remained constant during further gasification. Total pore volume increased from 0.4  $\text{cc}/\text{g}$  for the coal to 0.45  $\text{cc}/\text{g}$  for the char at 40% carbon conversion and decreased at higher conversion. The gasification reaction rate was correlated with total micropore surface area suggesting that gasification occurred on all internal pore surfaces. Therefore, most of the increase in pore volume was caused by gasification in the micropores.

From these results, it may be concluded that processing thermoset type coals in high pressure hydrogen tends to increase the carbon dioxide surface area appreciably compared to low pressure processing. The reported range of carbon dioxide surface areas for chars processed at atmospheric pressure was 200 - 370  $\text{m}^2/\text{g}$  compared to 500 - 775  $\text{m}^2/\text{g}$  for chars processed at high pressure. No results on the nitrogen surface area have been reported for chars processed in high pressure hydrogen, although the reported range in surface area data cited for low pressure pyrolysis (30 - 300  $\text{m}^2/\text{g}$ ) indicate that the results are highly variable. The wide range could be attributed to variations in process conditions, reactor configuration and fuel handling. However, without a systematic investigation of the effect of process conditions on char surface properties it was not possible to quantify the extent of the influence.

## **1.4 Evaluation of Coal and Char Combustibility**

### **1.4.1 Pilot Scale Experiments**

Major boiler manufacturers undertake several combustion tests to evaluate the combustibility of coals. These tests range from thermogravimetric analysis utilizing microgram quantity coal samples through to 50,000 tonne sample, full scale burn tests. There is consensus in the industry that a full scale burn test is a prerequisite to establish the performance of a coal in a specific full scale boiler. However, smaller scale combustion tests are essential during the preliminary characterization of the fuel to design the boiler and to minimize the risk of poor performance in the full scale burn. Organic heterogeneity, ash complexities and a lack of understanding of the coal combustion process all contribute to the unpredictability and costly testing of a new coal. The testing is further complicated by the possibility of variable coal combustion behaviour throughout a coal deposit resulting in poor combustion performance at some time during the mine life.

As elaborate coal combustion testing is generally required to evaluate any new coal, detailed testing would certainly be required for a new fuel such as hydrolysis char. Significant changes could have been induced to the fuel rendering conventional combustion tests results for the parent coal inappropriate or misleading with regard to hydrolysis char combustion performance. Unfortunately, it is extremely costly to produce sufficient quantities of char for full scale char combustion tests at the process development stage. This explains, in part, the

Table 1.3: Operating Conditions for Select Coal Conversion Processes

| Process    | Residence Time (s) | Reaction Temperature ( $^{\circ}\text{C}$ ) | Pressure (MPa)                                      | Flow Configuration |
|------------|--------------------|---|---|--------------------|
| ARC        | 0.5 – 5.0          | 600 – 800                                   | 0.5 – 5.0 ( $\text{H}_2$ )                          | Entrained          |
| Bigas      | 3                  | 1100 – 1200                                 | 5.0 ( $\text{N}_2/\text{CO}_2$ )                    | Entrained          |
| Rockwell   | 0.06 – 0.6         | 900 – 1000                                  | 0.7 ( $\text{H}_2/\text{H}_2\text{O}$ )             | Entrained          |
| Occidental | 2                  | 600 – 800                                   | 0.1 ( $\text{N}_2/\text{CO}_2$ )                    | Entrained          |
| Toscoal    | 900 – 1800         | 523   | 0.1 (Products)                                      | Moving Bed         |
| FMC-COED   | 7200               | 400 – 900                                   | 0.1 ( $\text{N}_2/\text{CO}_2/\text{H}_2\text{O}$ ) | Fluid Bed          |

limited amount of char combustion data in the literature.

The results of only two full scale burn tests using chars from coal conversion processes have been reported. In 1974, Foster Wheeler Energy Corporation conducted a full scale burn test of a gasification char from Utah King mine high volatile bituminous coal generated from the FMC-COED process [29]. In this process, coal was injected into a fluidized bed reactor at 400 – 900 $^{\circ}\text{C}$  with a mixture of atmospheric pressure nitrogen, carbon dioxide and steam as the fluidizing medium (see Table 1.3). The coal reacted in the bed for two hours before it was removed. The low char volatile matter content (3.2 – 7.7% as received) and the high carbon content (93% daf) prompted Foster Wheeler Energy Corporation to evaluate

the char in a 50 MW thermal, arched, downward fired furnace designed for low volatile, anthracite coal. The char was successfully fired with satisfactory burner and flame stability over a turndown ratio of 3 to 1. The char burned hotter and more efficiently than anthracite indicating that the char was a suitable boiler fuel in a downward fired furnace.

The Occidental Research Corporation evaluated the combustion properties of pyrolysis char in a commercial scale combustor<sup>[30]</sup>. Occidental char was produced by pyrolysing pulverized coal in an entrained flow reactor with a preheated mixture of nitrogen and carbon dioxide at a temperature of 600 – 800°C and atmospheric pressure (see Table 1.3). After ~~two~~ seconds residence time, the char was separated from the gas stream in a heated cyclone to prevent tar recondensation on the particle surface. In combustion tests, a Wyoming subbituminous coal char with 13.7% volatile matter and 15% ash performed as well or better than the parent coal in the full scale boiler. The results of the Occidental char combustion tests showed that the low char volatile matter content did not hinder combustion performance, thereby contradicting the conventional thinking on the importance of volatile matter to flame stability<sup>[10]</sup>. The ability of this char to burn in a conventional pulverized boiler designed for high volatile coal suggested that chars could displace some or all of the coal fired in existing units.

Despite successful demonstration scale char combustion tests, there remains some doubt regarding the suitability of chars as boiler fuels. There is contradictory evidence from pilot scale experiments whether chars required special boilers

designed for low volatile fuels or could be fired as a makeup fuel in an existing boiler designed for the parent coal. Three chars produced from the Toscoal pyrolysis process were combusted in a 0.4 MW (thermal input) boiler to evaluate combustion behaviour<sup>10</sup>. In the Toscoal process, coal was pyrolysed with atmospheric pressure pyrolysis gas product for 15 to 30 minutes in a moving bed at a temperature of 700 K. The chars contained only 17 – 28% volatile matter but burned easily in the pilot scale combustor. These results suggested that the chars could be burned in existing boilers designed for the parent coal with no modification to the burner or the combustion chamber.

The combustibility of five chars prepared in the Bigas, Rockwell, Occidental, Toscoal and FMC-COED processes were evaluated in the laboratory scale combustion unit at Brigham Young University (BYU)<sup>9,27</sup>. The chars were separated into two distinct groups of combustion performance based on their ability to burn with or without additional flame support from a gas flame. Chars produced from thermosetting western American coals in the Occidental and Toscoal processes were able to burn without flame support. These were the same two chars burned in the Foster Wheeler and Occidental demonstration scale tests<sup>29,30</sup>. The authors concluded that these chars would be suitable as makeup fuels in existing utility boilers. Chars produced from thermoplastic, eastern American coals in the Bigas, Rockwell and FMC-COED processes could not be burned without flame support.

There were several major differences between the two groups of chars. First,

the combustion performance was separated according to parent coal type. Thermosetting type coal chars could be combusted without flame support whereas the thermoplastic coal chars could not. High combustibility chars were produced in the Occidental and Toscoal processes which were both low temperature and low pressure processes. In contrast, two of the three low combustibility chars were generated in high temperature ( $900 - 1100^{\circ}\text{C}$ ), high pressure ( $0.7 - 5 \text{ MPa}$ ) hydrogen systems (see Table 1.3). As the third low combustibility char was produced in the low pressure, low temperature FMC-COED process, combustion performance may be more sensitive to parent coal type than process conditions.

Char properties may also have been important in the combustibility evaluation tests at BYU. The ultimate and proximate analysis and nitrogen surface area were the only commonly reported measurements made on these process chars (see in Table 1.4). The Occidental and Toscoal chars had volatile matter contents of 14 and 17% dry weight compared to the Bigas, Rockwell and COED chars which had volatile matter contents of 4, 5 and 9% by weight, respectively. On this basis the authors concluded that the volatile matter was essential to the high combustion performance in their reactor.

Earlier combustion tests conducted by Cogoli[33] in a laminar flow, laboratory scale combustor were performed on chars prepared from the Exxon, Bureau of Mines and FMC-COED coal conversion processes. The Exxon and Bureau of Mines processes were proprietary and no information was available on their operating parameters. However, it is known that American subbituminous and high

Table 1.4: Ultimate and Proximate Analyses and N<sub>2</sub> Surface Area of Select Chars

| Processes  | Ultimate (daf)    |     |     |     |      | Proximate (dry) |      |      | N <sub>2</sub> Surface Area (m <sup>2</sup> /g) |
|------------|-------------------|-----|-----|-----|------|-----------------|------|------|---|
|            | C                 | H   | N   | S   | O    | Ash             | VM   | FC   |   |
| Bigas      | 96.7              | 0.9 | 0.7 | 1.7 | 0.0  | 18.3            | 4.4  | 77.3 | 225   |
| Rockwell   | 94.5              | 1.1 | 1.2 | 2.2 | 0.9  | 19.8            | 5.0  | 75.2 | 15  |
| Occidental | 87.4              | 1.4 | 1.5 | 0.7 | 9.0  | 15.6            | 14.1 | 70.4 | 298   |
| Toscoal    | 83.6              | 3.3 | 1.9 | 0.6 | 10.6 | 17.2            | 17.4 | 65.4 | 8   |
| FMC-COED   | 92.0              | 2.0 | 2.0 | 3.2 | 0.8  | 13.5            | 9.1  | 77.4 | 115   |
| Exxon 1    | 98.7 <sup>a</sup> | 0.9 | 0.6 | 2.8 | -    | 40.2            | 8.0  | 51.8 | 324   |
| Exxon 2    | 95.8              | 1.1 | 0.6 | 2.7 | -    | 24.3            | 13.8 | 61.9 | 372   |
| BOM        | 94.0              | 1.1 | 1.6 | 0.6 | 2.6  | 13.3            | 5.1  | 81.6 | 363   |

volatile bituminous coals from the Wyodak and Illinois mines, respectively were tested in the Exxon process and are designated as Exxon 1 and Exxon 2 processes, respectively in Table 1.4. A Utah high volatile bituminous coal from the King mine was tested in the Bureau of Mines process. The ultimate and proximate analyses and  $N_2$  surface areas of these chars are shown in Table 1.4. The combustion performance of these chars was separated into two groups. Chars produced in the proprietary Exxon process burned as well as Pittsburgh bituminous coal whereas Bureau of Mines and FMC-COED chars burned as poorly as anthracite. Cogoli showed that combustion performance could not be adequately correlated with the volatile matter content of the char or the parent coal type. In these studies it was found that the extent of gasification and the porosity of the char had the most pronounced effect on combustion performance. Exxon chars, which were severely gasified, had a large volume in pores greater than 130 Å in diameter. Large pores may be essential to rapid burning of pulverized char particles. Cogoli concluded that Exxon chars may be suitable as makeup fuel for a utility boiler.

The combustibility of chars generated from the flash pyrolysis of Australian subbituminous coal was tested in an entrained flow combustor at 723°C<sup>31,32</sup>. The chars were prepared by rapidly heating coal in a fluidized bed reactor at atmospheric pressure and bed temperature from 500 to 800°C<sup>33</sup>. In general, the chars were shown to burn as well as brown and bituminous Australian coals suggesting that they would be suitable as makeup fuels in a utility boiler. These chars had volatile matter contents which decreased with pyrolysis temperature



from 28% dry weight at 540°C to 8% at 800°C. The loss in volatile matter lowered the reactivity by 43%.

The contradictory conclusions regarding the suitability of chars as makeup fuels in utility boilers may result for several reasons. As already discussed, the wide range in coal types from Australian brown coals to western and eastern American coals used in these experiments makes correlations of the effect of process conditions on char combustibility difficult. At the same time, the wide range in process conditions makes predictive correlations of the effect of coal type on char combustibility equally difficult. Compounding the problem are the widely different combustors used in the experimental tests. The apparatus vary from a laminar flow entrained flow reactor used in the Australian char studies 31, to a 0.1 MW pilot combustor in the Occidental tests 27 and a 0.4 MW pilot combustor used in the Toscoal tests 10. As all of the tests were comparative, the nature of the combustion process and the configuration of the units may affect the relative combustion behaviour of the process chars and coals. Therefore, it is essential to obtain more fundamental data on the combustibility of these fuels in order that differences in the reactor configuration may be properly assessed.

#### 1.4.2 Laboratory Scale Experiments

To compare the combustion behaviour of char and coal the reaction regime must be known in order to assess the relative advantage of one fuel to another. The oxidation rate of a particle may be limited by diffusion from the bulk stream to

the particle external surface or from the external particle surface to internal pore surface. The rate may also be limited by the chemical reaction rate of the surface (more will be discussed on this subject in Section 1.5). In order to separate the effects of mass transport and chemical reaction, it would be necessary to perform experiments under conditions where one mechanism was dominant. To study the differences between chemical reactivities of chars, the experiments should be performed under conditions of chemical control [41], (ie at a relatively low temperature). The temperature below which the reaction of a solid is operating under kinetic control may be obtained from experimental data. If the reaction rate of a solid is calculated over a wide range of reaction temperatures and plotted in Arrhenius form, a graph of the form shown in Figure 1.3 would be produced. The slope of the curve is the activation energy of the reaction. Reactions operating under kinetic control would have a higher activation energy and therefore a steeper slope on the plot. Carbon oxidation has an activation energy of 30,000 - 40,000  $cal/mol$ . As temperature increases, the reaction shifts to pore diffusion control resulting in a lesser slope with an activation energy of 20,000  $cal/mol$ . At the highest temperature shown on the graph, the reaction shifts to bulk diffusion control where the activation energy is typically 5000  $cal/mol$ .

Researchers have studied the reaction of chars at low temperature to eliminate diffusion limitations and to understand their chemical nature using a technique called thermogravimetric analysis (TGA). In this method, the fuel is placed in a pan suspended from a balance beam. The pan is immersed in a heated environment

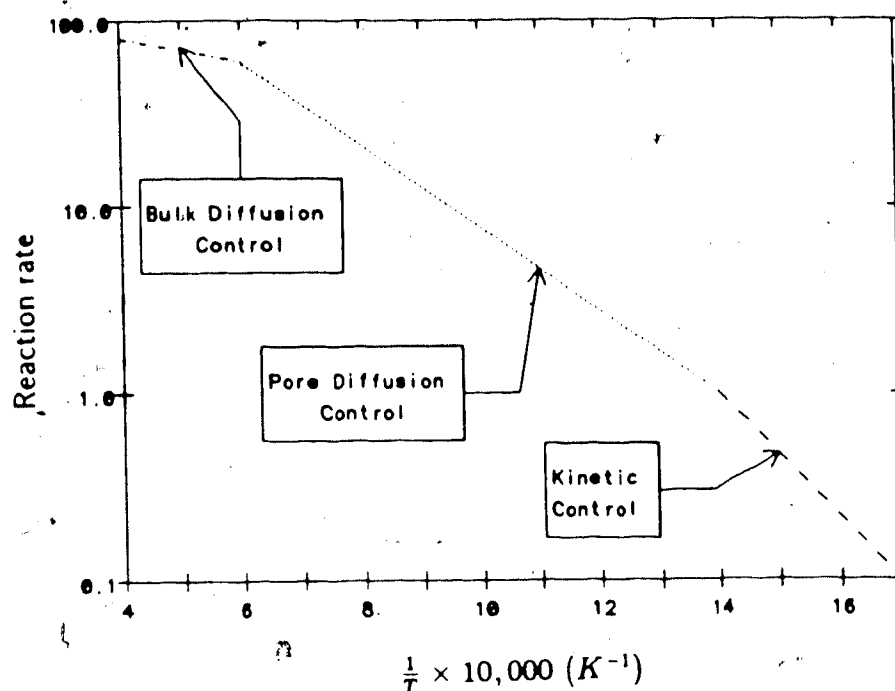


Figure 1.3: Arrhenius Plot Showing Regions of Kinetic and Diffusion Control of flowing reacting gas and the loss in weight of the sample is recorded with respect to time. Since the sample temperature may be carefully controlled the rate of the particle oxidation may be measured.

The low temperature thermogravimetric analysis has been used extensively to study the effect of process conditions on the kinetic mechanisms of char oxidation. For gasification chars prepared at a temperature of 850 – 950° C, a pressure of 2 – 7 MPa in hydrogen-methane, hydrogen-steam or oxygen-steam atmospheres, char reactivity depended more on gasification conditions than the parent coal type used in the study 39,40. Coal which was rapidly heated ( $> 10^3$  °C/s) produced a char which was generally more reactive than char prepared by slow heating. The most reactive carbon atoms were located at the edges of basal planes and their abundance increased as the crystallite size decreased 41. Rapid heating

tended to limit the crystal growth of the char by limiting the time for carbon atom reordering[42], a process similar to annealing.

Higher pyrolysis temperature reduced the char reactivity by a process of re-ordering the active carbon sites into a more stable ring system. Tseng and Edgar[43] modelled the deactivation process after the equation proposed by

Blackwood[44].

$$\frac{k_t}{k_v} = \exp \left[ E_d \left( \frac{1}{RT} - \frac{1}{RT_0} \right) \right] \quad (1.18)$$

where  $E_d$  was the thermal deactivation energy and  $k_v$  and  $k_t$  were the intrinsic kinetic rate constants of char pyrolysed at  $T_0$  and  $T$ , respectively. They found the thermal deactivation energy of lignite char was 17 kcal/gmole. In addition, this parameter was a strong function of coal type and char preparation atmosphere, ranging from 9 – 18 kcal/gmole.

The atmosphere in which chars were prepared affected oxidation reactivity. Chars prepared in a hydrogen atmosphere by slow heating at atmospheric pressure had an oxidation reactivity six times lower than char prepared in nitrogen[45]. The lower reactivity for hydropyrolysis char was attributed to a more thorough removal of the oxygen from the coal and also to a fraction of the active carbon sites being covered with hydrogen.

It has been well established that selective components in the coal ash, particularly calcium, sodium and potassium, catalyse the oxidation reaction[41,42,46,47,48]. Calcium, which is present in low rank coals as exchangeable cations on carboxylic acid groups, is finely dispersed in the solid after pyrolytic decarboxylation and may provide a highly dispersed active catalyst. Differences in reactivity of up to

three orders of magnitude were found by varying the calcium loading on a treated lignite char [48]. Improved reactivity with calcium loading may be limited to low temperature experiments. The catalytic activity of the ash constituents would be significantly reduced due to sintering [42] and the carbon oxidation reaction would be accelerated at high temperature. However, catalytic activity has been used to explain the discrepancy in oxidation reactivity tests made at low and high temperature.

Ashu [26] studied the reactivity of Exxon, Bureau of Mines and COED chars (see Table 1.4) in a thermogravimetric analyser with air heated to 500°C. It was concluded that char oxidation reactivity decreased with increasing process temperature due to thermal deactivation of the carbon. Coals which were rapidly heated during gasification produced chars with a higher reactivity. The higher heating rates produced a thermal shock in the coal which limited chemical reordering of the carbon in the char and resulted in greater surface area for oxidation to occur.

The chars used by Ashu [26] were the same as those used by Coğoli [34] in high temperature, laminar flow combustion tests. A twofold increase in oxidation reactivity measured by TGA, corresponded to an order of magnitude decrease in the ignition time on the laminar flow combustor. Essenhigh [6] concluded that these results showed that extrapolation from one set of conditions to another was not possible. The reactivity measured on experiments at 500°C using TGA were not representative of conditions found in the flame and could not be used to predict high temperature combustion behaviour.

Radovic [35] studied the reactivity of chars produced from the Occidental, Toscoal, COED, Rockwell and Bigas processes using TGA. The char reactivity decreased substantially with increasing processing temperature and residence time. Occidental char, produced at 600°C and atmospheric pressure (see Table 1.3) was 200 times more reactive than Rockwell chars produced at 900°C, and hydrogen pressure of 0.7 MPa. Also an increase in residence time from 60 to 600 ms for chars produced in the Rockwell process resulted in a twofold decrease in reactivity. The loss in reactivity with increasing process temperature and residence time was correlated with a decrease in the number of active carbon sites. Active carbon sites were measured, somewhat arbitrarily, by chemisorbing oxygen onto the surface of a char sample at 102°C for twelve hours [36]. The temperature of the sample was raised to 950°C for three hours to remove all CO and CO<sub>2</sub>. The rate of weight loss during TGA could be equated to the number of carbon active sites but could not be equated to the total internal surface area available for reaction. Since the number of active carbon sites may change substantially with process conditions, the chemical reactivity may also vary.

The chars investigated by Radovic were the same chars studied in the pilot scale combustor at Brigham Young University [9,27]. The Rockwell, Bigas and COED chars which had the lowest TGA oxidation reactivities, could not produce a stable flame in the pilot scale combustor. In comparison the Occidental and Toscoal chars, prepared at low pressure and moderate temperatures had the highest reactivity on the TGA analysis and produced stable flames in the pilot

combustor. Although the TGA and pilot scale combustion test results indicated similar relative char oxidation reactivities, it was concluded that TGA could not be correlated with high temperature reactivity. The relative high temperature reactivity varied by only a factor of two compared to the low temperature reactivity which varied by a factor of 200. The chars with a higher porosity had a greater high temperature combustibility. This observation was in substantial agreement with conclusions made in other work 34. Despite the wide range in feed coal and process conditions used in these studies, the authors were able to conclude that the high temperature reactivity was dominated more by physical char properties, namely the volatile matter content and porosity. In contrast, TGA char reactivities were dominated by pyrolysis process conditions. Therefore, chemical kinetics measured at low temperature may have little influence on particle reactivities at high temperature.

## 1.5 Combustion Mechanisms

The observed differences in reactivity at low temperature and at flame temperatures may be explained by the changing controlling mechanism between the two temperatures. The combustion of a char particle involves the following steps.

1. Bulk diffusion of reactant to the particle surface.
2. Intraparticle diffusion of the reactant.

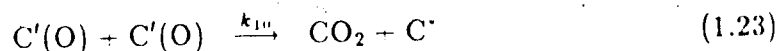
3. Dissociative adsorption of the reactant species on active sites on the particle surface.
4. Desorption of adsorbed products.
5. Intraparticle diffusion of the products.
6. Bulk diffusion of product away from the particle surface.

Any of these steps may control the reaction rate depending on experimental conditions. At low temperature (ie  $< 500^{\circ}\text{C}$ ) the reaction is chemically controlled [37,38] by steps 3 and 4. Above this temperature and up to flame temperatures, it is now generally agreed that the reaction is chemically and pore diffusion controlled (steps 2 through 5). At very high temperatures or at extremely low reactant concentration, the reaction is controlled by bulk diffusion (steps 1 and 6). Therefore observed differences in reactivity at  $500^{\circ}\text{C}$  may only partially account for differences in reactivity at flame temperatures. If there are large differences in the char pore structure, then intraparticle diffusion may be vastly different for chars with similar chemical reactivities, thus affecting particle burnout rates.

### 1.5.1 Oxidation Reaction

The kinetics of the carbon-oxygen reaction have been studied extensively although there is no agreement on the governing mechanism. One proposed mechanism reported by Laurendeau [37] is





where  $\text{C}^*$  was an active carbon site,  $\text{C}'$  was a carbon which has formed a complex with an oxygen atom and  $k_3$  to  $k_{10}$  were the reaction rate constants.

Reaction 1.19 is dissociative chemisorption of oxygen on active carbon surfaces. Reactions 1.20 and 1.22 describe the surface migration of intermediate bonded oxygen (weak surface bonds) to stronger chemical bonds. The difference between the two is that reaction (1.22) accounts for rapid conversion of intermediate bonds to CO at low temperatures. Reaction (1.21) is conventional desorption of the chemically bonded CO complex to CO gas. Reaction (1.23) accounts for direct conversion to  $\text{CO}_2$  gas although it would be of little consequence in most coal combustion processes.

After extensive manipulation of these Equations assuming that the reaction proceeded at steady state conditions, Laurendeau<sup>40</sup> showed that at low temperatures, mobile site desorption was controlling and the chemical reaction rate,  $RR$ , was given by:

$$RR = \frac{m_c}{2} \text{C}^* k_9 \quad (1.24)$$

where  $m$  was the mass of carbon per active site and  $\text{C}^*$  was the number of active

sites per unit surface area. Notice that the reactivity was independent of the oxygen concentration (zero order reaction). At intermediate temperatures, site migration was controlling and the chemical reaction rate was:

$$RR = \underbrace{m_C}_{\text{sites}} C^* k_8 \left( \frac{k_7}{k_{10}} \right)^{\frac{1}{2}} (c_{O_2})^{\frac{1}{2}} \quad (1.25)$$

a half order reaction with respect to oxygen partial pressure. At high temperatures, dissociative chemisorption was controlling and the chemical reaction rate was given by:

$$RR = 2m_C k_7 [C^*]^2 c_{O_2} \quad (1.26)$$

a first order reaction.

The above model is not definitive, but illustrates that the order of reaction with respect to oxygen partial pressure could vary over the temperature range of interest from zero order at low temperature to first order at high temperature. Also, the controlling mechanism of carbon oxidation may change with temperature. The chemical reactivity is dependent on the active carbon surface at all temperatures with second order dependence at high temperature. Therefore, evaluation of the chemical reaction rate of a group of chars at low temperature would indicate the difference in active carbon surface and may be important in evaluating the chemical reaction rate at a higher temperature. However, the mechanism of oxidation may change so that the chemical kinetics derived at 500°C may not be applicable if extrapolated to flame temperatures.

### 1.5.2 Diffusion Effects

Extrapolation of data from experiments conducted at low temperature to flame temperatures may also be complicated by diffusion limitations of oxygen inside the porous network of the char. Three mechanisms govern the transport of reactant species in a porous solid particle: bulk, Knudsen and activated diffusion 49. When the pore diameter is larger than the mean free path of a diffusing reactant gas then gas to gas molecular collisions are more frequent than gas to pore wall collisions. In this case bulk diffusion of oxygen predominates. Bulk diffusion is described by Fick's Law which for a spherical particle is given by:

$$J_A = -D_{AB} \nabla c_A = \frac{D_{AB}(c_{A,\infty} - c_{A,s})}{R_p} \quad (1.27)$$

where  $J_A$  is the mass flux of  $A$  to the surface,  $D_{AB}$  is the mass diffusivity,  $c_{A,\infty}$  and  $c_{A,s}$  are the concentration of species  $A$  in the free stream and on the particle surface, respectively, and  $R_p$  is the particle radius.

When the pore diameter is smaller than the mean free path of the gas, gas to pore wall collisions are most common and Knudsen diffusion of oxygen dominates. The mass flux of oxygen in a spherical particle controlled by Knudsen diffusion,  $J_{A_{Kn}}$ , is given by:

$$J_{A_{Kn}} = -D_c \nabla c_A = -\frac{D_c}{R^2} \frac{d}{dR} \left( R^2 \frac{dc_A}{dR} \right) \quad (1.28)$$

where  $R$  is the radial distance from the center of the particle,  $c_A$  is the reactant

concentration on the particle surface and  $D_e$  is the effective diffusion coefficient.

Smith 54, showed that the effective diffusion coefficient may be calculated from

$$D_e = \left[ \frac{\tau_p}{D_{Kn}\theta} + \frac{1}{D_{AB}} \right]^{-1} \quad (1.29)$$

where  $\theta$  is the particle porosity,  $\tau_p$  is the tortuosity (a value between 2 and 7 to account for pore geometry complexity which is assumed to equal 2 in this work) and  $D_{Kn}$  the Knudsen diffusion coefficient. The coefficient for Knudsen diffusion is given by the expression:

$$\begin{aligned} D_{Kn} &= \frac{r}{3} \sqrt{\frac{8RT_p}{M_A}} \\ &= 9700r \sqrt{\frac{T_p}{M_A}} \end{aligned} \quad (1.30)$$

where  $r$  is the pore radius,  $T_p$  is the particle temperature,  $R$  is the universal gas constant and  $M_A$  is the molecular weight of the gas. When pore size is similar to the molecular diameter, chemical interaction between the gas and solid dominates and the process is defined as activated diffusion. Activated diffusion is extremely sensitive to the pore size and very small changes can alter the diffusion mechanism from activated to Knudsen diffusion 50. Activated diffusion is much slower than either Knudsen or bulk diffusion and is neglected in this work as a useful component of the oxidation mechanism 51. However, activated diffusion will be reconsidered in the discussion on surface area development during reaction in Section 3.2.1.

Several models have been developed to account for gaseous diffusion in porous coal chars. The models may be classified into either macroscopic or microscopic types. Macroscopic models assume that an effective diffusivity may be defined for

the entire sphere based on known information of the solid pore structure. One such model used extensively by Smith et al [53,54] was based on the work of Mehta and Aris [55]. The diffusion inside a porous particle (Equation 1.28) was equated to the chemical reaction rate per unit volume,  $RR_V$  defined as:

$$\begin{aligned} RR_V &= \Lambda k_c S_a c_A \\ &= \frac{1}{R^2} \frac{d}{dR} [R^2 J_{A_{Kn}}] \end{aligned} \quad (1.31)$$

where  $k_c$  is the chemical reaction rate constant which has an Arrhenius type temperature dependency,  $S_a$ , is the apparent surface area per unit volume and  $\Lambda$  is the stoichiometric mass ratio relating carbon reaction rate to oxygen consumption. If the primary reaction product was carbon monoxide,  $\Lambda$  was equal to 1.33 and if the primary reaction product was carbon dioxide,  $\Lambda$  was equal to 2.66.

Substituting into Equation 1.31 the expression:

$$\frac{c_A}{c_{A_s}} = \frac{f(R)}{R} \quad (1.32)$$

where  $c_{A_s}$  was the reactant concentration at the particle external surface yielded

$$\frac{d^2 f}{dR^2} = \frac{\Lambda k_c S_a f(R)}{D_e} \quad (1.33)$$

integrating twice and backsubstituting Equation 1.33 gave:

$$\frac{c_A}{c_{A_s}} = \frac{R_P}{R} \frac{\sinh\left(\sqrt{\frac{\Lambda k_c S_a}{D_e}} R\right)}{\sinh\left(\sqrt{\frac{\Lambda k_c S_a}{D_e}} R_P\right)} \quad (1.34)$$

where  $R_P$  was the particle radius. Substituting Equation 1.28 into 1.34 gave:

$$J_{A_{Kn}} = D_e c_{A_s} \left[ \frac{1}{R_P} - \sqrt{\frac{\Lambda k_c S_a}{D_e}} \coth\left(\sqrt{\frac{\Lambda k_c S_a}{D_e}} R_P\right) \right] \quad (1.35)$$

At the surface of the particle  $J_{A_{Kn}} = J_{AB}$ . Therefore, Equation 1.27 was substituted into Equation 1.35 to eliminate  $C_A$ , finally yielding

$$J_{A_{Kn}} = \frac{\frac{D_e c_{A,i}}{R_p} [1 - \phi \coth \phi]}{1 - \frac{R D_e}{R_p D_{AB}} [1 - \phi \coth \phi]} \quad (1.36)$$

where the Thiele number,  $\phi$  was a dimensionless ratio of the chemical reaction rate to the pore diffusion rate expressed by:

$$\phi = \sqrt{\frac{\Lambda k_c S_a}{D_e}} R_p \quad (1.37)$$

If there were no pore diffusion restriction, then all of the internal particle surface could react and the total reaction rate would be given by:

$$J_A = -\frac{\Lambda k_c S_a c_{A,i} R_p}{3} \quad (1.38)$$

Division of Equation 1.36 by 1.38 gave the effectiveness,  $\eta$ , of the internal surface to react:

$$\eta = \frac{\frac{3}{\phi^2} [\phi \coth \phi - 1]}{1 - \frac{D_e}{D_{AB}} [1 - \phi \coth \phi]} \quad (1.39)$$

Most reported results have neglected bulk diffusion limitations in the above analysis ( $D_{AB} \gg D_e$ ) so that the effectiveness was equal to the numerator of Equation 1.39. The nature of Equation 1.39 with the denominator set equal to unity is shown in Figure 1.4. As the Thiele number increases to a value in excess of unity, the effectiveness of the internal surface to react decreases rapidly. For Thiele number in excess of 10, the effectiveness of the internal surface is reduced to less than 0.15. However, reaction on only 15% of the internal surface still greatly increases the total available surface area over the external surface area of a coal

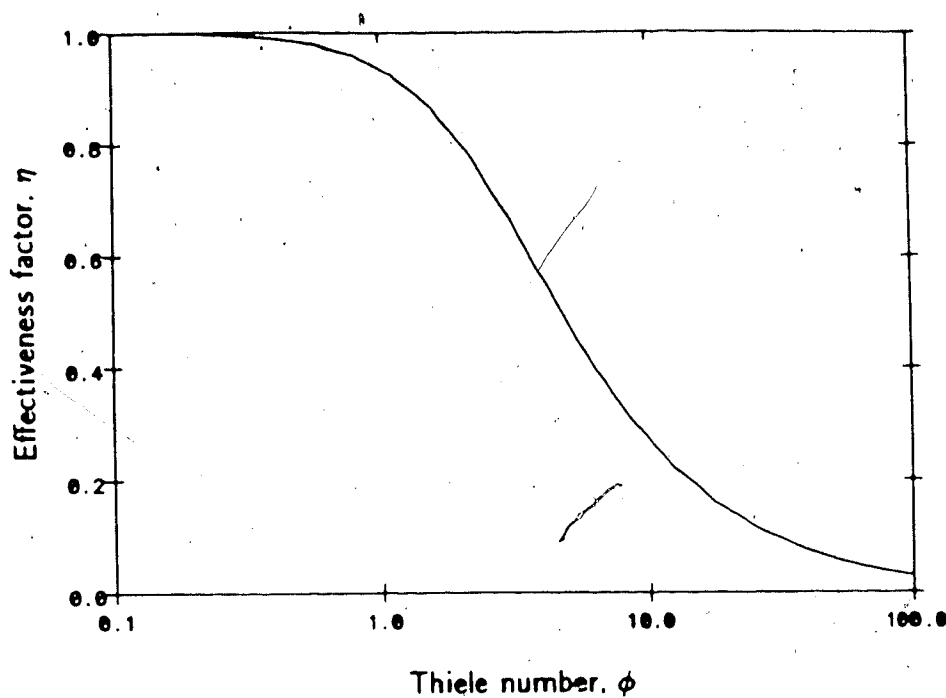


Figure 1.4: Effect of Thiele Number on the Effectiveness Factor

particle. For example, a  $100 \mu\text{m}$  diameter particle has an external surface area ( $S_{ext} = 3/R$ ) of less than  $0.1 \text{ m}^2/\text{g}$ . Examination of porosimetry data indicates that the internal surface of char particles in even the largest pores may exceed the external surface area by one to two orders of magnitude. Therefore, it is important to consider the reacting internal surface area when interpreting combustion results.

An average value for  $D_e$  and  $S_a$  were also required in Equations 1.36 and 1.39 to calculate char reaction rates. Both  $D_e$  and  $S_a$  are a function of pore radius which varied from  $5 - 20,000 \text{ \AA}$  for the chars considered. To evaluate the effective diffusivity,  $D_e$ , used in Equations 1.36 and 1.39, an average pore radius was required.

Smith used the expression developed by Wheeler<sup>52</sup> who assumed that the

pore structure could be adequately described by pores of a single diameter,  $\bar{r}$ , according to:

$$\bar{r} = \frac{2\theta\tau_p^{0.5}}{S_{CO_2}\rho_a} \quad (1.40)$$

Smith and Tyler [53] also extended Wheeler's unimodel pore size model to a bi-model pore size model to determine the influence of pore size distribution on the Thiele number and effectiveness calculations for a burning coal particle. They approximated the pore size distribution as a group of macro and micropores and calculated the Thiele number for each. They concluded that there was little difference between the unimodel and bimodel pore size models on calculated Thiele numbers and effectiveness factors.

Although the macroscopic models are suitable to define global pore diffusion limitations, they do not provide specific details of the process occurring in individual pores. This information is necessary to understand the changes in pore diameter, pore volume and surface area during reaction. Recent microscopic models include those of Simons et al [56,57,58,59], Perlmutter et al [60,61,62], Srinivas and Amundson [63], Gavalas [64,65], and Hashimoto and Silveston [66].

The Lewis and Simons [56] model considered that the porous char structure was made up of a series of pore trees in which a pore which intersected the external surface of the particle was a tree trunk and the smaller pores branched off of the feeder system. The tree system was modelled using a pore distribution function. The diffusion limitations were calculated for each individual tree system and combined with all other model pore trees in the particle to obtain the overall particle



diffusion rate.

The models of Srinivas and Amundson and Hashimoto and Silveston used a differential equation to describe the change in pore size distribution as a function of time. This equation was integrated with respect to time and related to the solid reaction rate to obtain pore structure characteristics as a function of conversion. The models had several parameters which were estimated from the combustion results so that the model was not suitable to predict the combustion rate of particles.

Bhatia and Perlmutter [60] and Gavalas [64] independently proposed a random pore model to account for diffusional effects and structural changes during combustion. The model of Bhatia and Perlmutter is developed in full in the following discussions. This model will be used to interpret combustion data in Section 3.2.1.

Bhatia and Perlmutter considered a reacting solid with a pore size distribution  $G(r, t)$  where  $G(r, t)dr$  was the total length of pore surface per unit pore plus solid volume having a radius between  $r$  and  $r + dr$ . They defined the total length,  $L_E$ , surface  $S_E$  and volume  $V_E$  of a non-overlapped system of pores by:

$$L_E = \int_0^\infty G(r, t) dr \quad (1.41)$$

$$S_E = 2\pi \int_0^\infty r G(r, t) dr \quad (1.42)$$

$$V_E = \pi \int_0^\infty r^2 G(r, t) dr \quad (1.43)$$

A mass balance of the change in size distribution for reacting pores gave:

$$\frac{\partial G}{\partial t} + \frac{\partial}{\partial r} \left( G \frac{dr}{dt} \right) = 0 \quad (1.44)$$

If reaction rate was proportional to total surface area (generally only possible under kinetic reaction control) then the change in pore radius could be expressed by:

$$\frac{dr}{dt} = \frac{k_c c^n}{\rho_a} \quad (1.45)$$

where  $k_c$  was the chemical reaction rate constant,  $c$  was the reactant concentration and  $n$  was the reaction order. Combining Equations 1.44 and 1.45 gave

$$\frac{\partial G}{\partial t} = \frac{k_c c^n}{\rho_a} \frac{\partial G}{\partial r} \quad (1.46)$$

Integrating with respect to  $r$  and knowing that  $G(0, t) = G(\infty, t) = 0$  gave

$$\int_0^\infty \frac{\partial G}{\partial t} dr = 0 \quad (1.47)$$

Substituting Equation 1.41 and using Leibnitz's Rule for differentiation under the integral sign they found:

$$\frac{dL_E}{dt} = 0 \quad (1.48)$$

Multiplying Equation 1.46 by  $2\pi r$ , integrating with respect to  $r$  and inserting definitions 1.41 and 1.42 an equation for total surface was obtained.

$$\frac{dS_E}{dt} = \frac{2\pi k_c c^n L_E}{\rho_a} \quad (1.49)$$

Also, multiplying Equation 1.46 by  $\pi r^2$  and integrating with respect to  $r$  and using Equation 1.43, an expression for the total open pore volume was obtained.

$$\frac{dV_E}{dt} = \frac{k_c c^n S_E}{\rho_a} \quad (1.50)$$

Combining Equations 1.48, 1.49 and 1.50 gave:

$$S_E = S_{E_i} + 2\pi \frac{k_C c^n L_{E_i} t}{\rho_a} \quad (1.51)$$

$$V_E = V_{E_i} + S_{E_i} \frac{k_C c^n t}{\rho_a} + \pi L_{E_i} \left( \frac{k_C c^n t}{\rho_a} \right)^2 \quad (1.52)$$

where  $L_{E_i}$ ,  $S_{E_i}$  and  $V_{E_i}$  were the initial pore length, surface and volume, respectively. Bhatia and Perlmutter used the expressions:

$$V = 1 - \exp(-V_E) \quad (1.53)$$

$$S = S_E (1 - V) \quad (1.54)$$

$$L = L_E (1 - V) \quad (1.55)$$

to relate volume, surface and length of the pore system to the corresponding volume surface and lengths in the absence of any pore overlap. Substituting Equations 1.53-1.55 into Equations 1.51 and 1.52 gave:

$$S = \frac{1 - V}{1 - V_i} \left( S_i + 2\pi L_i \frac{k_C c^n t}{\rho_a} \right) \quad (1.56)$$

$$\ln(V - 1) = \ln(V_i - 1) + \frac{S_i}{1 - V_i} \left( \frac{1 - V}{1 - V_i} \right) + \frac{\pi L_i}{1 - V_i} \left( \frac{k_C c^n t}{\rho_a} \right)^2 \quad (1.57)$$

Squaring Equation 1.56 and substituting in Equation 1.57 they obtained

$$\frac{S}{S_i} = \frac{1 - V}{1 - V_i} \left[ 1 - \frac{4\pi L_i (1 - V_i)}{S_i^2} \ln \left( \frac{1 - V}{1 - V_i} \right) \right]^{0.5} \quad (1.58)$$

Su and Perlmutter[61] successfully correlated this model with chars prepared from anthracite and high volatile bituminous coals from the Eastern United States. Gavallas[65], using a similar model, successfully fitted the data of Mahajan et al[45] and Dutta and Wen[40] but with limited information on the pore structure of their chars.

The results of the model suggested that the internal structure of chars particles changed substantially during reaction. Su and Perlmutter concluded that changes in pore structure may have been primarily responsible for the changes in reaction rate observed during the oxidation of coal under kinetic control. Pores enlarged and eventually coalesced during reaction resulting in significant changes in the internal surface of the particle.

### 1.5.3 Controlling Mechanism

The behaviour of a particle surface during reaction is dependent on the reaction conditions as well as the chemical and physical properties of the solid. If reaction is slow, all pore surfaces will oxidize and all pores will increase in size until they coalesce. This behaviour is typical of oxidation at low temperatures where the process is kinetically controlled. At flame temperatures, bulk or pore diffusion may be rate controlling in which case the larger diameter pores close to the surface will oxidize preferentially. The particle would burn in a partial shrinking core mechanism as the reaction proceeds inwards to the unreacted core. This behaviour indicates the importance of a well developed pore structure with a significant fraction of larger pores. These pores will enhance the transport of oxygen to the particle interior causing the solid to oxidize evenly increasing the rate of carbon burnout per unit volume.

Proper account of the influence of pore structure will determine, to a large extent, the agreement between intermediate and flame temperature determinations.

of particle combustibility. If a particle has an extensive microporous structure but limited larger (transitional pores), reactivity may be high at intermediate temperatures but poor combustibility may result at flame conditions. Proper evaluation of the factors contributing to particle burnout would reduce the risk of extrapolating results at one set of test conditions to another.

## 1.6 Objectives of the Research

The overall objective of this research was to determine the suitability of hydrolysis char from Alberta subbituminous coal as a makeup fuel in a utility boiler. To attain this objective, several sub-objectives were defined. These were:

1. To characterize the surface structure of the chars and evaluate changes which occurred at different hydrolysis conditions.
2. To measure the oxidation reactivity of chars under kinetic control in order to evaluate chemical changes induced in the solid during hydrolysis.
3. To measure the combustibility of chars at flame conditions.
4. Relate the results of objectives 1, 2 and 3 to evaluate the suitability of Alberta subbituminous coal char as a substitute fuel in a utility boiler.

## 1.7 Point of Departure

A systematic investigation on the effect of hydrolysis conditions on Alberta subbituminous coal char physical and chemical properties has not been reported in the literature. Combustion tests have only been performed on a small number

of chars prepared from widely different coals and conversion processes. Therefore, the effects of process conditions and coal type on char combustibility have been difficult to conclude. In the present work, the combustibility of chars generated from a single Alberta subbituminous coal, hydrolysed in the Alberta Research Council hydrolysis bench unit over a wide range of temperature, pressure and residence time was studied. These tests provided a comprehensive set of data to indicate the effect of process conditions on Alberta subbituminous coal char physical and chemical properties and combustibility.

## Chapter 2

# Method Development

### 2.1 Surface Characterization

To characterize the physical structure of the char particles, all of the analyses described in Section 1.3 were used; namely, the true density, mercury porosimetry, nitrogen and carbon dioxide surface areas. True densities were measured using the automated Micromeretics Instrument Corporation, AutoPycnometer 1320. A schematic of the device is shown in Figure 2.1. To measure helium density a dry sample of char was weighed and loaded into sample chamber A. After the system was evacuated and helium was introduced, the system was pressurized through pistons D and E. If chambers A and C had the same volume and the compression was carried out isothermally, then the pressures in chambers A and C measured at the differential pressure transducer B, must have been the same. Because chamber A contained the sample, the gas volumes would not be the same and compression would cause a pressure differential. The chamber C volume was

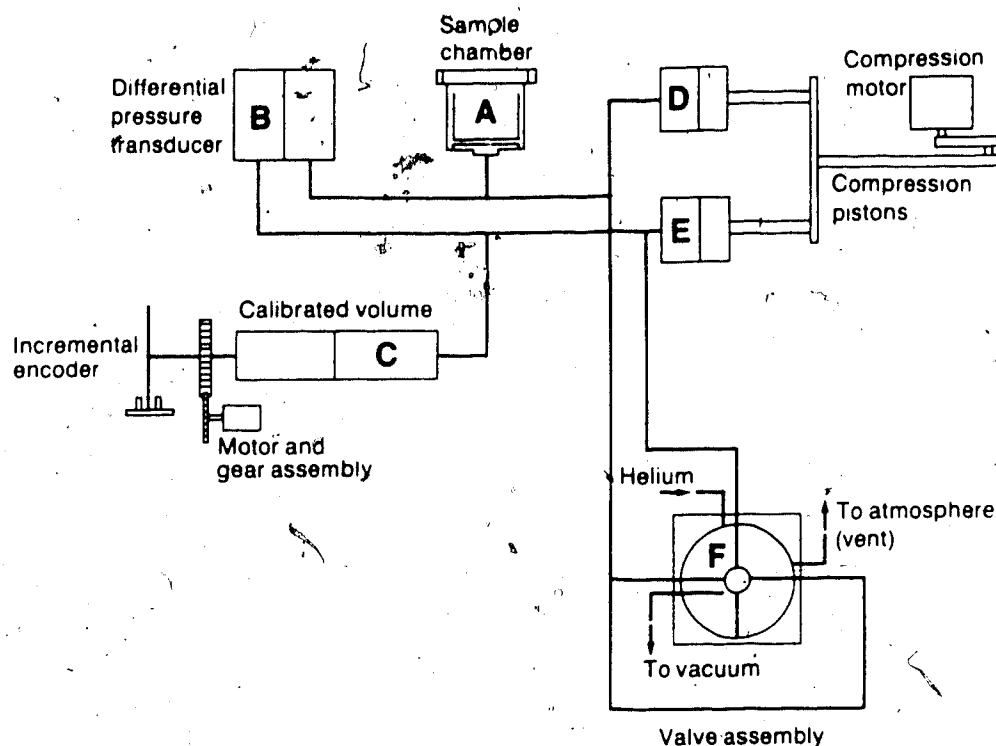


Figure 2.1: Schematic of the AutoPychometer 1320

decreased using a gear assembly and the change recorded on a microcomputer using an incremental encoder. The compression was removed and the procedure repeated approximately five to ten times until a compression stroke did not cause a differential pressure in the two sample volumes. The amount that the volume of chamber C was reduced to minimize the differential pressure was equal to the volume of the sample. The reported accuracy of sample volume measurement was  $\pm 0.02$  cc or approximately 3% of the density measurement.

Mercury porosimetry was completed using a Micromeretics Instrument Corporation, Model 9300 porosimeter. The procedure used to measure the pore volume distribution was to load a sample of coal or char into the penetrometer, seal and weigh the assembly. A sketch of the penetrometer is shown in Figure 2.2. The



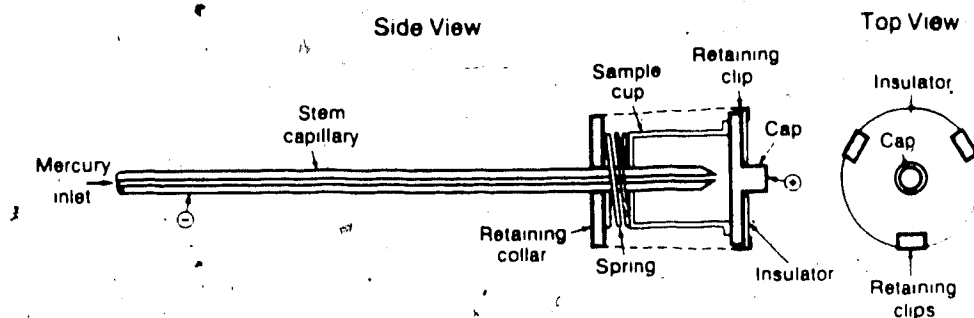


Figure 2.2: Schematic of the Mercury Penetrometer

sample weight was calculated from the known weight of the penetrometer. The penetrometer was fitted into a low pressure chamber where it was degassed to  $1.5 \times 10^{-3}$  torr at room temperature for approximately 2 hours and then filled with mercury. After the penetrometer was filled with mercury, the pressure was increased in increments of 6 – 12 *kPa*. As mercury penetrated interparticle voids and solid pores, the amount of mercury in the penetrometer stem decreased. The amount of mercury penetrating the particle was calculated from the change in capacitance of the penetrometer stem. The capacitance was linearly related to the volume of mercury in the stem and therefore, could be related to the penetration of mercury into the particles. The mercury pressure was increased to atmospheric (90 *kPa*) after which the penetrometer was removed from the low pressure apparatus and installed on the high pressure apparatus. The pressure was increased in 0.1 *MPa* increments up to 0.6 *MPa*, in 1.5 *MPa* increments up to 7 *MPa* and in 7 *MPa* increments to a maximum pressure of 70 *MPa*.

Changes in capacitance were converted to mercury volume displaced by a pre-

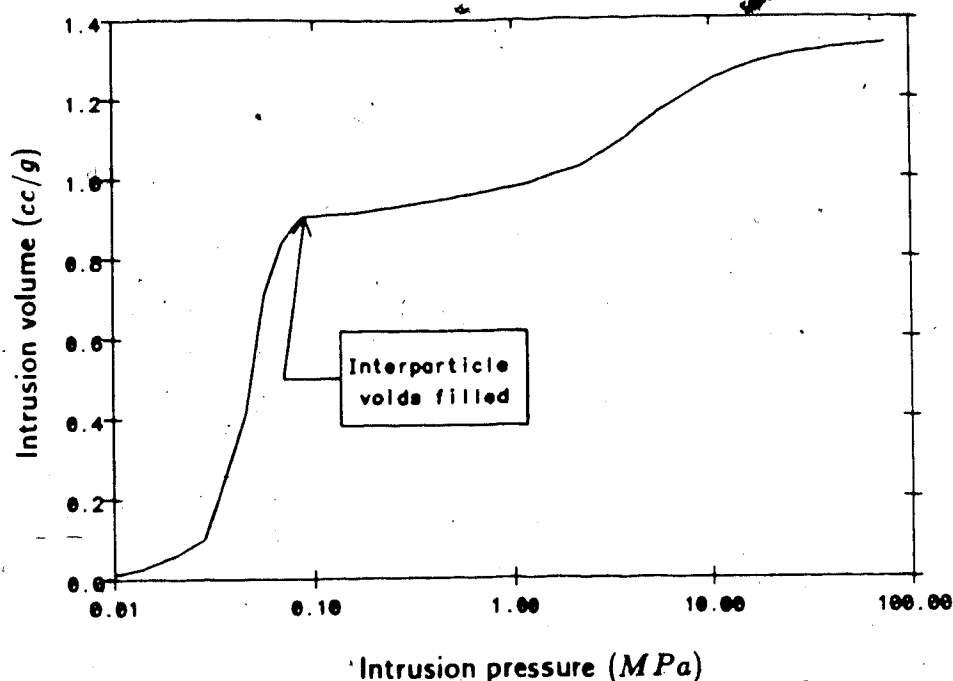


Figure 2.3: Mercury Intrusion Graph

vious calibration of the instrument. The result of this procedure was a change in the volume of mercury penetrating the sample at increasing pressure. A plot of the volume of mercury penetration with sample pressure is shown in Figure 2.3. The pressure of the mercury was related to the volume in pores of a given radius using the Washburn Equation (Equation 1.4). The data could also be related to the surface area in pores of a given radius based on thermodynamic considerations. The work required to force mercury into the pores of a solid  $dW$  would equal  $PdV$  which could be equated to the area,  $S$ , of the char in contact with the mercury by the expression [69]:

$$dW = -P dV = \gamma_{LV} \cos \Theta dS \quad (2.1)$$

where  $\gamma_{LV}$  was the surface tension between the liquid and the vapour and  $\Theta$  was

the contact angle between the mercury and the char. Integrating this expression over an incremental pressure range gave:

$$S = - \int_{V_1}^{V_2} \frac{P dV}{\gamma_{LV} \cos \Theta} \quad (2.2)$$

The surface tension of mercury at room temperature was 485 [dynes/cm] and the contact angle for char was assumed to be equal to 130° [24]. At any given pressure, the pore radius was known and the incremental change in volume,  $V_i$ , from  $P_i$  to  $P_{i+1}$  was known so that surface area was calculated directly from Equation 2.2. An example of the data obtained using the Model 9300 mercury porosimeter for a hydrolysis char is shown in Table 2.1.

No commercial instruments were available to measure the nitrogen and carbon dioxide surface areas of the chars so that an instrument was developed for this purpose. The technique used was based on a procedure first proposed by Nelson and Eggertsen [68] and refined by Haley [70] to determine adsorption curves using a continuous gas flow method. In the procedure the adsorbate was adsorbed by the sample at the temperature of interest from a gas stream containing the adsorbate in helium flowing over the sample. The adsorbate was eluted by heating the sample to a temperature at least 100°C in excess of the adsorption temperature. The volume of gas eluted was measured using a thermoconductivity cell on a standard gas chromatograph. Haley concluded that the adsorption isotherms developed by this method were comparable with isotherms obtained by the conventional pressure-volume method of adsorption measurement and the surface area values showed good agreement.

Table 2.1: Typical Mercury Porosimetry Data for Hydropyrolysis Chars

| Pressure<br>(MPa) | Diameter<br>( $\mu m$ ) | Cumulative<br>Pore Volume<br>(cc/g) |
|-------------------|-------------------------|-------------------------------------|
| 0.01              | 180.0000                | 0.0000                              |
| 0.03              | 36.7347                 | 0.1111                              |
| 0.08              | 16.5138                 | 0.7020                              |
| 0.34              | 3.5618                  | 0.7408                              |
| 0.48              | 2.5526                  | 0.7458                              |
| 1.00              | 1.2374                  | 0.7585                              |
| 2.10              | 0.5894                  | 0.7767                              |
| 3.78              | 0.3283                  | 0.8013                              |
| 7.23              | 0.1717                  | 0.8357                              |
| 13.84             | 0.0897                  | 0.8706                              |
| 27.79             | 0.0446                  | 0.8947                              |
| 55.23             | 0.0225                  | 0.9090                              |
| 76.53             | 0.0162                  | 0.9114                              |

The adsorption apparatus developed for this study and shown in Figure 2.4, was similar to the apparatus used by Haley. The adsorbate entered the unit at 0.7 MPa and was split into two parallel streams. The pressure of stream 1 was reduced to near atmospheric, flowed ~~passed~~ the reference arm of a thermoconductivity cell from a Hewlett Packard Company, Model 5830 gas chromatograph and vented to atmosphere. The pressure of stream 2 was reduced to an adjustable intermediate pressure using a gas regulator, *R2*, and passed over the inline sample. The pressure was further reduced to near atmospheric at *R3*, passed over the measuring arm of the thermoconductivity cell and vented to atmosphere. A sample valve was installed between the sample and *R3* to allow known volumes of adsorbate to be injected into the system in order to calibrate the volume of gas eluted to the detector response of the thermoconductivity cell. The flowrate of the gas in streams 1 and 2 were balanced using flow restrictors, *FR1* and *FR2*, at 30 ml/min.

The char sample was held in a straight 6 mm stainless steel tube between two pyrex glass wool plugs (see Figure 2.4). Before a test, the char sample would be outgassed at a temperature of 150°C and pressure of 10 kPa to remove surface moisture. The dried sample would be weighed and installed in the unit immediately before a surface area measurement was made to avoid recondensation of water vapour on the sample surface.

For nitrogen surface area measurements, a standard calibration gas supplied by Matheson Gas Products Canada containing  $9.78 \pm 0.2\%$  nitrogen in helium was

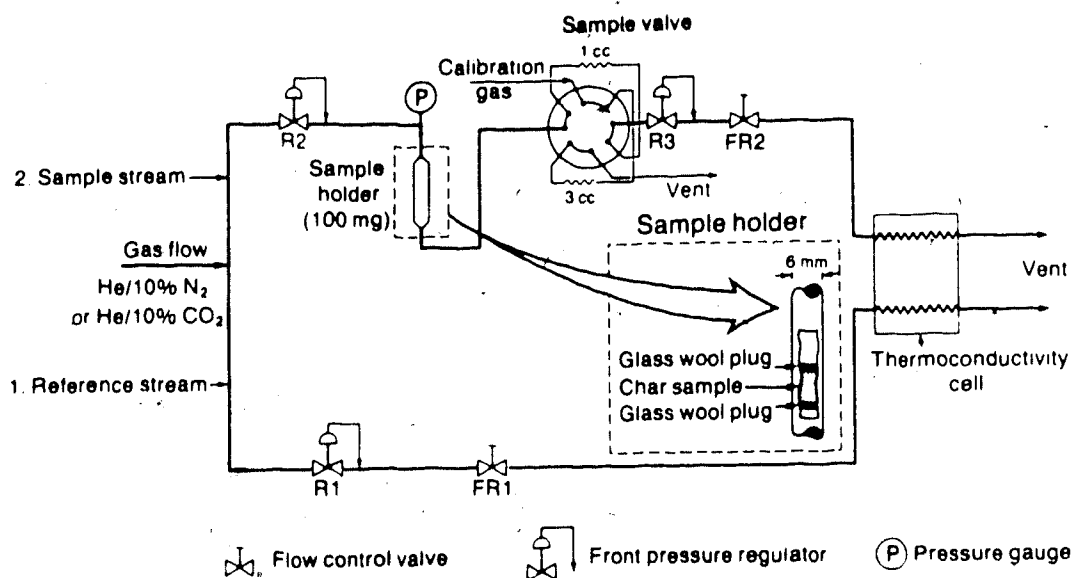


Figure 2.4: Schematic of the Surface Area Apparatus

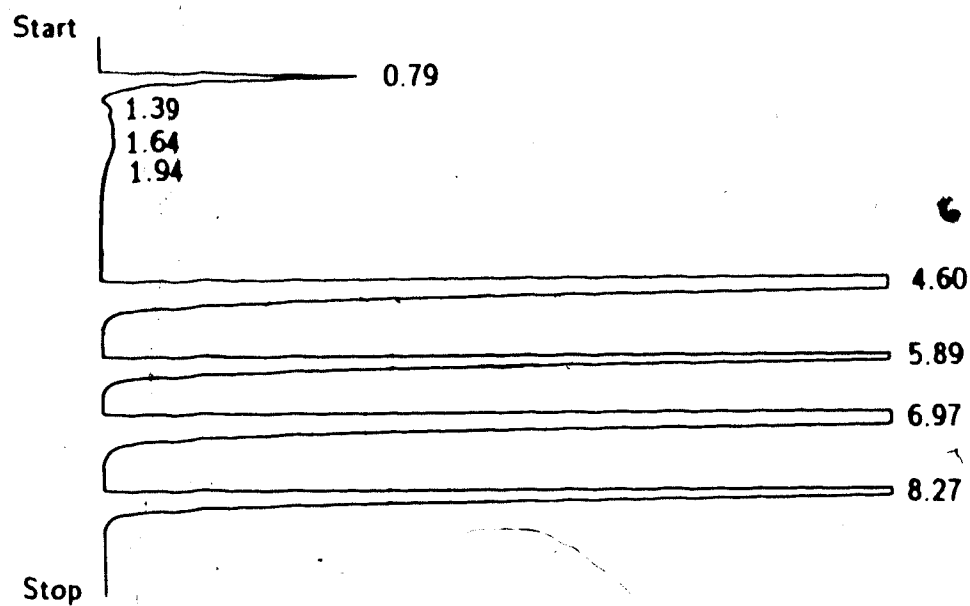
used. A char sample weighing approximately 0.1 g was connected to the adsorption apparatus in the configuration shown in Figure 2.4. The sample was immersed in a Dewar flask filled with liquid nitrogen (temperature equal to  $-196^{\circ}\text{C}$ ) for 30 minutes with gas flowing over the sample. After 30 minutes, additional adsorption could not be detected for the char samples. The liquid nitrogen was removed and the sample was immediately immersed in water at a temperature of  $20^{\circ}\text{C}$ . The nitrogen adsorbed on the sample, eluted over a period of 5 minutes, causing an imbalance in the nitrogen concentration in the gas stream which was converted to an electric signal by the thermal conductivity cell. This signal was linearly related to the concentration of additional nitrogen in the sample. The volume of gas eluted was measured and recorded on a Hewlett Packard integrator, model 18850.4. Figure 2.5 shows a typical desorption peak for a hydropyrolysis char.

After the sample was desorbed, 1 *ml* and 3 *ml* samples of pure nitrogen were alternately injected into the gas stream. The volume of gas desorbed, recorded as an area count by the integrator, was calculated by dividing the area count for the desorption peak by the area count for the 1 *ml* sample of nitrogen. The fact that the area count for the 3 *ml* sample was a factor of 3 larger than the count for the 1 *ml* sample proved that the detector response was linearly related to the additional nitrogen concentration over the volume of interest. Dividing by the known sample weight yielded the volume adsorbed per unit sample weight. The volume adsorbed was converted to nitrogen surface area using Equations 1.8 and 1.9. The barometric pressure,  $P_o$ , was recorded daily and the nitrogen partial pressure was calculated using the expression

$$P_{N_2} = 0.0978 (P_o + P_g) \quad (2.3)$$

where  $P_g$  was the sample gauge pressure measured using a test gauge ( $P$  on Figure 2.4).

To test the validity of the single point  $N_2$  surface area technique, a series of primary surface area standards supplied by Quartachrome Corp. were tested. The standards had certified surface areas of 2.6, 7.8, 48.6 and 233  $m^2/g$  covering the expected surface area range for coals and chars. Several tests were performed for each sample with 23 tests conducted in total. The measured surface areas are plotted against the true surface area in Figure 2.6. The accuracy of the technique was evaluated by applying a linear regression curve fit to the data in Figure 2.6. The fitted curve had a slope of 0.985 and an intercept of  $-0.24$ . Since the in-



| RT   | Area    | Area % |
|------|---------|--------|
| 0.79 | 390900  | 1.547  |
| 1.39 | 77000   | 0.305  |
| 1.64 | 84220   | 0.333  |
| 1.94 | 788200  | 3.120  |
| 4.60 | 8544000 | 33.817 |
| 5.89 | 3036000 | 12.017 |
| 6.97 | 9398000 | 37.197 |
| 8.27 | 2947000 | 11.664 |

Figure 2.5: Desorption Peak for Nitrogen Surface Area



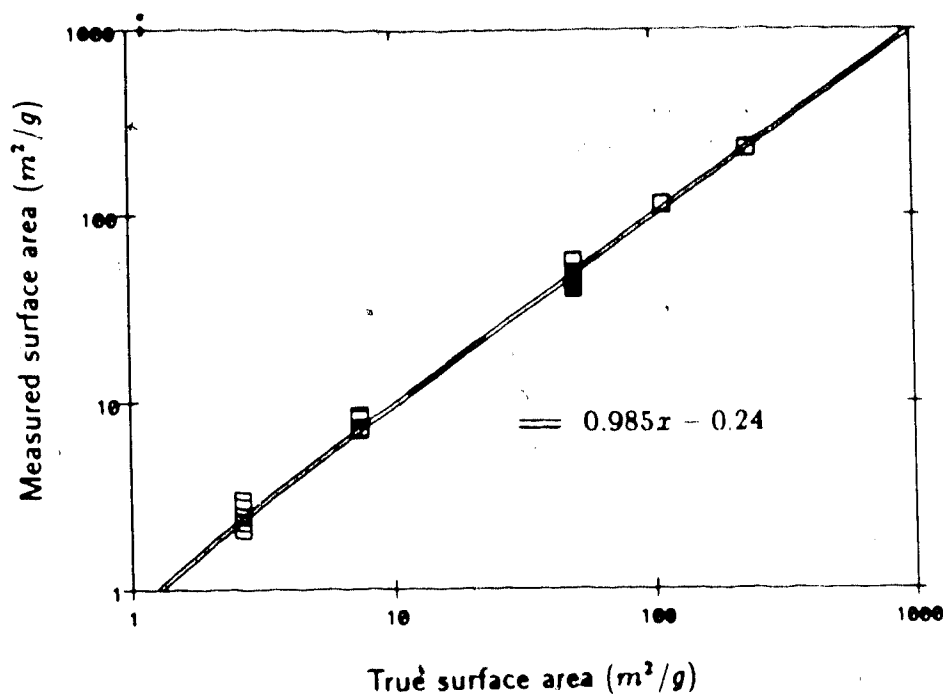


Figure 2.6: Comparison of Measured and True  $\text{N}_2$  Surface Area

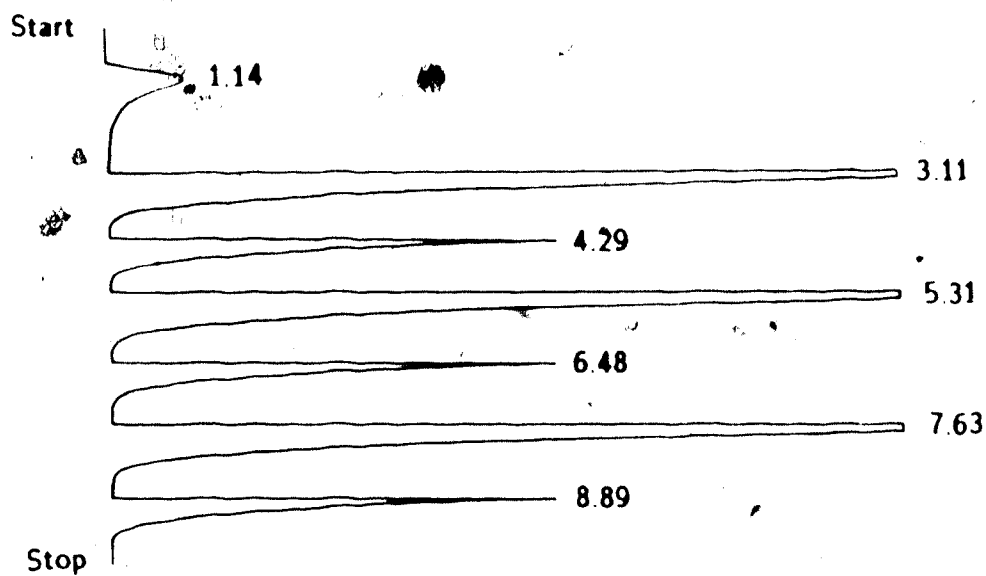
tercept should equal zero if the measured and true surface areas are equal, the significance of the non-zero intercept was evaluated using a t-test. As shown in Appendix A, there was very little evidence to suggest a non-zero intercept, and therefore, it was neglected. If the measured and true surface areas are equal, then the slope of the line should equal unity. As shown in Appendix A, the slope of the line was one standard deviation less than unity, and therefore, the measured surface area deviated from the true value. The variance in the relative error between the true and measured surface areas was calculated as 10%. Assuming a normally distributed variation in relative error, the 90% confidence in surface area measurements was  $\pm 17\%$  of the true value. For single point measurements, this was considered acceptable.

Examination of the error between measured and true surface areas in Figure 2.6

showed that error was randomly distributed over the surface area range from 2 to 50  $m^2/g$ . Somewhat better agreement between measured and true values was obtained for samples with surface area in excess of 100  $m^2/g$ .

For carbon dioxide surface area measurements, two standard calibration gases supplied by Matheson Gas Products Canada containing  $9.19 \pm 0.10\%$  and  $10.16 \pm 0.20\%$   $CO_2$  in helium were used. The same char samples used for  $N_2$  surface area measurement were dried, weighed and installed in the adsorption apparatus. The sample was immersed in a Dewar flask filled with water maintained at  $25^\circ C$  for 45 minutes. After this time, no detectable increase in  $CO_2$  adsorption was measured for the chars considered here. After adsorption was complete, the sample was immersed in a flask filled with mineral oil heated to a temperature of  $150^\circ C$ . The eluted carbon dioxide caused an imbalance in the  $CO_2$  content of the two gas streams and was recorded as a desorption peak on the integrator. One and three ml samples of pure  $CO_2$  were alternately injected into the stream 2 to determine the volume of  $CO_2$  desorbed. A plot of the integrator response is shown in Figure 2.7. The desorption of  $CO_2$  from the sample was generally complete in 5 minutes.

The  $CO_2$  surface areas were calculated using Equations 1.14 and 1.15. Unlike the  $N_2$  surface area, the technique for measuring  $CO_2$  surface area involved extrapolating a line from experimental data, to the intercept on a log volume adsorbed versus  $[\log P_o/P]^2$  plot. In this case, multipoint measurement was required to obtain acceptable accuracy from the extrapolation. A typical  $CO_2$  surface area plot is shown in Figure 2.8. Approximately twelve desorption points were taken to



| RT   | Area    | Area % |
|------|---------|--------|
| 1.14 | 2083000 | 5.023  |
| 3.11 | 9552000 | 23.033 |
| 4.29 | 3647000 | 8.794  |
| 5.31 | 9378000 | 22.613 |
| 6.48 | 3689000 | 8.958  |
| 7.63 | 9590000 | 23.125 |
| 8.89 | 3532000 | 8.517  |

Figure 2.7: Desorption Peak for CO<sub>2</sub> Surface Area

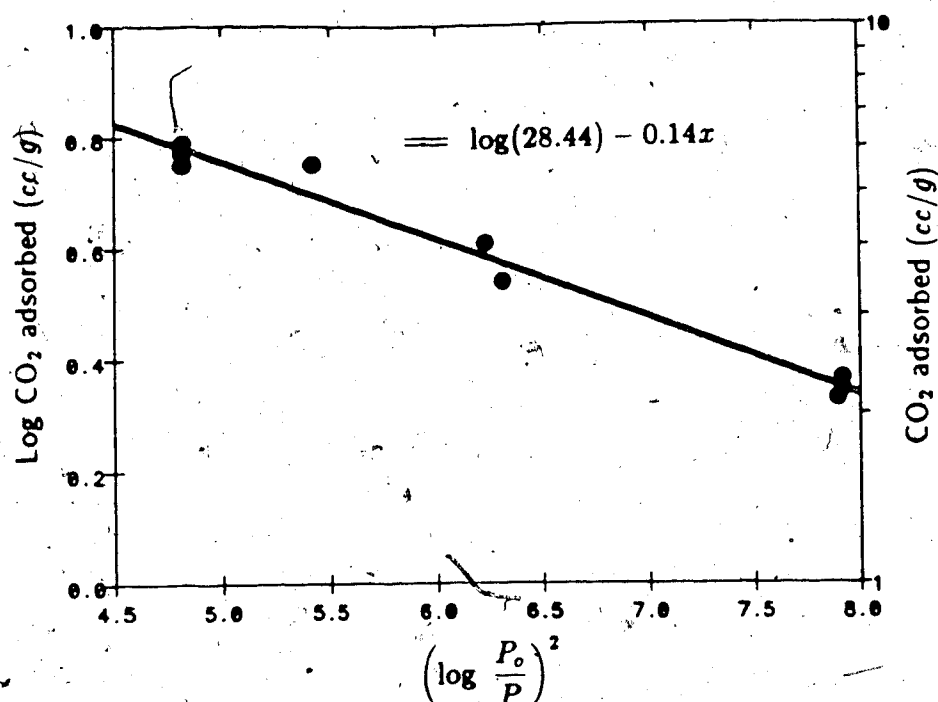


Figure 2.8: Typical Dubinin-Polanyi Plot for CO<sub>2</sub> Surface Area

construct the curve fit using the Dubinin-Polanyi Equation in the plot with four points at each of three CO<sub>2</sub> partial pressures.

The adsorption/desorption sequence was completed at 0.1 and 0.3 MPa sample gauge pressure for each of the two gases. This procedure was chosen to allow an overlap in test results for the 5 and 10% CO<sub>2</sub> in helium test gases. The value of  $[\log^2 P_0/P]$  was identically equal for 5% CO<sub>2</sub> in helium gas, at a pressure of 0.3 MPa gauge and 10% CO<sub>2</sub> gas in helium at a pressure of 0.1 MPa gauge (an abscissa value of 6.2). For all chars, the volume of gas adsorbed was equal at the overlap point proving that the adsorption was not dependent on the fraction of CO<sub>2</sub> in the test gas. This procedure required two days to complete due to the long adsorption times for each point.

No standards were commercially available to calibrate the CO<sub>2</sub> surface area technique so that the results on the CO<sub>2</sub> adsorption technique are presented here without verification. To test the precision of the measured surface area, a non-linear regression analysis was applied to the data of multipoint measurements. The range in standard deviations from the calculated CO<sub>2</sub> surface areas, summarized in Appendix C, was  $\pm 5 - 13\%$ . Therefore, assuming a normally distributed variation in percent error, the range in the 90% confidence interval for CO<sub>2</sub> surface area measurements was  $\pm 9 - 22\%$  of the measured value.

## 2.2 Intrinsic Oxidation Reactivity - Thermogravimetric Analysis

To evaluate the oxidation reactivity of hydrolysis chars prepared in this laboratory a technique was developed using a thermogravimetric analyser (TGA) manufactured by DuPont Instruments, Model No. 951. A schematic of the unit is given in Figure 2.9.

A standard analytical technique was adopted to measure the oxidation reactivity of char samples. Originally, a 10 mg sample of char was placed in a platinum foil pan on the end of a quartz balance beam connected to an electromagnetic balance. The sample was heated in helium to its operating temperature before injecting air at a flowrate of 70 ml/min. The furnace operating temperature was increased from 30°C at a rate of 10°C/min until the sample was burned out. As

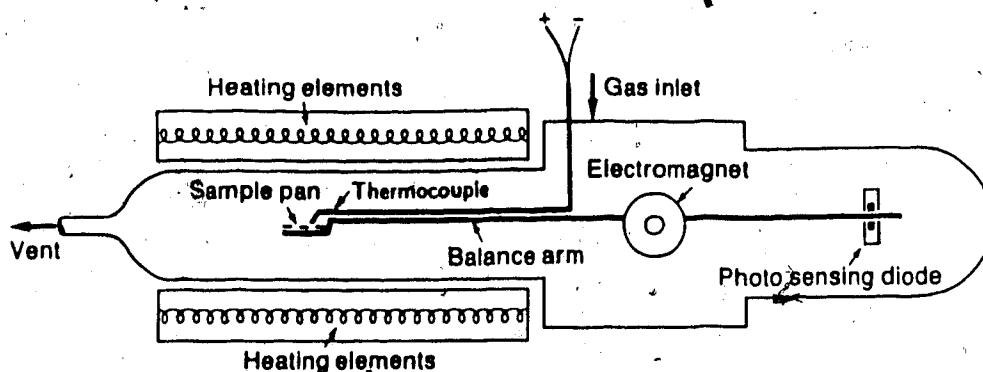


Figure 2.9: Schematic of the Thermogravimetric Analyser

the sample reacted, the weight loss as a function of time was recorded on a Dupont Instruments, Model 1090 microprocessor. The data were used to calculate the rate of weight loss and conversion vs time plots shown in Figure 2.10.

During preliminary testing, a maximum rate of weight loss of sample was observed even though the gas temperature continued to rise. This occurred at 20% conversion of the sample. Since rate of weight loss should increase exponentially with temperature according to Arrhenius kinetics, the reaction was suspected to be controlled by diffusion limitations. A simplistic model of the sample in the pan with gas flowing over the surface of the pan was formulated and the limiting rate of oxygen diffusion to the sample surface was calculated. It was found that the theoretical limit of oxygen diffusion to the surface agreed with the observed maximum reactivity of the sample. These calculations, reproduced in Appendix B, confirmed that the reaction of these samples could be limited by diffusion at temperatures well below 500°C. The limit corresponded to 72 mg/hr of char consumption. In order to limit the effects of oxygen diffusion and to eliminate temperature gradients

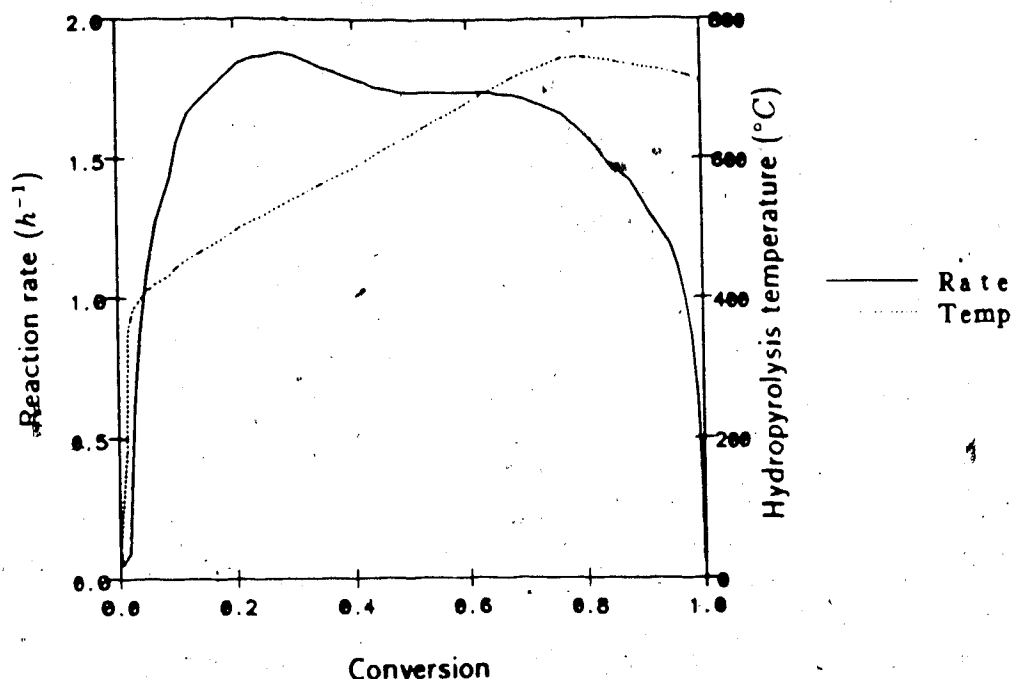


Figure 2.10: Rate of Weight Loss and Temperature for Initial TGA Tests

between the sample and the furnace, it was decided to limit the rate of oxidation to 6  $mg/hr$  or 8% of the diffusion limit. For a 10  $mg$  sample, this would require a minimum of two hours to complete each run. This was considered excessive as online disc storage for realtime data collection on the microprocessor was limited. To reduce the run time length, the sample size was reduced to 3  $mg$  so that a single run could be completed in one hour.

The effect of gas flow on the rate of sample oxidation was tested. Gas flow was varied from 50 to 1000  $ml/min$  at identical test conditions. The resulting rate of weight loss versus gas flow data is shown in Figure 2.11. At gas flowrate below 100  $ml/min$ , the rate of oxidation was limited by diffusion of oxygen to the sample. Above 200  $ml/min$  the rate of weight loss was independent of gas flowrate.

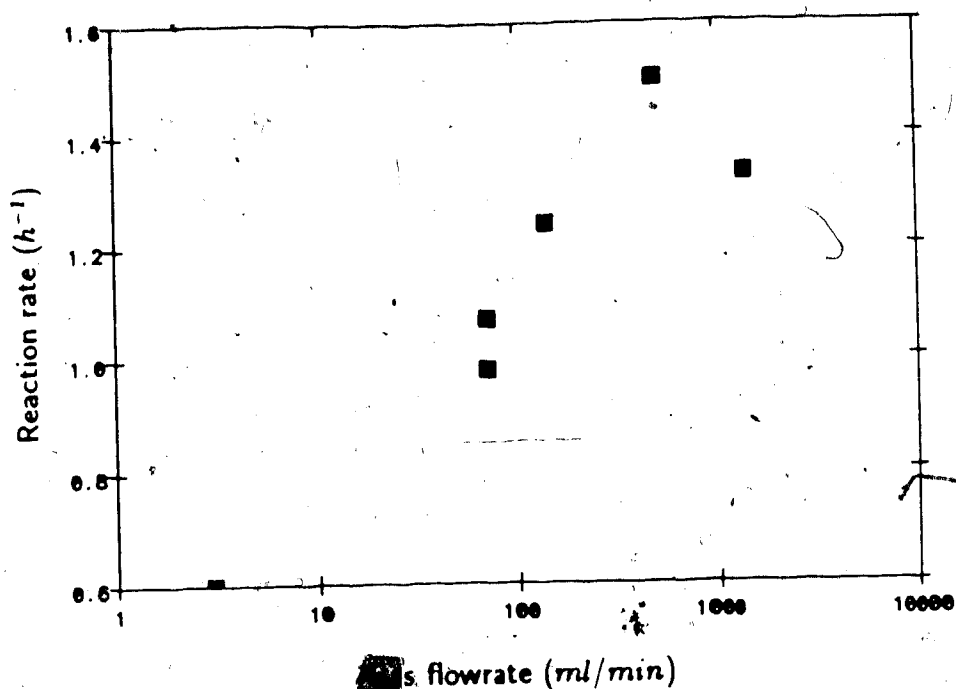


Figure 2.11: Effect of TGA Gas Flowrate on Reaction Rate

However, at gas flow exceeding 500 *ml/min*, the gas would not be adequately preheated before reaching the sample. This was apparent from the discrepancy in temperature measured from a thermocouple located near the heating elements and the thermocouple positioned directly above the sample. Without equal gas and furnace element temperature, the sample temperature would be difficult to evaluate. Therefore, a compromise in gas flowrate of 200 *ml/min* was chosen, where temperature gradients and diffusion limitations were minimized.

Using helium to preheat the sample was a problem in that the difference of thermal capacity between helium and air caused a larger reduction in thermal load when the helium was replaced with air during an oxidation test. Upon switching from helium to air, the furnace temperature controller would require at least 10



minutes to equilibrate at the same temperature. The unsteady temperature made analysis of the data complicated as the rate of weight loss could vary significantly during this time. To eliminate temperature fluctuations, the sample was preheated with nitrogen. Since the tests were all conducted below 700 K, the nitrogen was assumed to be inert. With this modification, the furnace temperature would not change upon switching from nitrogen to air.

The effect of oxygen diffusion within the sample on the pan was tested by performing comparative tests using the conventional pan or a 400 mesh stainless steel screen which would allow oxygen access to the char from above and below the sample. The rate of weight loss was unaffected by the type of sample container indicating that diffusion within the 3 mm sample was not a problem. This was confirmed by the results of the diffusion process described in Appendix B. No sample dropped from the stainless steel screen during the test suggesting that both containers were suitable for the reactivity tests. The stainless steel screen had a residual benefit in that the low frontal area to the gas flow eliminated fluctuations in the measured weight from the pan. The net effect was to make the 1  $\mu g$  reading steady whereas the 10  $\mu g$  reading was the lowest useful digit when using the pan. Therefore, the stainless steel screen was adopted for all reactivity tests.

The final procedure adopted for all oxidation reactivity tests was:

1. A 3 mg sample of char was spread evenly across a 400 mesh stainless steel screen and placed on the quartz balance beam of the TGA.
2. A quartz tube was installed around the balance beam and the entire assembly,

was positioned inside the TGA furnace.

3. Nitrogen was introduced into the tube at a flowrate of 200 ml/min.
4. The furnace temperature was raised at 100°C/min to within 15°C of the pre-determined reaction temperature. The heating rate was reduced to 10°C/minute until the reaction temperature was reached, then held constant for 10 minutes.
5. The nitrogen was replaced with air at a flowrate of 200 ml/min and the temperature and weight were recorded on the microprocessor as a function of reaction time.
6. After completing the reactivity test the sample temperature was raised by 200°C to burn out the residual carbon and to measure the ash content of the sample.

Since the oxidation reactivity tests began, no further changes have been made to the experimental procedure.

The reactivity of the sample was determined from the recorded weight loss vs time data. The overall char reaction kinetics were correlated with the expression:

$$RR = -\frac{1}{1-\chi} \frac{d\chi}{dt} = K_o c_o^n \quad (2.4)$$

where  $c_o$  was the ambient concentration of the reactive gas,  $n$  was the apparent order of reaction with respect to reactant partial pressure,  $K_o$  was the apparent overall rate coefficient and  $\chi$  was the conversion of organic matter in the char. The reactivity,  $RR$  could be related to the reactivity based on the available internal surface area by the expression:

$$RR = \eta s_a k_r c_o^n \quad (2.5)$$

If the reactivity was slow enough, the effectiveness factor would approach unity ( $\eta \rightarrow 1$ ) and the reactant gas concentration on the internal surface could be equated to the free stream value ( $c_s = c_o$ ). Equating Equations 2.4 and 2.5 gave:

$$K_o = s_a k_c \quad (2.6)$$

where the observed overall reaction rate was related to the chemical reaction rate constant,  $k_c$ , by the total internal surface area of the particle. Therefore, calculation of the chemical reactivity of the particle from observed rates required that the effectiveness factor of the particle approach unity.

Several investigators 26,39,43,35 have used thermogravimetric analysis to calculate the chemical reactivity of coals and chars. All of the studies involving char oxidation were performed at temperature less than 850 K. This was to ensure that the system was reacting under kinetic control. However, early investigators utilized large samples in confined pans which could have restricted the reaction by limiting bulk diffusion of oxygen to the particle surface. The large samples would also result in significant temperature differences between the char and the thermocouple located above the sample. In early experiments, Tseng & Edgar 43 reported that significant concentration and temperature gradients existed in the boundary layer above the sample when 30 - 40 mg samples were used. They later reduced their sample size to 2 - 9 mg to minimize the gradients. After 1982, most researchers limited their sample sizes to less than 10 mg.

The extent of diffusion control of the reaction may also be affected by the total reaction rate and the physical nature of the sample. Radovic & Walker 35 studied

the reactivity of Saran char using TGA. This char, which contained essentially all micropores, provided less access to oxygen on the internal surface than typical coal chars oxidized under similar conditions (ie the Saran char had a lower effectiveness factor). The investigators concluded that below an observed reaction rate of  $3 \text{ g/g} \cdot \text{h}$ , the process was chemically controlled. Therefore, investigators studying chemical reaction of chars should maintain their reaction rate at less than  $3 \text{ g/g} \cdot \text{h}$  as a conservative estimate of complete kinetic control of the reaction. This upper limit for reaction rate was adopted in this work.

## 2.3 Combustibility - Entrained Flow Combustor Development

To measure the combustibility of hydropyrolysis chars at conditions approaching those found in a utility boiler, an entrained flow combustor (EFC) was developed and used. The use of entrained flow combustors for combustion tests was pioneered by Field [71,72] who used this type of apparatus to show that char burnout was strongly dependent on the original coal type. Smith and coworkers [31,32,53,54] refined the combustor design and were successful in using their own apparatus to understand the nature of pore oxidation during char combustion. Entrained flow combustors are now widely used by boiler manufacturers as a boiler design tool with excellent success [73,74]. The purpose of entrained flow combustors is to study the behaviour of a particle gas suspension at carefully controlled conditions of

reactor temperature, particle residence time and gas composition. Generally, coals or chars are injected into a preheated gas stream to raise the particle temperature rapidly. The particle is reacted for a known length of time then quenched in a probe. The stoichiometric air ratio is maintained at a value in excess of 5 to ensure that gas composition remains constant during combustion and that the oxidation reaction does not significantly raise the gas temperature. If these conditions are met, the reactor may be suitable for detailed kinetic studies of char oxidation at conditions relevant to pulverized coal combustion boilers.

A schematic of the final apparatus configuration used in this work is shown in Figure 2.12. The apparatus consisted of a solid feed system, an isothermal high temperature reactor and a solids collection filter. A fluidized bed feeder, developed by Knill 70, was used to feed the char (see Figure 2.13). The feeder was a long cylindrical vessel constructed of pyrex glass. A sintered glass disc was fitted near the bottom of the feeder which was used to support the coal or char particle bed.

Air was injected from below the disc through a Kovar fitting, manufactured by Ace Glass Inc., to fluidize the particle bed. This gas exited the feeder through a filter at the top. A 1.5 mm stainless steel tube intersected the particle bed 15 mm above the fitted glass disc. A 1 mm hole was drilled in the tube and positioned, facing up in the center of the bed. To feed char, transport air was passed through the tube at a flowrate of 0.5 l/min to carry char particles to the high temperature reactor. The fluidizing gas flowed at a rate of 4 l/min through the particle bed. A slight restriction on the fluidizing gas exit caused the bed to pressurize slightly.

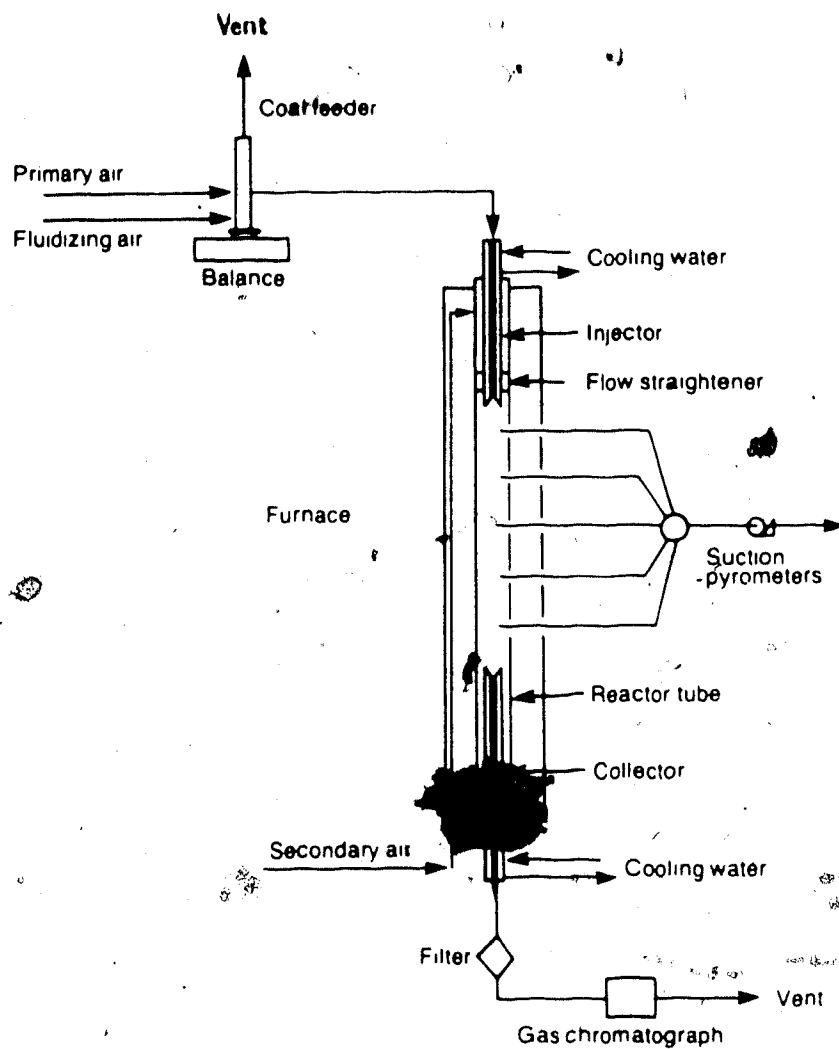


Figure 2.12: Schematic of the Entrained Flow Combustor

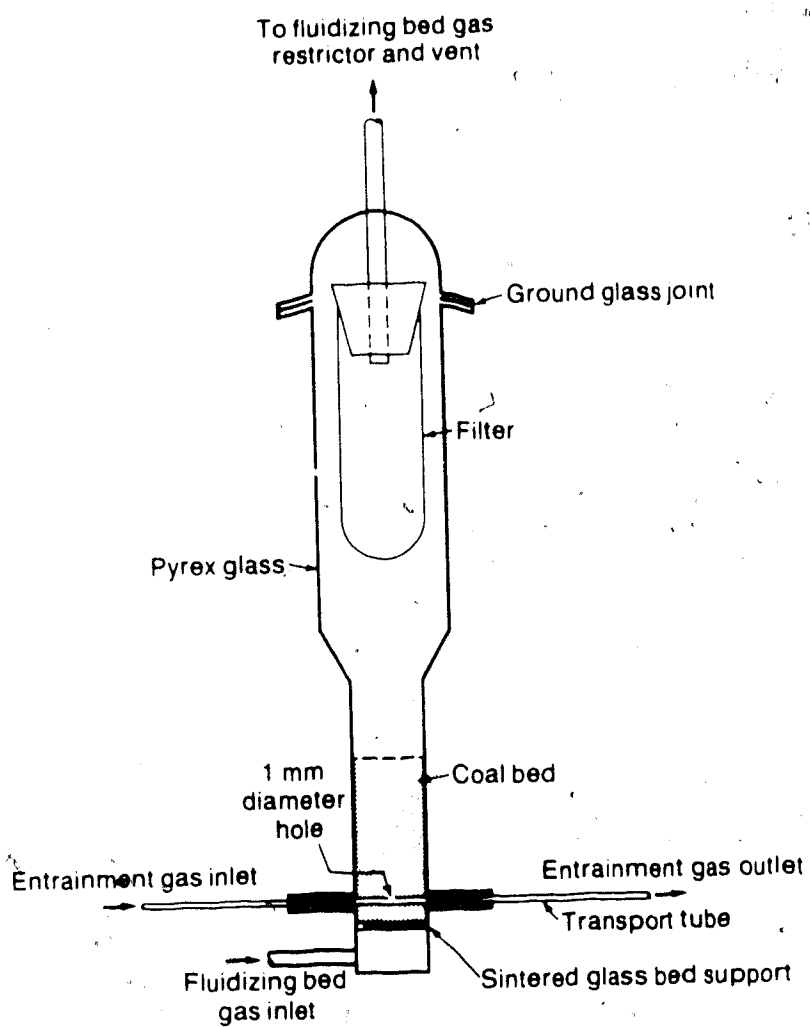


Figure 2.13: Schematic of the Fluidized Bed Coal Feeder

This pressure caused some fluidizing gas and particles to flow into the transport tube where they were entrained with the primary air. By adjusting the restriction on the fluidizing gas exit, the particle flowrate could be accurately controlled over the range of 0.02–0.10 g/min. The feeder was positioned on a Mettler Instruments Corp., Model PE 1600 balance to continually measure the weight of the char and feeder.

The reactor was a 25.4 mm stainless steel tube fitted with a 1.5 mm O.D. by 3.2 mm I.D. water cooled injector probe at the top and 1.5 mm O.D. by 6.4 mm I.D. collector probe at the bottom. The reactor was placed inside a three zone Lindberg Model 54287-S furnace, manufactured by General Signal Corp., capable of heating the reactor to 1200°C. The reactor design is shown in Figure 2.14. The probes were constructed from three concentric stainless steel tubes. The cooling water entered the probe through the inner annulus and exited from the probe through the outer annulus. The flowrate of water was adjusted to maintain its exit temperature near the boiling point. This procedure minimized the heat loss from the reactor through the probes. The probes were fitted with conical caps to minimize flow disruption during injection and collection of char particles. The entire probe assembly was welded together except for the fitting between the inner and outer tubes at the back of the probe. As there could be severe temperature gradients between the inner and outer tubes, this joint was allowed to rotate freely in a fitting to prevent thermal stresses from rupturing any of the welded joints. The injector was fitted with a flow straightener constructed from a 10 mm thick



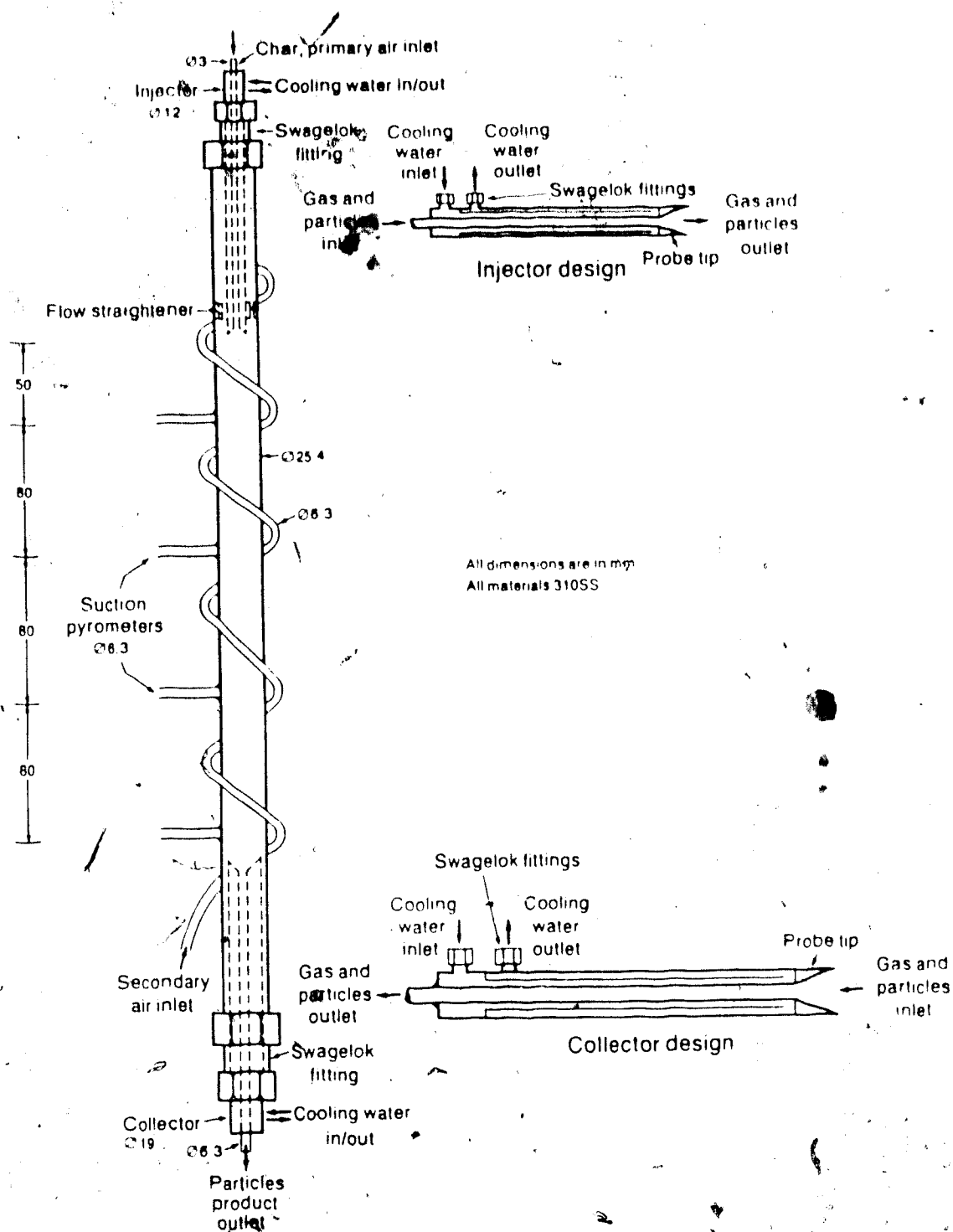


Figure 2.14: Detailed Entrained Flow Combustor Reactor Design

disc of stainless steel with evenly spaced 1.5 mm holes drilled through. The flow straightener was used to ensure that the secondary airflow was evenly distributed across the full cross-section of the reactor.

The injector and collector were fitted into the 25.4 mm reactor as shown in Figure 2.14. The secondary air was preheated in a 6.4 mm O.D. stainless steel tube wrapped around the reactor tube and injected into the reactor above the flow straightener. Gas temperature was measured from the 6.4 mm suction pyrometer ports welded to the reactor at 50, 130, 210 and 290 mm downstream from the injector. For temperatures exceeding 1000°C, radiative heat transfer from a bare thermocouple to the walls of the reactor maintained at a different temperature becomes appreciable<sup>75</sup>. To reduce the effects of radiative heat transfer and to measure the correct gas temperature, the thermocouple must be shielded from radiative heat transfer with other bodies. This was accomplished by installing a radiation shield around the thermocouple tip. At the same time, the convective heat transfer to the thermocouple tip may be increased by aspirating hot gas across it at a high velocity. In this way, a close approximation of the true gas temperature may be attained. Suction pyrometers were constructed from a 3.2 mm O.D. stainless steel tube covering a 1.6 mm, unshielded Chromel-Alumel (k-type) thermocouple (see Figure 2.15). To measure gas temperature, reactor air was aspirated through the tip of the probe and across the unshielded thermocouple. The flowrate of air was adjusted by a valve located before the aspirating pump and was measured using a calibrated rotameter. To obtain the true reactor

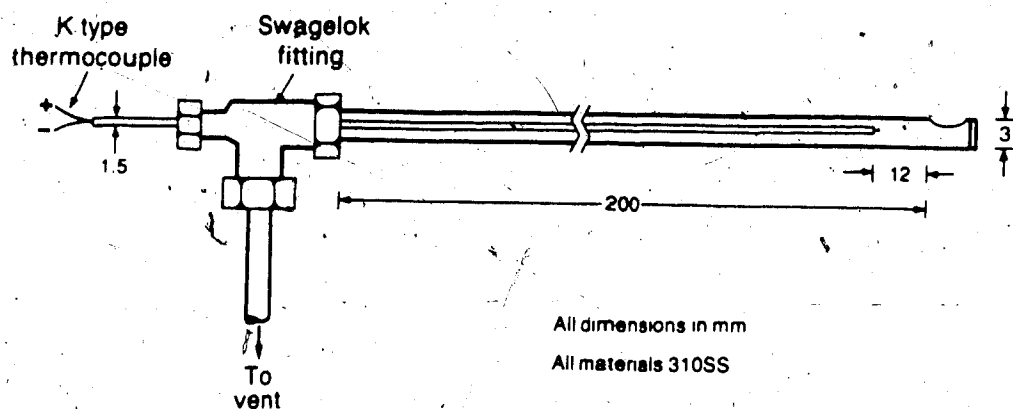


Figure 2.15: Detailed Suction Pyrometer Design

gas temperature, the aspiration rate was increased until there was no change in gas temperature at higher gas flowrates. A plot of the suction pyrometer measurements at the two temperature stations along the reactor is shown in Figure 2.16 for a reactor wall temperature of  $1100^{\circ}\text{C}$ . Above a gas flowrate of  $300\text{ ml/min}$ , no appreciable change in gas temperature was recorded. This flowrate was used for all subsequent gas temperature measurements.

The residence time in the reactor was adjusted by varying the distance between the injector and the collector. In these tests, the position was fixed and the collector was positioned accordingly. Reaction zone lengths could be adjusted from 100 to 350 mm.

In the tests conducted here, the coal was injected with transport air at a flowrate of  $0.5\text{ l/min}$ . This primary stream was mixed with the secondary air which was introduced in the annulus between the injector and the reactor at a flowrate of  $4\text{ l/min}$ . An isothermal reaction zone temperature of either 760 or

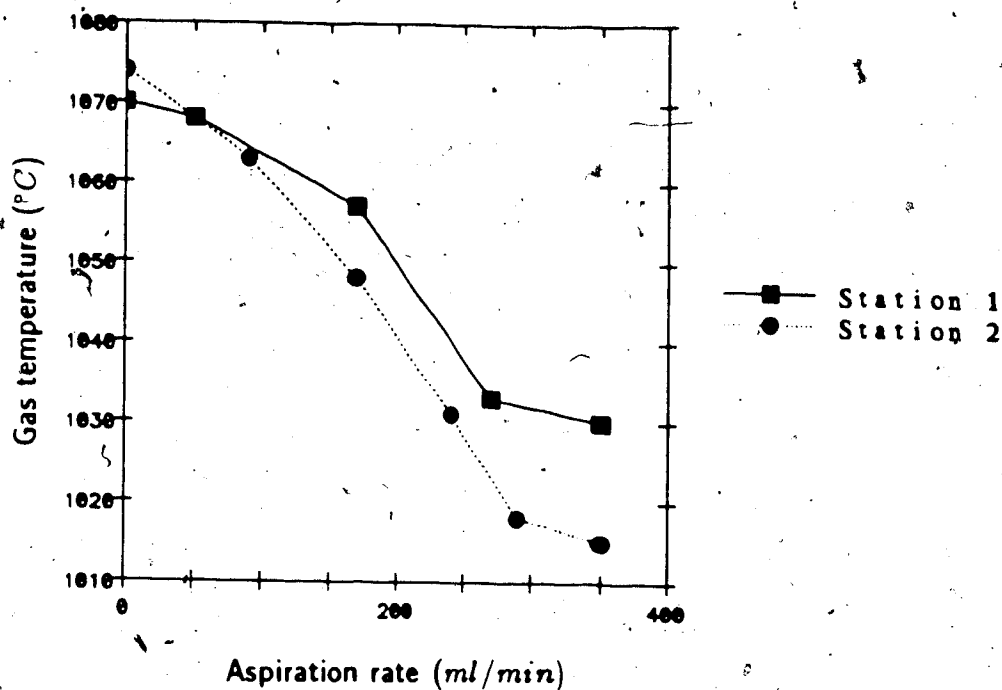


Figure 2.16: Effect of Aspiration Rate on Gas Temperature Measurement

1050°C was attained for all char runs. This isothermal zone was obtained by adjusting the temperature setpoints of the three zones of the Linbergh furnace. Because of the position of the water cooled injector, the top furnace element had to be operated at a temperature of 900 or 1200°C. Therefore, the secondary air would enter the reactor at the higher temperature and cool down to the reaction setpoint as it passed through the flow straightener.

The velocity of the coal entering the reactor was 4 m/s and of the secondary air was 1 m/s. This caused the coal to enter in the form of a jet and spread evenly across the reactor cross-section, mixing rapidly with the preheated secondary stream. The jetting action also ensured that the particles were injected directly into the isothermal reaction zone increasing the particle heatup rate.

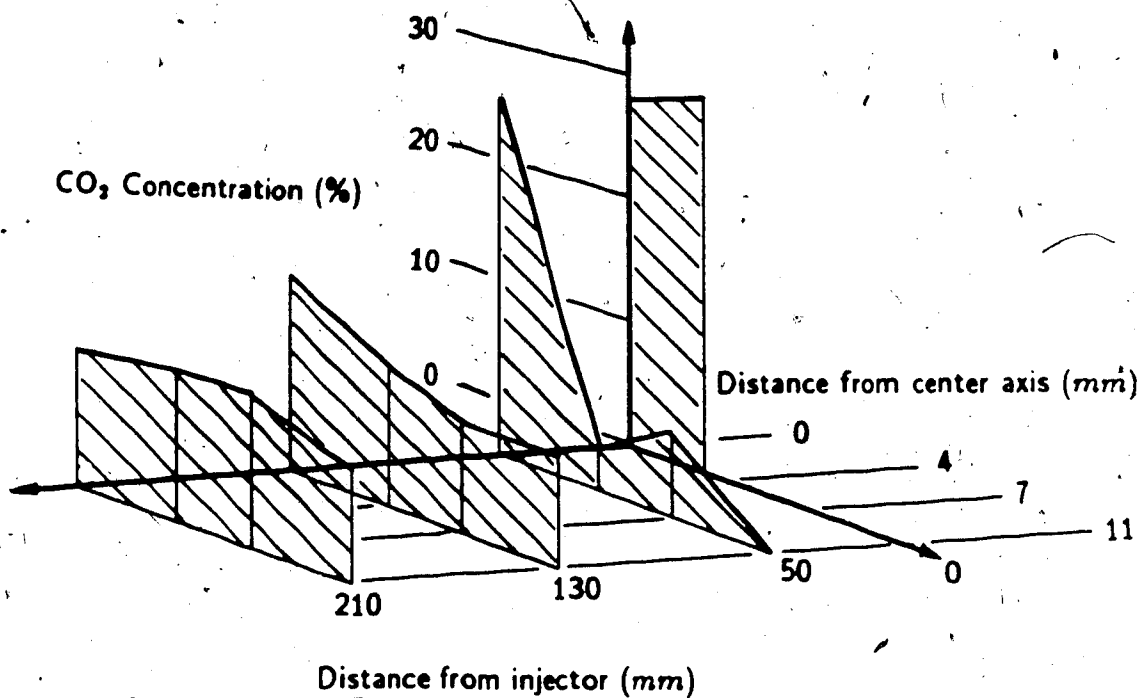


Figure 2.17: CO<sub>2</sub> Tracer Measurement in the EFC

The rate of mixing of the primary and secondary air streams was measured by injecting CO<sub>2</sub> through the injector at a flowrate of 0.4 l/min and air through the annulus at a flowrate of 4.0 l/min. The radial concentration of CO<sub>2</sub> was measured at the suction pyrometer ports. The concentration distribution is shown in Figure 2.17. Mixing was not appreciable until the second pyrometer station, 130 mm from the injector and was not complete until 210 mm from the injector. Assuming that heat and mass transfer processes are similar (ie. Lewis No. 1) the radial temperature distribution of the gas stream should not be uniform until 210 mm from the injector. Indeed, this was observed in the temperature profiles measured during testing. The temperature 50 mm from the injector was consistently 30 – 60°C less than the temperature recorded at all other stations.

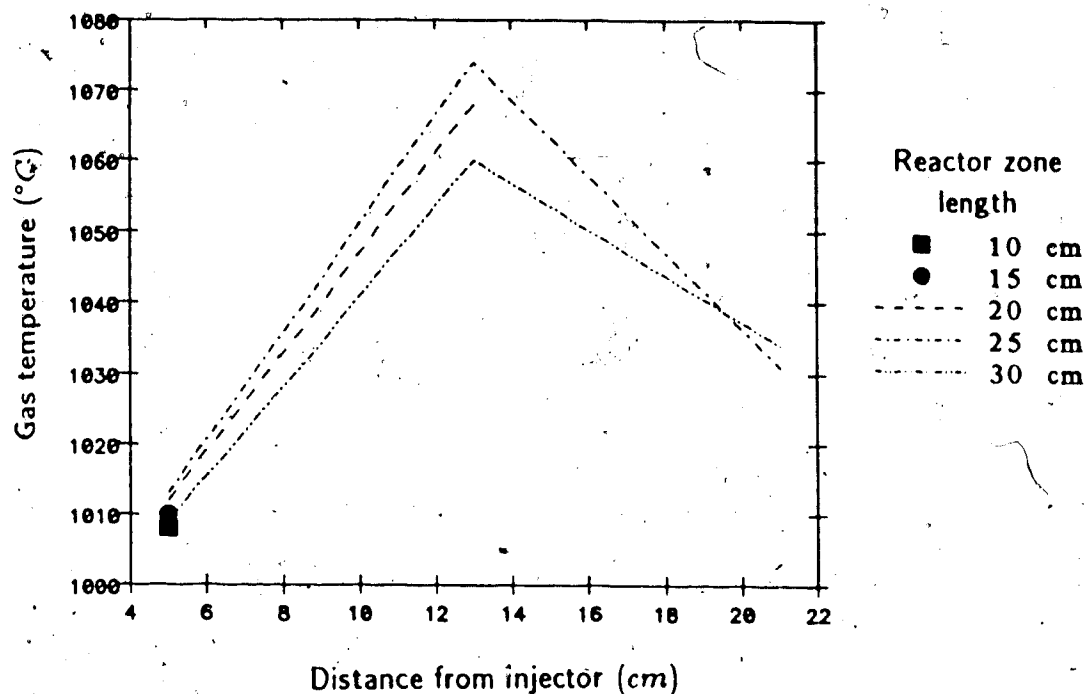


Figure 2.18: Temperature Profile in the EFC

A profile of the temperature distribution in the reactor for various zone lengths is shown in Figure 2.18. The temperature could be maintained within a 25°C window throughout the reaction zone. Better control was not attempted as this profile was considered acceptable.

The particles were collected in a Balston filter connected to the end of the collector. The residue in the filter was removed and its ash content was determined. The particle conversion was calculated from an ash balance of the feed char,  $ash_{char}$ , and the residue,  $ash_{res}$ . Assuming that all ash remained in the particle, the mass of ash in the char and residual particles were equal. This equality was related to the carbon conversion according to the expression:

$$\chi_{daf} = \frac{1 - ash_{char}/ash_{res}}{1 - ash_{char}} \quad (2.7)$$

where  $\chi_{daf}$  was the conversion of organic matter in the char on a daf basis. Significant errors could have occurred from this method if the particle temperature exceeded 1300°C due to volatilization of certain ash components [76]. However, in the tests reported here, the particle temperature did not exceed 1300°C so that these errors were neglected.

Evaluating solid reactivity using an entrained flow system required calculation of the particle temperature. Particle temperature depended on the heat generation and loss from the particle, which changed rapidly along the length of the combustor. Therefore, a numerical model was developed to evaluate the temperature, based on the experimentally measured rate of particle burnout. Also, the residence time of the particle was calculated from knowledge of the gas and solid velocity, both of which depend on the combustion behaviour.

To evaluate the particle temperature and residence time, the conservation equations of mass, momentum, energy were solved along with assumed chemical kinetics. Since particle Reynolds number was always less than unity, particle velocity was calculated assuming that the particles moved in the stokes flow regime. The conservation equation was:

$$\frac{dv}{dt} = g - \frac{9\mu v}{2R_p^2 \rho_a} \quad (2.8)$$

where  $R_p$ ,  $v$ ,  $\rho_a$  were the particle radius, velocity and density, respectively,  $\mu$  was the gas viscosity and  $g$  was the gravitational constant.

The particle temperature was calculated from a balance of heat generation due to internal reaction, heat loss due to radiation to the furnace walls and convection

to the surrounding gas according to:

$$\frac{dT}{dt} = \frac{12}{c_P} \left[ \frac{H}{1 - \chi_{TOT}} \frac{d\chi_{FC}}{dt} - \Phi_1(T_P - T_o) - \Phi_2(T_P^4 - T_w^4) \right] \quad (2.9)$$

where  $c_P$ ,  $\chi_{FC}$ ,  $\chi_{TOT}$ ,  $H$  and  $T_P$  were the particle specific heat, fixed carbon conversion, total conversion, heat of reaction and temperature, respectively.  $T_o$  and  $T_w$  were the gas and wall temperature and  $\Phi_1$  and  $\Phi_2$  were heat transfer factors due to convection and radiation, respectively. Convective heat transfer was calculated assuming that the Nusselt number was equal to 2. The radiative heat transfer was calculated assuming that the particles behaved as grey bodies with an emissivity equal to 0.8. The specific heat was a function of the ash and organic content of the solid as well as the temperature. A suitable expression for the generation of heat required a knowledge of the combustion products. For all chars, the carbon content was 81 – 94% with the remainder being hydrogen, oxygen and nitrogen. Most of the hydrogen and oxygen would be concentrated in the volatile matter and would be released prior to combustion of the solid residue. Therefore, the residue may be assumed to be composed entirely of carbon with little error.

Either CO or CO<sub>2</sub> may be primary products of combustion. The heat generated within the particle with CO<sub>2</sub> as the only product would be 7900 cal/g and with CO as the only product would be 2340 cal/g. At high temperature CO would be the major product of combustion which would oxidize to CO<sub>2</sub> away from the particle so that it would not contribute directly to heat generated within the particle.



Mulcahy[28] showed the expression:

$$\Gamma = \left[ 1 + 2500 \exp \left( -\frac{12400}{RT_P} \right) \right]^{-1} \quad (2.10)$$

where  $\Gamma$  was the fraction of primary oxidation product as  $\text{CO}_2$ , agreed with the measured products in a combustion furnace. The factor  $\Gamma$  was used to determine the heat generated in the particle.

The rate of weight loss of char was assumed to be modelled by the expression:

$$\frac{d\chi_{FC}}{dt} = \frac{3 K_{TOT} c_{O_2}}{\rho_a R_P} \quad (2.11)$$

for a first order reaction with respect to oxygen partial pressure where the total reaction rate  $K_{TOT}$  was represented by the equations:

$$K_c = k_c (1 - \chi_{FC}) \quad (2.12)$$

$$K_d = \frac{2 \Gamma D_{AB}}{R} \quad (2.13)$$

$$K_{TOT} = \left( \frac{1}{K_d} + \frac{1}{K_c} \right)^{-1} \quad (2.14)$$

An expression for the rate of volatile evolution was developed from devolatilization experiments conducted on Alberta subbituminous coal[79] and incorporated into the model.

The radius and density of the particle changed with extent of combustion and needed to be evaluated for Equations 2.8, 2.9, 2.11 and 2.13. Smith[22] developed the expressions:

$$R_P = R_{P_0} (1 - \chi_{TOT})^\alpha \quad (2.15)$$

$$\rho_a = \rho_{a_0} (1 - \chi_{TOT})^\beta \quad (2.16)$$

where  $\alpha$  and  $\beta$  were experimentally determined exponents used to express the density and size changes that occurred with combustion and the subscript  $i$  referred to initial conditions. The exponents were interrelated by the equation:

$$3\alpha - \beta = 1 \quad (2.17)$$

The increase in gas temperature from combustion was also incorporated into the model with allowance made for the radiation loss from the particles to the wall and convection loss from the gas according to:

$$\dot{m} c_p \Delta T_g = q''' - q_R - q_{CONV} \quad (2.18)$$

where  $q'''$ ,  $q_R$  and  $q_{CONV}$  were the heat generated, heat transfer by radiation and by convection, respectively and  $\Delta T_g$  was the change in gas temperature flowing at a rate,  $\dot{m}$ .

These ordinary differential equations were solved simultaneously using a Runge-Kutta routine. The particle and gas temperatures, distance along the combustor and conversion of the solid were calculated.

# Chapter 3

## Results and Discussion

### 3.1 Char Surface Characterization

The chars used in this investigation were designated alphabetically from A to H. The char processed in the least severe hydrolysis condition was designated as char A and the char processed under the most severe condition was designated as char H. A summary of the process conditions for chars A-H are given in Table 3.1. Char H was only used in the TGA analysis described in Section 3.2.2. Chars A-G, representative of the range of experimental test conditions studied during the hydrolysis program, were characterized using helium density, mercury porosimetry, CO<sub>2</sub> and N<sub>2</sub> gas adsorption techniques. The surface characteristics of coal and chars A-G are listed in Table 3.2.

The true densities for all chars were within a narrow range from 1.38 to 1.56 g/cc compared to 1.47 g/cc for the original coal. There was no correlation between the process conditions and the true densities. Char G had the highest

Table 3.1: Hydropyrolysis Char Process Conditions

| Char<br>Designation | Process Conditions  |                                     |                       |
|---------------------|---------------------|-------------------------------------|-----------------------|
|                     | Temperature<br>(°C) | Pressure<br>(MPa - H <sub>2</sub> ) | Residence<br>Time (s) |
| A                   | 600                 | 3.5                                 | 2.7                   |
| B                   | 600                 | 6.7                                 | 5.0                   |
| C                   | 700                 | 3.5                                 | 0.5                   |
| D                   | 700                 | 6.7                                 | 2.4                   |
| E                   | 700                 | 10.0                                | 5.0                   |
| F                   | 800                 | 6.7                                 | 5.0                   |
| G                   | 800                 | 10.0                                | 2.7                   |
| H                   | 800                 | 10.0                                | 5.0                   |

Table 3.2: Surface Characteristics of Hydropyrolysis Chars

| Char Type | True              | Apparent          | Open Pore        | Surface Area                           |                                       | Average                |       |
|-----------|-------------------|-------------------|------------------|--|---------------------------------------|------------------------|-------|
|           | Density<br>(g/cc) | Density<br>(g/cc) | Volume<br>(cc/g) | CO <sub>2</sub><br>(m <sup>2</sup> /g) | N <sub>2</sub><br>(m <sup>2</sup> /g) | Pore Size (Å)<br>macro | micro |
| Coal      | 1.47              | 1.25              | 0.12             | 205                                    | 2.3                                   |                        |       |
| A         | 1.50              | 0.87              | 0.48             | 435                                    | 16.7                                  | 527                    | 31    |
| B         | 1.48              | 1.09              | 0.24             | 332                                    | 4.2                                   | 320                    | 20    |
| C         | 1.43              | 0.69              | 0.76             | 269                                    | 22.0                                  | 797                    | 80    |
| D         | 1.38              | 0.68              | 0.75             | 317                                    | 13.1                                  | 761                    | 67    |
| E         | 1.52              | 0.69              | 0.79             | 237                                    | 10.5                                  | 666                    | 95    |
| F         | 1.48              | 0.53              | 1.21             | 427                                    | 33.6                                  | 968                    | 80    |
| G         | 1.56              | 0.57              | 1.11             | 405                                    | 28.5                                  | 757                    | 77    |

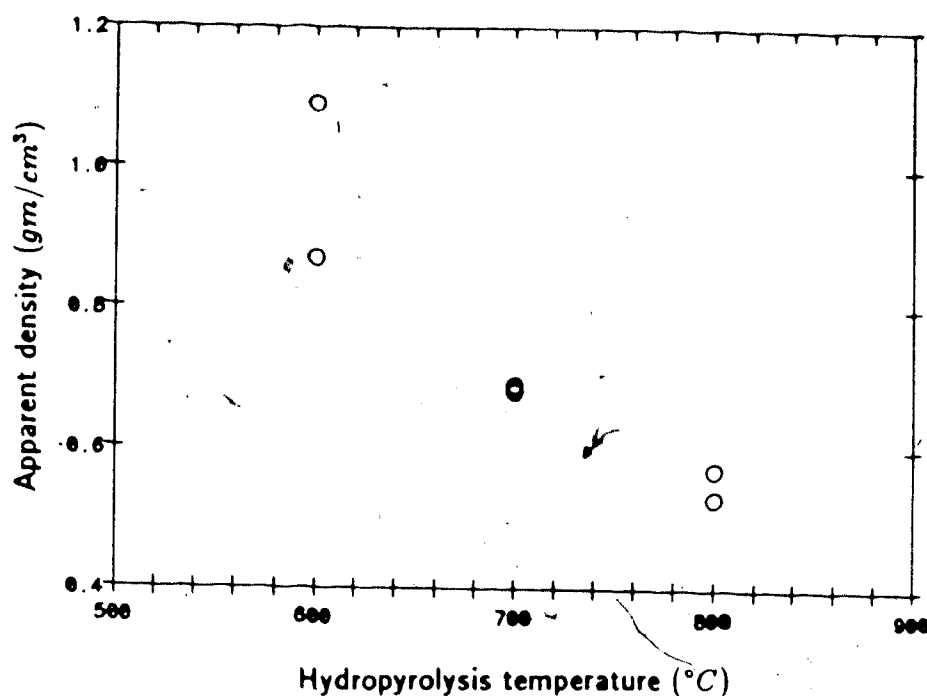


Figure 3.1: Effect of Hydropyrolysis Temperature on Char Density

density of 1.56 g/cc followed by char E (1.52 g/cc) and char A (1.50 g/cc). This observation showed that reactive gas may affect density compared to thermal effects alone since Nsakala [25] showed a gradual increase in true density from 1.5 to 1.7 g/cc with increasing residence time for American lignite chars pyrolysed in nitrogen at 808°C. Perhaps the hydropyrolysis test conditions were sufficiently narrow such that true density would not change appreciably compared to the test conditions used by Nsakala.

A summary of the mercury porosimetry experimental results is included in Appendix C. The particle apparent densities decreased with hydropyrolysis temperature from 1.09 g/cc for char B to 0.53 g/cc for char F (see Figure 3.1 and Table 3.2). The apparent density was insensitive to other hydropyrolysis process conditions. Chars C, D and E, which were all processed at 700°C but widely

different pressures and residence time had identical apparent densities.

The apparent and true densities were used to calculate the total open pore volume of the coal and chars according to Equation 1.17 (see Table 3.2). The open pore volumes increased rectilinearly with hydrolysis temperature from 0.24 cc/g for char B to 1.21 cc/g for char F compared to 0.12 cc/g for the original coal. The decrease in apparent density with increasing hydrolysis severity was also found by Cyprès et al.[77] and Johnson[28]. Cyprès et al. gasified devolatilized Belgian coal at 900°C to various conversion levels between 40 and 80 wt % daf. They showed that internal volume increased with the greatest change occurring in pores of diameter 600 to 5000 Å. Johnson showed that the total pore volume for a subbituminous coal char at 50% conversion was 1.5 cc/g which was consistent with the pore volumes in the work reported here.

The porosimeter was operated up to a pressure of 69 MPa corresponding to mercury penetration into pores 180 Å in diameter. A plot of the pore volume distribution, presented as  $dV/d(\log r)$ , versus the logarithm of pore diameter for chars B, E, G and the original coal is shown in Figure 3.2. The effect of increasing hydrolysis severity was to enlarge the volume in pores over the entire range from 200 to 10,000 Å diameter. The largest increase in pore volume occurred for pores in the range of 2000 to 10,000 Å diameter indicating that smaller pores were enlarging to pores of this size range.

The surface area distribution in all pores calculated using mercury porosimetry and gas adsorption data are shown in Figure 3.3. The surface area in pores larger

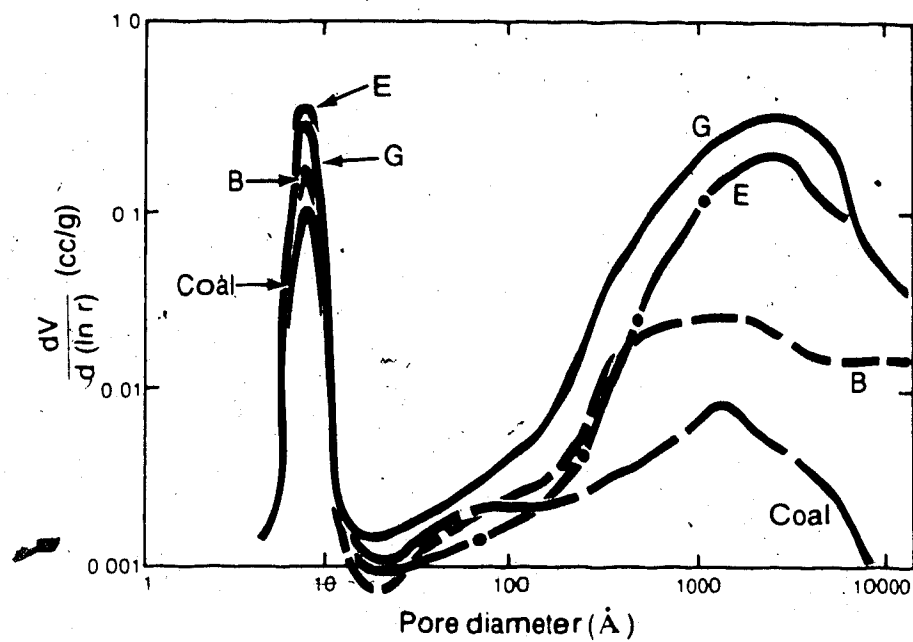


Figure 3.2: Pore Volume Distribution of Hydropyrolysis Chars

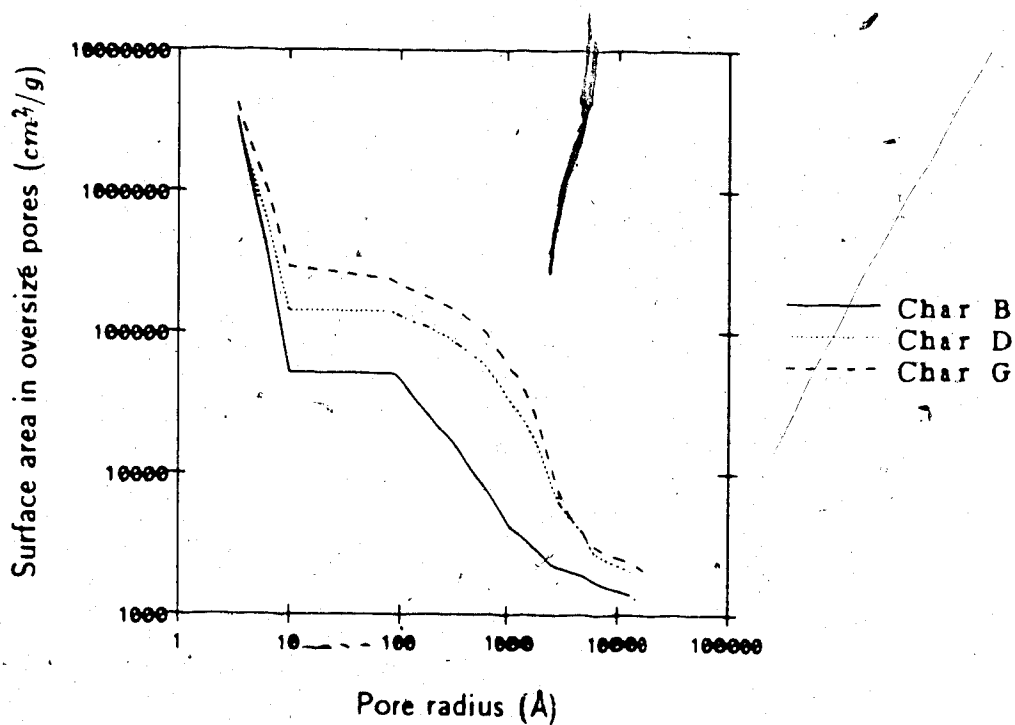


Figure 3.3: Surface Area Distribution of Hydropyrolysis Chars



than 180 Å increased from 5.1  $m^2/g$  daf for char B to 22  $m^2/g$  for char G. Assuming these pores to be cylindrical, the average macropore diameter could be calculated from the expression:

$$\bar{r}_M = \frac{2V_M}{S_M} \quad (3.1)$$

The average macropore diameters are given in Table 3.2 for selected chars. The average macropore diameter increased with temperature during hydrolysis from 320 Å for char B to 968 Å for char F. This was probably a direct result of lower char yield at higher gas temperature. The average macropore diameter also increased with lower hydrolysis pressure. This result could not be related to char yield alone. However, at lower pressure, hydrogasification should be decelerated since it is a first order reaction and the diffusion rate of hydrogen to the reacting surface would be higher. Both of these conditions would tend to increase the reaction on the internal surface of the particle, thereby enlarging the average pore diameter.

The nitrogen surface areas of the seven chars are listed in Table 3.2. The  $N_2$  surface area increased with hydrolysis severity from 4.2  $m^2/g$  for char B to 33.6  $m^2/g$  for char F. For chars B, D and E there was no difference in the surface areas measured by  $N_2$  adsorption which included pores as small as 12 Å diameter and mercury porosimetry which measured pores as small as 180 Å diameter. Only chars A and C pyrolysed at a hydrogen pressure of 3.5 MPa and chars F and G pyrolysed at a temperature of 800°C had surface area in pores between 12 Å and 180 Å as measured by  $N_2$  adsorption. This result supported the conclusion

that chars must be hydrolysed at low pressure or high temperature to open significant internal particle surface area.

The carbon dioxide surface areas of the chars are also listed in Table 3.2. The  $\text{CO}_2$  surface area increased from  $205 \text{ m}^2/\text{g}$  for coal to  $237 - 435 \text{ m}^2/\text{g}$  for the chars. The surface area was higher for chars pyrolysed at low pressure. Char A, pyrolysed at pressure of  $3.5 \text{ MPa}$ , had a surface area of  $435 \text{ m}^2/\text{g}$  compared to char B, pyrolysed at  $6.7 \text{ MPa}$ , which had a surface area of  $332 \text{ m}^2/\text{g}$ . It was concluded that at lower process pressure more internal particle surface area was opened. The  $\text{CO}_2$  surface area also increased with hydrolysis temperature. For chars B, D and G, all pyrolysed at a pressure of  $6.7 \text{ MPa}$  and two different residence times, the surface area increased from  $332$  and  $317 \text{ m}^2/\text{g}$  at  $600$  and  $700^\circ\text{C}$  pyrolysis temperature to  $427 \text{ m}^2/\text{g}$  at  $800^\circ\text{C}$ . The  $\text{CO}_2$  surface areas were lower than the surface areas reported by Johnson[28] for gasification chars prepared from American subbituminous coals. Those chars, prepared at a temperature of  $925^\circ\text{C}$ , had surface areas of  $600 - 800 \text{ m}^2/\text{g}$ . Perhaps temperature in excess of the range studied here may result in significantly higher total particle surface area.

## 3.2 Char Intrinsic Oxidation Reactivity

### 3.2.1 Nature of the TGA Oxidation

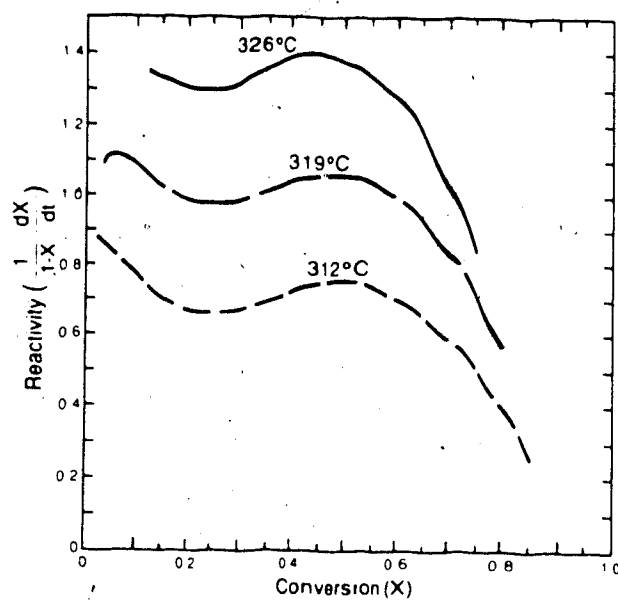
Seventeen hydrolysis char samples were oxidized under conditions of kinetic control using the TGA. The oxidation procedure was described in Section 2.3 and

burnout plots of the form shown in Figure 3.4 were produced. In general, oxidation was completed at rates of  $0.3 - 3.0 \text{ g/g} \cdot \text{h}$  at a temperature of 310 to  $400^\circ\text{C}$ .

The oxidation rate was expressed in terms of the reaction rate, ( $RR$ ), from Equation 2.4 by dividing the instantaneous rate of weight loss by the mass of unburned carbon. When plotted with respect to conversion, the reaction rate for all chars studied had two characteristic forms as shown in Figure 3.4. The first set of curves, labelled '1' had a rate which remained reasonably constant up to 60% conversion with a slight minimum at 10 – 30% conversion and decreased at higher conversion. This curve was characteristic of the reactivity for Highvale coal as well as hydropyrolysis chars with oxygen content in excess of 10% and large volatile matter contents. The second set of curves, labelled, '2', had a noticeable maximum in rate between 50 – 80% conversion. The second curve was characteristic of high severity process chars which typically had oxygen contents of less than 4%.

The high initial reaction rate of curve 1 could not be due to devolatilization of the char sample on the TGA apparatus because the sample was oxidized at several hundred degrees lower temperature than in the hydropyrolysis process. As devolatilization was essentially a thermal process, no additional weight loss would be expected during TGA tests except for drying. It is possible that the initial high rate was due to the oxidation of reactive hydrogenated and oxygenated sites on the char. Jenkins[78] reported that chars with a high hydrogen content were most reactive due to the preferential oxidation of hydrogenated sites within the char. In these test results, the minimum in the reaction rate curve probably corresponded

1



2

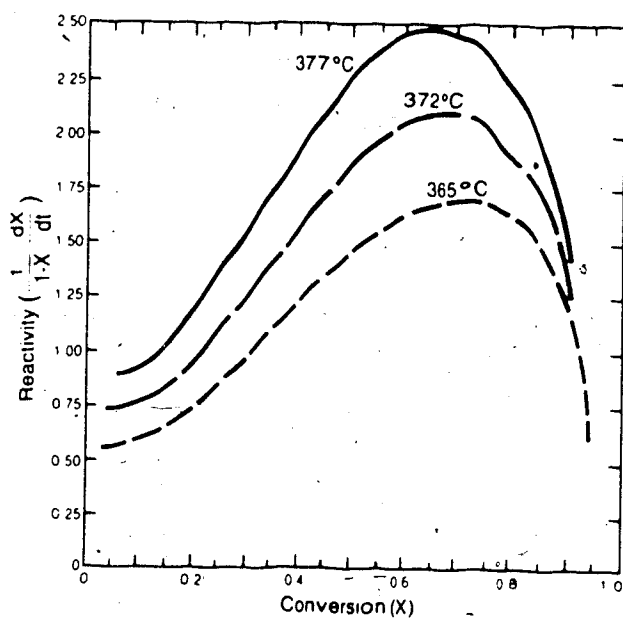


Figure 3.4: Characteristic Forms of the TGA Reaction Rate

to the depletion of hydrogenated sites.

Although the reaction rates of coal and low severity hydrolysis chars did not increase significantly to a maximum at 50–80% conversion, their reaction rates were higher than the rates for other hydrolysis chars. The higher oxygen and hydrogen content of these chars may have resulted in the higher rates.

The ratio of the initial to the maximum reaction rate varied between a factor of unity and four. The chars prepared under the most severe hydrolysis conditions had the largest increase in rate. This effect has been attributed to the opening of 'ultramicropores' above 10% conversion and the development of pore surface area during oxidation[50]. A large fraction of internal char surface area exists in the 'ultramicropores' which are approximately 5 Å in diameter and are probably atomic voids within the char structure. Oxidation in 'ultramicropores' would have been controlled by activated diffusion which was a very slow process. Walker[80] using the Lennard-Jones (6-12) potential for dispersive and repulsive energies concluded that activated diffusion was controlling when pore diameter was less than the sum of the kinetic diameter of the diffusing species plus 1.6 Å. Also, he showed that since the repulsive power varies inversely with the twelfth power of distance between the diffusing species and the surface, small increases in pore size would produce a larger reduction in the activation energy of diffusion. Once the pores had been enlarged to the critical size where activation energy of diffusion decreased, diffusion rate and mass reactivity would increase.

The surface area developed during oxidation probably reached a maximum

between 30 – 70% conversion after which the pores begin to coalesce. Coalescing would have caused a rapid decrease in available surface area and mass reactivity. This development of internal surface area with reaction is reported by investigators in other reactivity tests [28,61]. However, the small samples used in the TGA experiments conducted here prevented detailed surface examination of the partially oxidized samples.

To determine whether surface structural changes were entirely responsible for the variation in char reactivity during oxidation, the data were fitted to the model of Su and Perlmutter [60,61,62]. Recall from Section 1.5 that a single equation (Equation 1.58) was used to model the change in surface area at any conversion as a function of the initial surface area, pore volume, reaction rate and reactant gas concentration at the external surface of the particle. Assuming that reaction rate changes were due entirely to surface area changes, Equation 1.58 could identically satisfy the observed increase in reactivity.

Bhatia and Perlmutter [60] showed that a particle reacting in the regime of kinetic control could be related to the pore volume and reaction rate by:

$$1 - \chi = \frac{1 - V}{1 - V_i} \left( 1 - \frac{k_c c^n t}{\rho_a R_{P_i}} \right)^3 \quad (3.2)$$

Defining a non-dimensional pore structural parameter,  $\psi = 4\pi L_i(1 - \theta_i)/S_i^2$ ; a particle size parameter,  $\sigma = R_{P_i} S_i/(1 - \theta_i)$ ; and a dimensionless time,  $\tau = k_c c^n S_i t/(1 - \theta_i)$ , Equations 1.58 and 3.2 could be combined and written in the form:

$$\frac{S}{S_i} = \frac{1 - \chi}{(1 - \tau/\sigma)^3} \sqrt[3]{1 - \psi \ln \left[ \frac{1 - \chi}{(1 - \tau/\sigma)^3} \right]} \quad (3.3)$$

The pore structural and particle size parameters,  $\psi$  and  $\sigma$  were calculated from the known pore volume distribution,  $V(r)$  which was used to obtain  $L_i$  and  $S_i$  according to Equations 1.41, 1.42 and 1.43. To calculate the dimensionless time, the values for the reaction rate constant,  $k_c$  and the true reaction order  $n$  needed to be ascertained.

The value of  $n$  was obtained for a single char by measuring the reaction rate at a given temperature over a wide range of oxygen partial pressure. The char was oxidized using a carrier gas of 1, 5, 21 and 100% oxygen in nitrogen. Three reactivity tests at different temperatures were used to calculate the reactivity plot for each of the gas compositions. The data were interpolated to obtain the reactivity of each oxygen partial pressure at a reaction temperature of 625 K. Solving Equation 2.4 for known values of oxygen pressure and reactivity, should give the reaction order,  $n$ . The data were plotted on a log reactivity versus log oxygen pressure where the slope of the line was the reaction order (see Figure 3.5). The data were best fit by a reaction order equal to 0.62 with a correlation coefficient equal to 0.99. This calculated reaction order was in agreement with other published data for TGA reactivity tests [43], however, the value contradicted the presently accepted zero or one-half order reaction expected at low or intermediate temperatures where TGA reactivity tests were conducted (see Equations 1.24-1.26). More research is required to understand the fundamental mechanisms of the carbon-oxygen reaction. Knowing the reaction order, the reaction rate,  $k_c$ , could be calculated knowing that  $\frac{1}{1-x} \frac{dx}{dt} = \frac{k_c c^n}{\rho_a} S_i$  which was easily obtained from experimental TGA

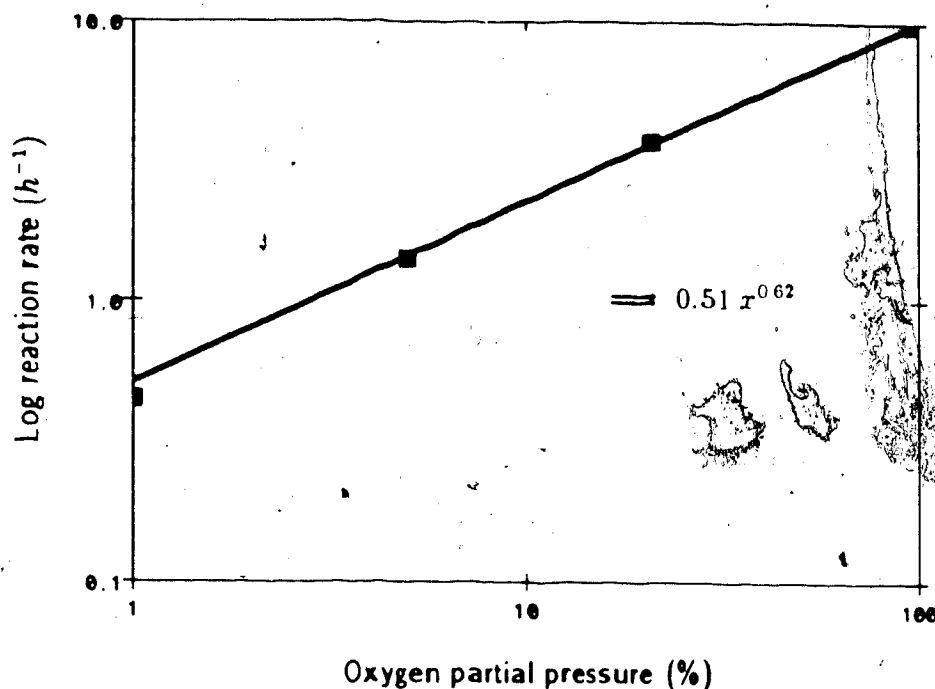


Figure 3.5: Reaction Order for the TGA

data. This information was sufficient to calculate  $\tau$ .

The parameters for the pore structure development model were calculated for chars A to G from surface characterization data and TGA results. This information is shown in Table 3.3. The pore lengths per unit volume calculated from the pore volume distribution data ranged from  $5.6 \times 10^{12}$  to  $14 \times 10^{12} \text{ cm/cm}^3$  for all chars. The calculated surface area per unit volume varied from  $1.7 \times 10^6$  to  $4.3 \times 10^6 \text{ cm}^2/\text{cm}^3$ . The highest values of  $L_v$  and  $S_v$  were only 2.5 times greater than the lowest values. The small variations in  $L_v$  and  $S_v$  were expected since the micropores, which contribute most of the surface area and essentially all of the pore length in coals and chars [62], did not vary by more than a factor of 2.5. The pore structural parameter,  $\psi$ , varied from 5.3 for char A to 10.3 for char E. Chars



Table 3.3: Hydropyrolysis Char Pore Structural Parameters

| Char Type | $L_v \times 10^{-12}$<br>( $\text{cm}/\text{cm}^3$ ) | $S_v \times 10^{-6}$<br>( $\text{cm}^2/\text{cm}^3$ ) | $\psi$ | $\sigma$ | $\tau$ |
|-----------|--|---|--------|----------|--------|
| A         | 14.0   | 4.3   | 5.34   | 37,069   | 5.2    |
| B         | 13.0   | 4.0   | 7.44   | 27,072   | 4.0    |
| C         | 6.6  | 2.1   | 9.22   | 21,875   | 6.2    |
| D         | 7.8  | 2.5   | 8.01   | 25,510   | 6.1    |
| E         | 5.6  | 1.7   | 10.32  | 18,889   | 6.7    |
| F         | 8.2  | 2.6   | 5.61   | 36,111   | 8.3    |
| G         | 8.1  | 2.5   | 5.85   | 33,784   | 8.1    |

with lower  $\text{CO}_2$  surface area tended to have higher values of  $\psi$ .

The ratio  $\tau/\sigma$ , necessary for Equation 3.3, was always very much less than unity even at the longest residence times used during the TGA tests. Therefore, Equation 3.3 could be reduced with little error to:

$$\frac{S}{S_i} = (1 - \chi) \sqrt{1 - \psi \ln(1 - \chi)} \quad (3.4)$$

Where changes in the surface area of the solid were only a function of the conversion,  $\chi$ , and the pore structural parameter,  $\psi$ .

The change in surface area with conversion for a wide range of values of  $\psi$  is shown in Figure 3.6. For  $\psi=0$ , the surface area decreased monotonically with conversion. For  $\psi=100$ , the surface area increases by a factor of 4 at 40% conversion before decreasing as pores coalesced at high conversions. The highest values

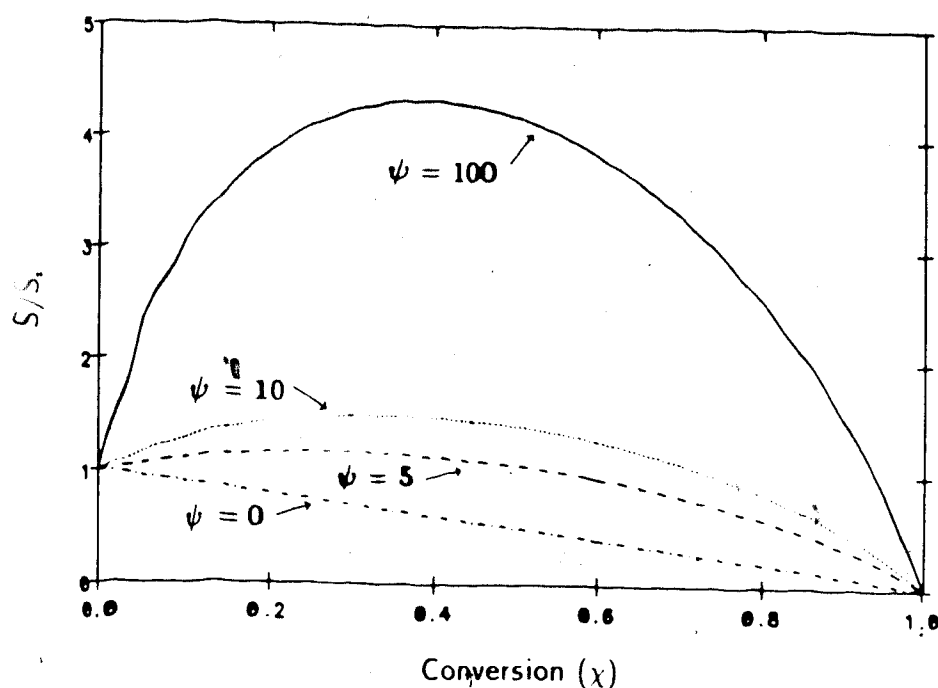


Figure 3.6: Effect of  $\psi$  on Surface Area Change with Conversion

of  $\psi$  were calculated for chars with the smallest micropore surface area. Therefore, chars with a low micropore surface area would tend to have a larger ratio of maximum reactivity to initial reactivity.

The change in surface area with conversion predicted by the Bhatia and Perlmutter model using measured char structural properties was compared to the rate of TGA oxidation for chars A through G. The results are plotted in Figure 3.7. For chars D-G, the change in the theoretical surface area and change in rate of weight loss were similar. Both curves rise to a maximum value between 30 and 40% conversion and decline gradually at higher conversions. The model underpredicts the change in reaction rate by 12 – 30% for chars D-G. However, the chars which had the highest measured increase in rate of weight loss were predicted to have the highest increase according to the model. For chars A-C, the model did

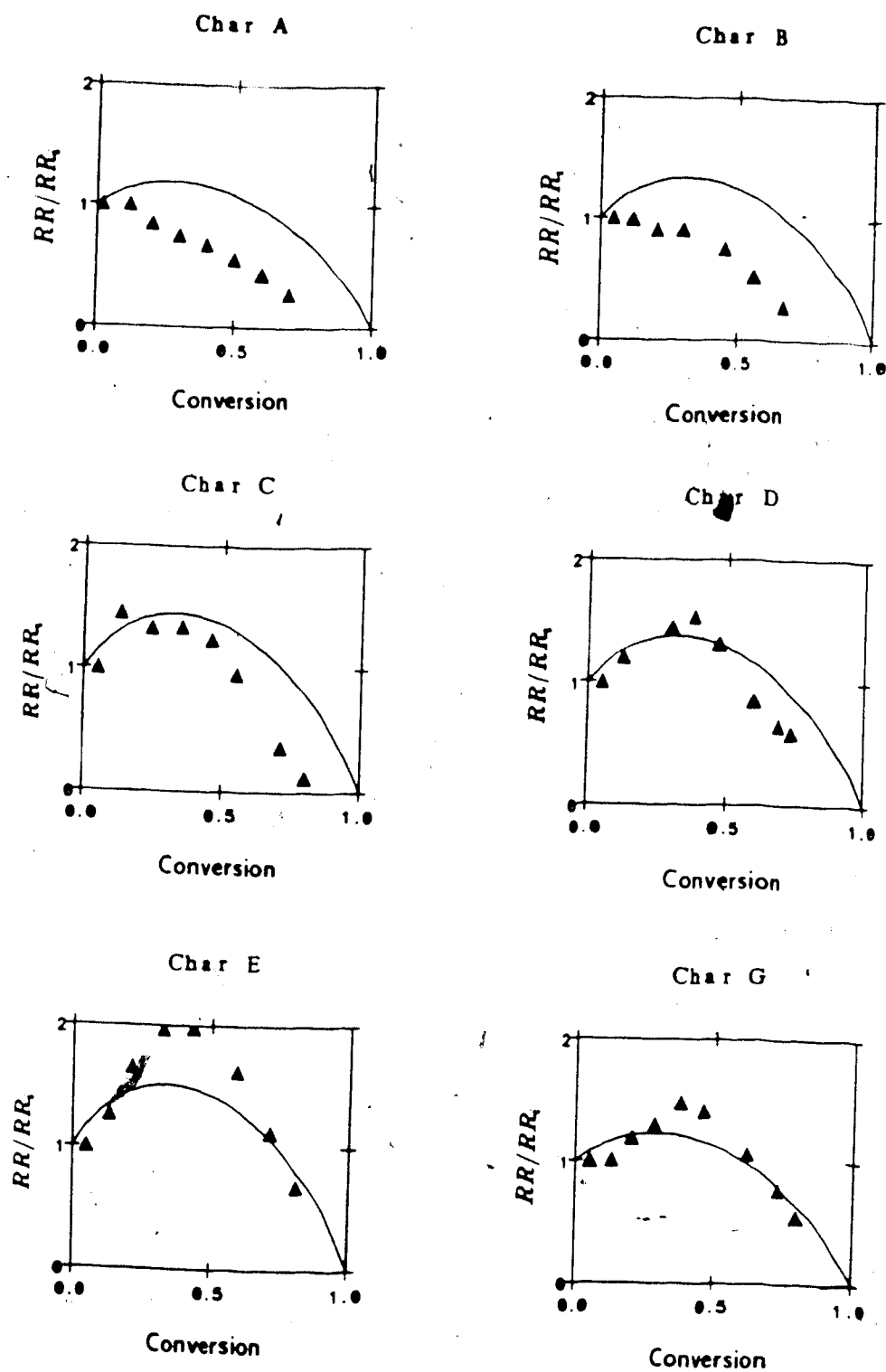


Figure 3.7: Comparison of Char Reaction Rate and Surface Area Development

not fit the data well. These chars had a continuously decreasing rate of weight loss with conversion although the model predicted that the rate should rise 20 - 45%. These chars had a high proportion of volatile matter which could have an oxidation reactivity higher than the non-volatile matter. As reaction proceeded and reactive volatile matter was consumed, the rate of weight loss for chars A-C may have decreased. The pore surface model could not account for this behaviour. Therefore, the change in rate of weight loss during oxidation could be explained by developing pore surface for completely devolatilized chars processed under the most severe hydrolysis conditions. However, the lower severity chars with high volatile matter could not be adequately fitted by the model.

### 3.2.2 Intrinsic Char Chemical Reactivity

The maximum mass reactivity of the chars varied by a factor of ten. These char reactivities were normalized by dividing each char maximum mass reactivity by the coal maximum mass reactivity at a reaction temperature of 625 K. This ratio, defined here as the relative maximum mass reactivity, ( $\overline{RR}_{max}$ ) varied from 0.3 to 2.9.  $\overline{RR}_{max}$  was plotted against char volatile matter content as shown in Figure 3.8. For chars with less than 15% volatile matter,  $\overline{RR}_{max}$  varied within a narrow range from 0.32 to 0.47. For char with more than 15% volatile matter,  $\overline{RR}_{max}$  varied from 1.53 to 2.86.

Having evaluated  $\overline{RR}_{max}$  for the chars, the intrinsic relative reactivity,  $\overline{RR}_i$ , could be calculated by dividing  $\overline{RR}_{max}$  by the total surface area of the char and

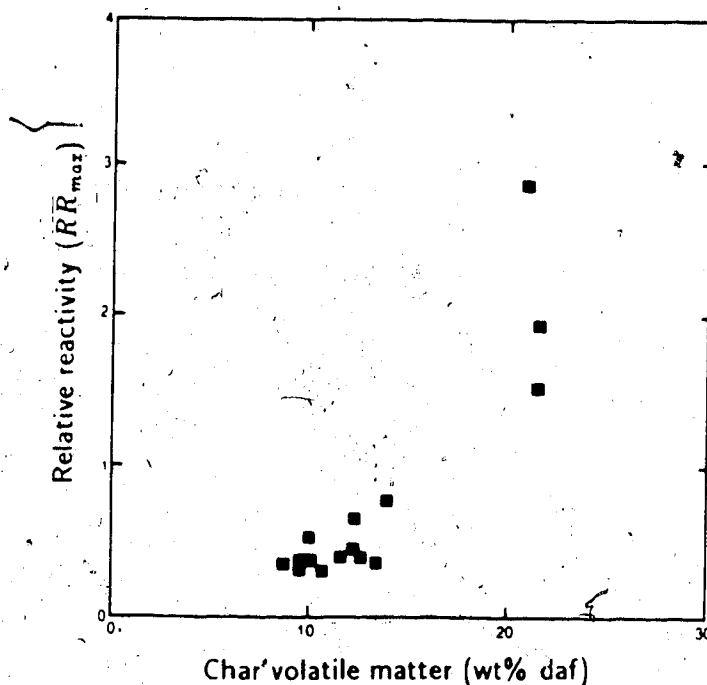


Figure 3.8: Effect of Char Volatile Matter on TGA Relative Reactivity

the partial pressure of oxygen to the power,  $n$  (see Equation 2.5). All of these properties were known from experimental data for chars A-G except the reaction order which was measured at 0.62 for a single char. The intrinsic relative reactivity for chars A-G at a reaction temperature of 625 K is plotted against char volatile matter in Figure 3.9. For chars with 9% volatile matter,  $\overline{RR}_i$  was equal to 0.07. The value of  $\overline{RR}_i$  exceeded 0.6 for chars with more than 20% volatile matter, however, the results were more scattered. This may be due to the wide variation in process conditions for chars with more than 20% volatile matter. The value of  $\overline{RR}_i$  only exceeded unity for char C, produced at the shortest residence time studied (0.5 s). From these results, it is concluded that volatile matter in the char and coal had a higher oxidation reactivity than the fixed carbon by about one order of magnitude. In the case of char C, the rapid removal of a portion of the

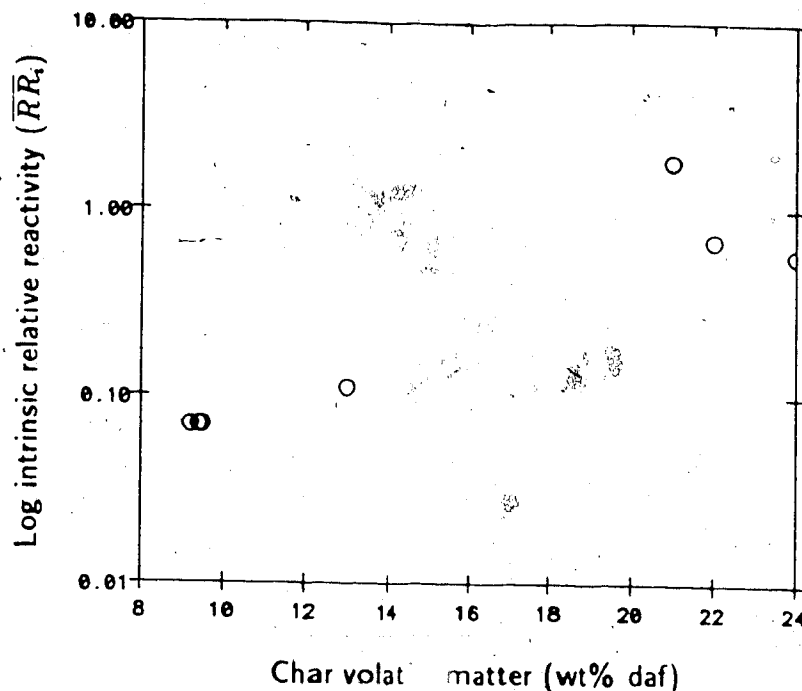


Figure 3.9: Effect of Char Volatile Matter on  $\overline{RR}_i$

volatile matter from the coal in 0.5 s appeared to activate the remaining volatile matter, resulting in  $\overline{RR}_i$  exceeding unity.

For chars A-C, the continuously decreasing rate of weight loss during oxidation probably corresponded to the removal of the most reactive volatile matter. However, the point at which the volatile matter would be completely oxidized was difficult to ascertain from the rate loss plots.

The temperature dependence of the intrinsic rate constant,  $k_c$ , was determined from the expression  $k_c = A_c \exp[-E_c/RT]$  by calculating  $k_c$  at various temperatures. Plotting the logarithm of  $k_c$  versus the inverse temperature gives an Arrhenius plot (see Figure 1.3) with slope proportional to the activation energy,  $E_c$ , and y-intercept equal to the frequency factor,  $A_c$ . The Arrhenius plot for coal and

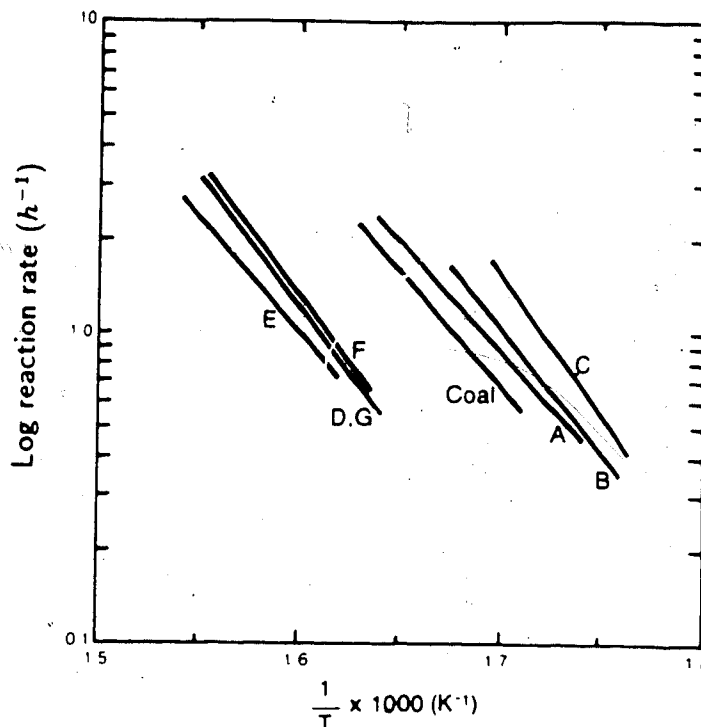


Figure 3.10: Effect of Temperature on TGA Reaction Rates of Chars A-G

chars A-G are shown in Figure 3.10. The activation energy was in the range of 30 – 37 *kcal/mole* for all chars compared to 33 *kcal/mol* for the coal. This activation energy was typical for the oxidation of impure carbons and corresponded to a kinetically controlled reaction [48].

Most of the activation energy calculations were made from curve fitting of two or three points. This resulted in very wide or unmeasurable error bounds in the calculated value of  $E_c$ . To test the accuracy of the three point method and to obtain an activation energy with a high confidence level, 12 TGA runs were conducted on char H which was produced under the most severe hydropyrolysis process conditions. An Arrhenius plot of the results is shown in Figure 3.11. The

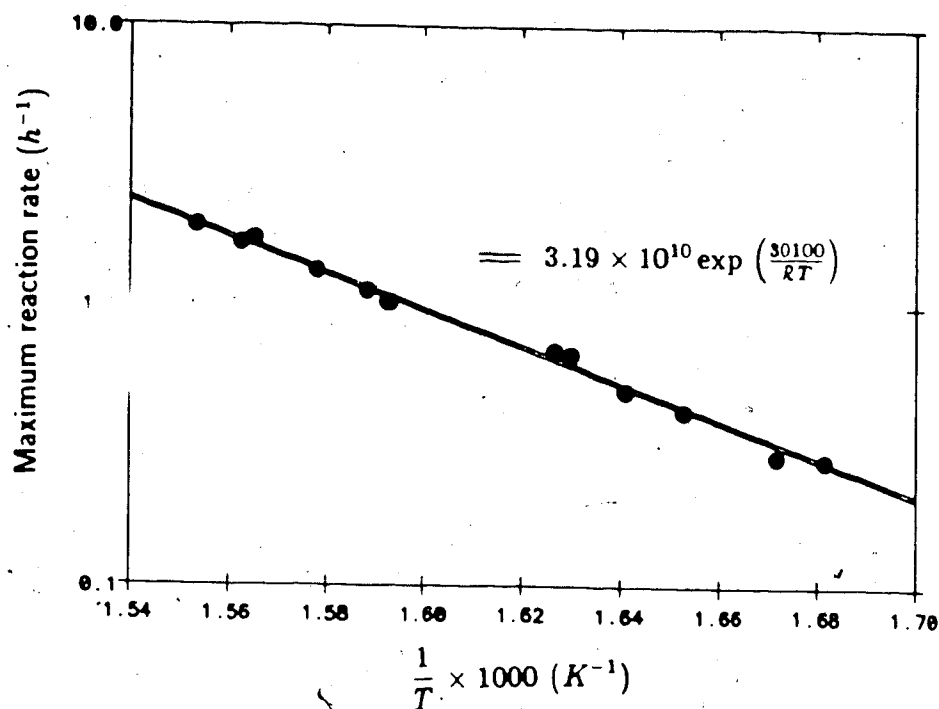


Figure 3.11: Effect of Temperature on TGA Reaction Rate for Char H

R-square coefficient was 0.9988 for the fitted rate equation:

$$RR = 3.19 \times 10^{10} \exp\left(-\frac{30100}{RT}\right) \quad (3.5)$$

The standard deviation on  $E_c$  was  $\pm 900$  and on the frequency factor was  $\pm 2.2 \times 10^{10}$ .

The standard deviation in activation energy was assumed to be the true value for all other TGA tests and was used to calculate error bounds on measured TGA reaction rates from 3 point measurements. The measured activation energy was similar to values reported in the literature for coal chars as summarized by Smith [11].

The measured TGA rates for Alberta subbituminous coal chars were similar to reported TGA reactivities for Occidental subbituminous coal chars by Radovic and Walker [35].



### 3.3 Char Combustibility

The entrained flow combustor (EFC) described in Section 2.3 was used to evaluate the combustibility of hydropyrolysis chars at flame conditions. The chars were mechanically sieved to obtain the  $-140 + 170$  mesh ( $90 - 104 \mu m$ ) fraction in order that particle temperature measurements could be calculated accurately and changes in particle radius with burnout could be measured. The char was fed to the reactor through a water cooled injector at the rate of  $3 \text{ g/hr}$ . The char was entrained in the transport air flowing at  $0.5 \text{ l/min}$  and entered the reactor where it mixed with a large excess of secondary air flowing at  $4.0 \text{ l/min}$ .

Chars B, C, E, G and the parent coal were tested at gas temperature of 1035 and 1335 K, oxygen partial pressure of 9 and 21%, and reactor lengths of 10, 15, 20, 25 and 30 cm corresponding to a residence time of 0.06 to 0.45 s. The burnout versus residence time results for the case of combustion in gas at a temperature of 1035 K are shown in Figure 3.12. In the 9% oxygen atmosphere, the order of decreasing combustibility was char B, C, G, E. Chars B and C had 18% volatile matter content compared to 7% for chars E and G. The high oxidation reactivity of volatile matter, noted in Section 3.2 was probably responsible for the rapid burnout of these chars. A similar order of reactivity was observed for the tests conducted using 21% oxygen as the reactant gas. In this case char C was slightly more reactive than char B.

It was interesting that char E and G, which had very similar volatile matter contents and chemical reactivity had strikingly different behaviour at the higher

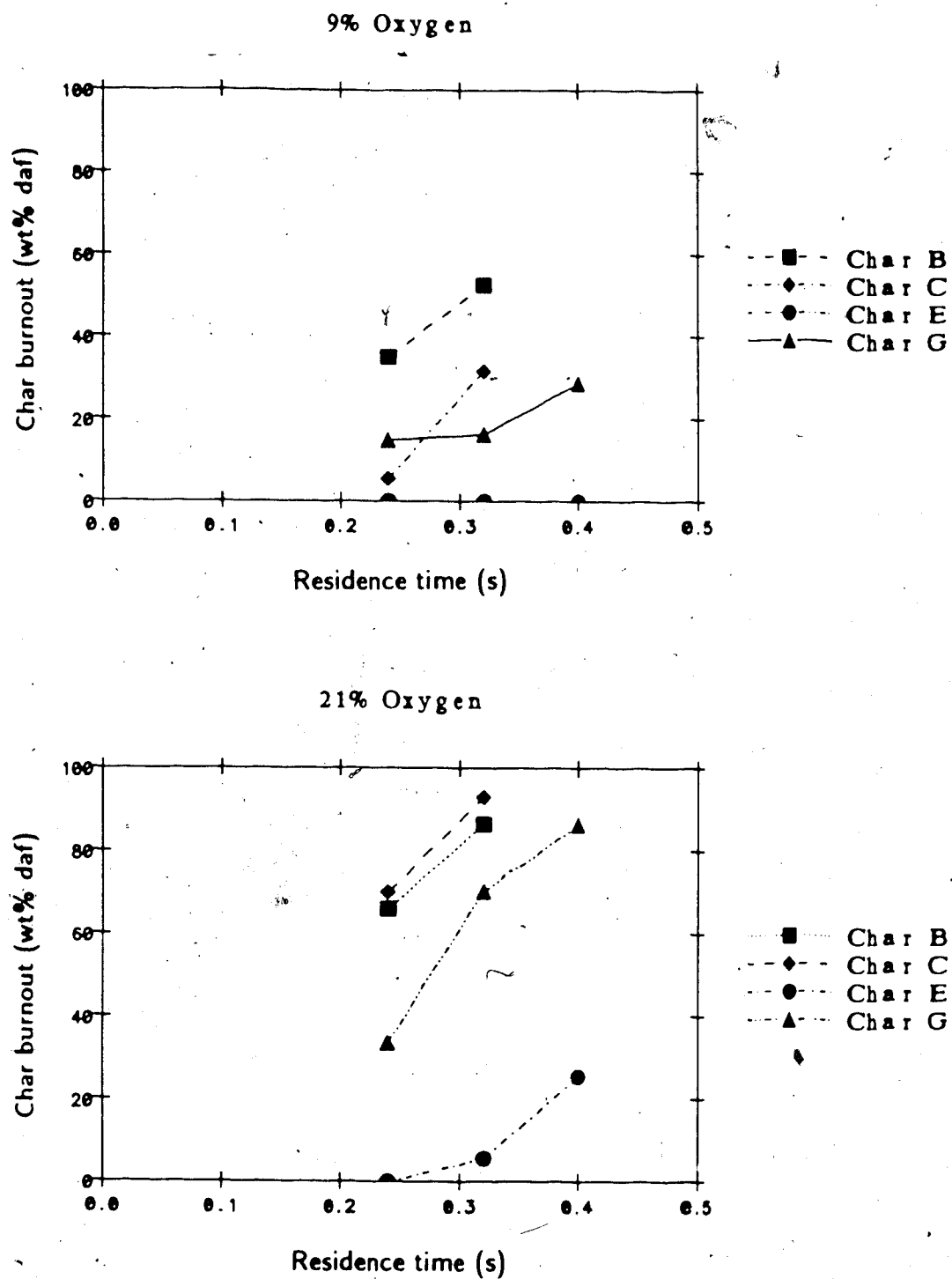


Figure 3.12: Effect of Residence Time on Burnout @ 1035 K on the EFC

temperature used in the EFC. Char E did not burn at all in the 1035 K gas environment with 9% oxygen compared to 21% burnout of char G after 0.32 s. The burnout of char E in a 21% oxygen atmosphere after 0.32 s was only 25% compared to 86% for char G. It was postulated that the pore structure developed during hydropyrolysis may have had a major influence on the discrepancy in combustion rate data for chars E and G. Char E had a lower surface area in the macropores which may have limited the access of oxygen to the interior of the particle. This hypothesis is tested in Section 3.4.

The burnout, versus residence time results for coal and char combustion in gas at a temperature of 1335 K are shown in Figure 3.13. In the 9% oxygen atmosphere, all chars had a lower conversion than the parent coal at any given residence time but the rate of char combustion between 0.06 and 0.3 s equalled or exceeded the rate of coal combustion. The large differences in conversion at 0.06 s were attributed to coal devolatilization. The coal conversion during the first 0.06 s was equal to its volatile matter content. For chars B, C and G, the burnouts at 0.06 s were greater than their volatile matter contents suggesting that heterogeneous reaction of the char was occurring in the first 0.06 s. As was the case at lower temperature, char E had a delayed ignition. Conversion was not detected until the second sampling location after 0.12 s residence time. The delay in combustion of char E at 1335 K gas temperature may also be due to the poorly developed internal char structure. However, once ignited, char E burned at a rate similar to all other chars. Perhaps, the internal-surface developed rapidly as combustion

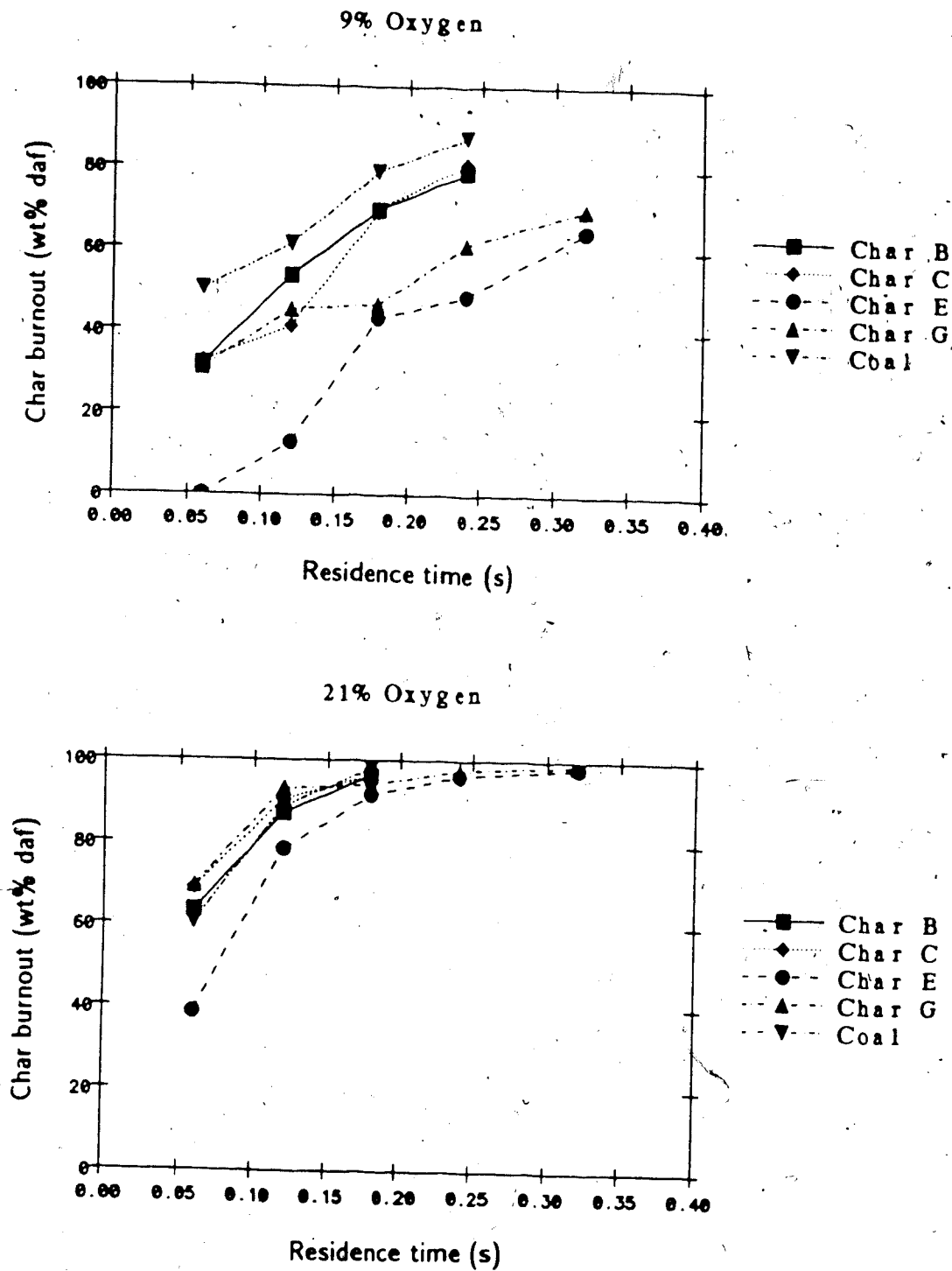


Figure 3.13: Effect of Residence Time on Burnout @ 1335 K on the EFC

proceeded such that all chars would have similar combustion characteristics after ignition. This hypothesis would need to be tested by sampling partially combusted samples from the EFC and characterizing their surface structure.

In the 21% oxygen atmosphere, chars B, C, G and coal had very similar burnout profiles. These fuels were burned out 60 – 70% in the first 0.06 s. This value corresponds to 71% of the bulk diffusion limit of oxygen transport to the particles. This was calculated using Equation 1.27 with the oxygen concentration on the particle surface set equal to zero. At these reactor conditions, a minimum of 43 ms are required to burn out a particle completely. The rapid char burnout suggested that during the early stages of combustion in a utility boiler where 21% oxygen is available, either char or coal would combust at similar rates close to the bulk diffusion limit of oxygen transport. Therefore, both fuels would have similar heat flux profiles and similar flame stability. However, char E burned well away from the bulk diffusion limit as the conversion was only 38% in the first 0.06 s. It was not possible to ascertain from these tests whether the lower combustibility of char E would be significant in a full scale boiler. However, its lower initial combustibility would be a source of concern to boiler designers interested in substituting coal with hydropyrolysis char.

Maximum carbon burnout levels in the coal and chars were correspondingly high. At a gas temperature of 1335 K and oxygen concentration of 21%, the carbon burnout always exceeded 96% in 0.25 s. The burnout of residual carbon in the coal and chars should not be affected by hydropyrolysis conditions since the

combustion process was much more severe. The equivalent burnout rates for coal and char supported this conclusion. Therefore, carbon burnout behaviour in a utility boiler should be similar for the coal and its hydrolysis chars. If carbon burnout was not a problem for the original coal, it should not be a problem for the char.

### 3.4 Comparison of TGA and EFC Results

The effect of surface structure on char combustibility could be evaluated using the surface area and pore volume distribution data. As noted in Section 3.3, surface structure may have had a significant effect on the different reactivities from thermogravimetric analysis (TGA) and entrained flow combustion (EFC) tests.

The macroscopic model described by Equations 1.27-1.39 was used to calculate the reaction rate and effectiveness factor of hydrolysis char particles burning over a wide range of combustion temperature. Three chars (B, D, G) were chosen in the simulation, representative of the full range of hydrolysis test conditions. These three chars were processed at intermediate pressure and residence time and 600, 700 or 800°C, respectively. The value of  $k_c$  used in the Thiele number calculation was extrapolated from TGA data for the three chars according to Equation 3.5 where  $E$ , the activation energy, was set equal to 31,000 cal/mole. This activation energy was an average value for all TGA char reactivity tests. Therefore,  $k_c$  was set by adjusting the preexponential factor,  $A_c$ , to match TGA

data. The values of  $A_c$  for chars B, D and G were 171869, 30967 and 23375  $\text{cm/s}$ , respectively. The factor of six variation in  $A_c$  was due to the wide range in TGA reaction rates for these chars.

### 3.4.1 Average Pore Radius Model

An average value for  $D_e$  and  $S_a$  were also required in Equations 1.36 and 1.39 to calculate char reaction rates. To properly account for the pore structure in determining particle reaction rates, two methods of calculating  $D_e$  and  $S_a$  were tested and compared. First, an average pore radius,  $\bar{r}$ , was calculated according to Equation 1.40. This method has been used extensively by Smith [53,54] and coworkers to evaluate Australian char combustion data. This average pore radius was used in calculations of the effective diffusivity (Equation 1.39) and the Thiele number (Equation 1.37).

The results of this analysis are summarized in Table 3.4 for a particle temperature of 1800 K. The average pore size increased with hydrolysis temperature from 20 Å for char B to 77 Å for char G. Using this value to calculate  $D_e$  resulted in a Thiele number from 1370 for char B to 132 for char G. Although the effectiveness was highest for char G, its burnout rate was only equal to char D and was lower than char B.

The sensitivity of the overall particle reaction rate to chemical reaction rate was tested by assuming a single  $k_c$  for all chars. Assuming that  $A_c$  was equal to 23375  $\text{cm/s}$  for all three chars, then the reaction rate for chars B, D and G

Table 3.4: Calculated Char Reaction Rates Using the Average Pore Size Model

| Char Type | Reaction Rate and Thiele Number |                  |                          |                  |
|-----------|---------------------------------|------------------|--------------------------|------------------|
|           | $A_c = \text{constant}$         |                  | $A_c = \text{TGA value}$ |                  |
|           | Rate<br>( $g/cm^2 s$ )          | Thiele<br>Number | Rate<br>( $g/cm^2 s$ )   | Thiele<br>Number |
| B         | $7.0 \times 10^{-3}$            | 157              | $1.9 \times 10^{-2}$     | 1370             |
| D         | $1.4 \times 10^{-2}$            | 84               | $1.6 \times 10^{-2}$     | 175              |
| G         | $1.7 \times 10^{-2}$            | 88               | $1.7 \times 10^{-2}$     | 132              |

would have been  $7.0 \times 10^{-3}$ ,  $1.4 \times 10^{-2}$  and  $1.7 \times 10^{-2} g/cm^2 s$ , respectively at 1800 K. Therefore, pore size distribution may have a significant effect on reaction rates if the chemical reactivities per unit volume are the same. However, the large differences in chemical reactivity measured at low temperatures influenced the overall calculated reaction rate at flame temperatures.

### 3.4.2 Distributed Pore Size Model

The assumption of an average size for the pores of a coal char did not agree with physical reality. The average pore size model proposed by Wheeler [52] was fairly insensitive to differences in surface area distribution with pore size. Chars with similar total surface areas had widely different pore size distributions, particularly in pores larger than 180 Å in diameter.

To determine the influence of pore surface area distribution on reaction rate, Equation 1.36 was solved incrementally for each pore size. The pore size range



was divided into twenty segments between 5 and 20,000 Å diameter, corresponding to available data from gas adsorption techniques and mercury porosimetry. The effective diffusion coefficient, calculated from Equation 1.29, was solved for each segment using an average pore diameter calculated as the numerical average of the pore size range. The surface area for each pore size range was equal to the incremental change in surface area measured from mercury porosimetry and gas adsorption data. Solving Equation 1.36 for each segment, the total reaction rate was the sum of all reaction rates over the entire pore size range.

$$J_{A_{Kn}} = \sum_{r=0}^{r=r_{max}} J_{A_{Kn}|r \rightarrow \Delta r} \quad (3.6)$$

where  $J_{A_{Kn}}|_r$  refers to mass flux in pores of a given size.

The model was solved first using constant chemical reactivity for all chars. Total reaction rates were calculated over the temperature range from 600 K to 1800 K for chars B, D and G. The reaction rates and effectiveness factors are shown in Figures 3.14 and 3.15 respectively. At temperatures less than 650 K, the Thiele number was less than 1 and the effectiveness factor was greater than 0.98 for all chars. This result supported the conclusion that TGA reactivity data were taken at conditions of chemical control since all TGA data were measured at temperature well below 650 K. As temperature increased above 650 K, the Thiele number and reaction rate increased rapidly. At 1200 K, the Thiele number was 30–50 and the effectiveness factor was only 7–10%. At 1800 K, the Thiele number exceeded 100 and the effectiveness factor was 1–4% for all chars. These Thiele numbers were much different than the values calculated using an average pore

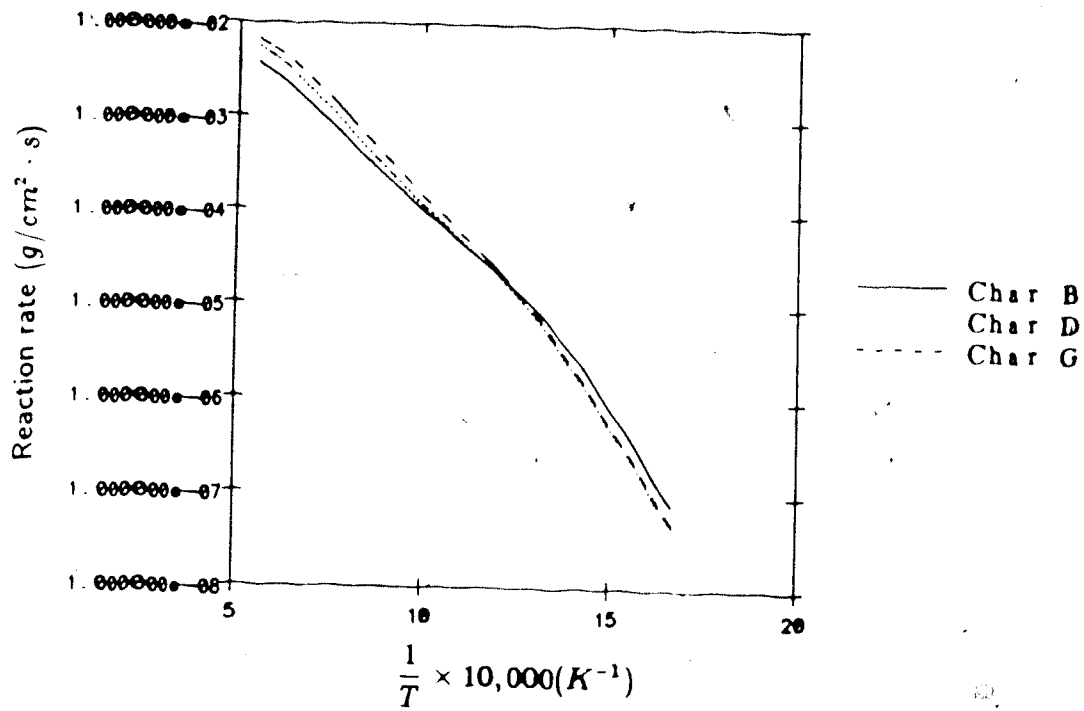


Figure 3.14: Effect of Temperature on Char Reaction Rate with Constant  $A_c$

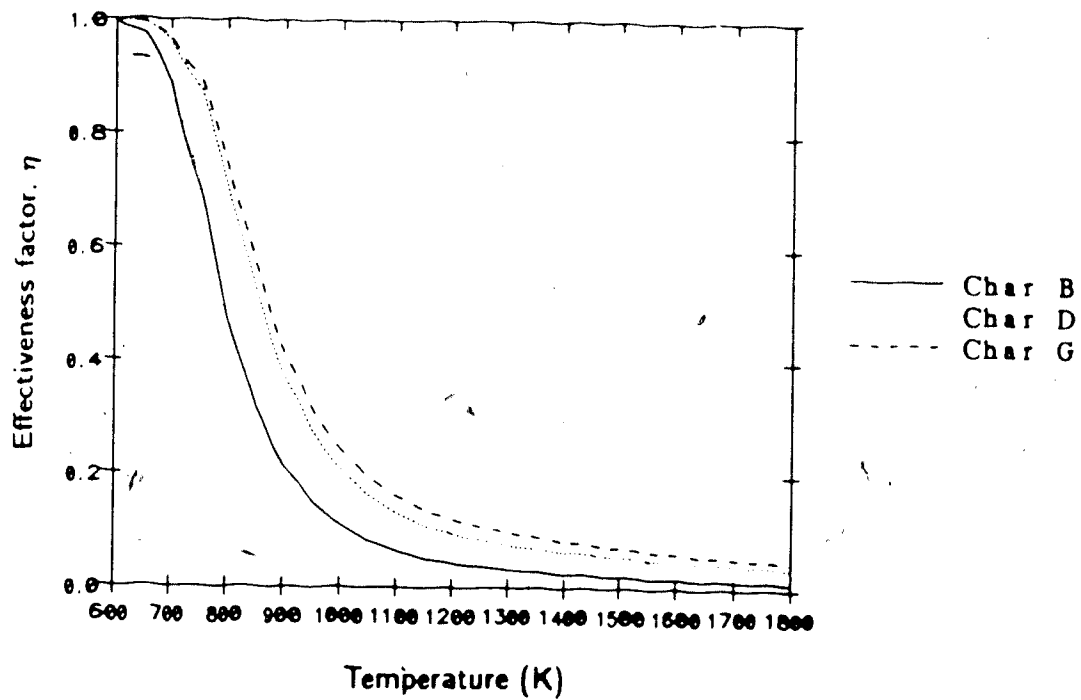


Figure 3.15: Effect of Temperature on Effectiveness Factor with Constant  $A_c$

diameter. Because these chars had a significant surface area in pores larger than 200 Å, the pores were able to contribute to the particle reaction rate at the highest temperature investigated. This was in contrast to the average pore diameter model which was strongly affected by increasing temperature and chemical reactivity. At 1800 K, char B had an overall reaction rate 2.5 times less than char G using the average pore diameter model but the rate was only 1.4 times less using the surface area distribution model. Therefore, surface area in the large pores of all chars tended to increase their calculated reactivity at high reaction temperatures.

The analysis was repeated using the chemical reactivity based on TGA data where the preexponential factors for char B, E and G were 171869, 23505, and 23375  $\text{cm/s}$ , respectively. The total reaction rates of the three chars were calculated for a 90  $\mu\text{m}$  particle diameter and 9% oxygen concentration. The reaction rate and effectiveness factors are shown in Figures 3.16 and 3.17, respectively.

The reaction rate of char B was an order of magnitude greater than all other chars at 600 K but only a factor of 2 and 1.2 at 1200 K and 1800 K respectively. The low surface area of char B was responsible for the decreasing reaction rate with increasing temperature relative to all other coal chars studied. However, the order of magnitude higher chemical reactivity of char B measured on the TGA maintained the calculated reaction rate of char B higher than all other chars. This agreed with the experimental combustion burnout data from the EFC operated at 1325 K gas temperature shown in Figure 3.13. Char B had the most rapid burnout followed by char G and char E. The particle temperatures, calculated from an

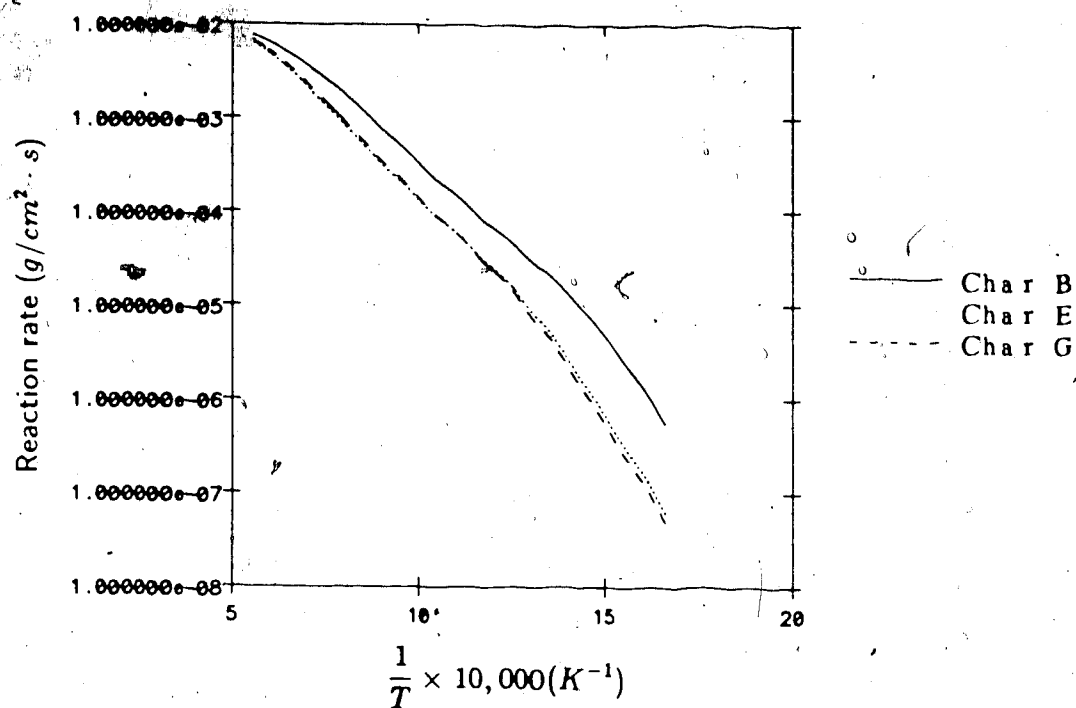


Figure 3.16: Effect of Temperature on Char Reaction Rate with TGA A.

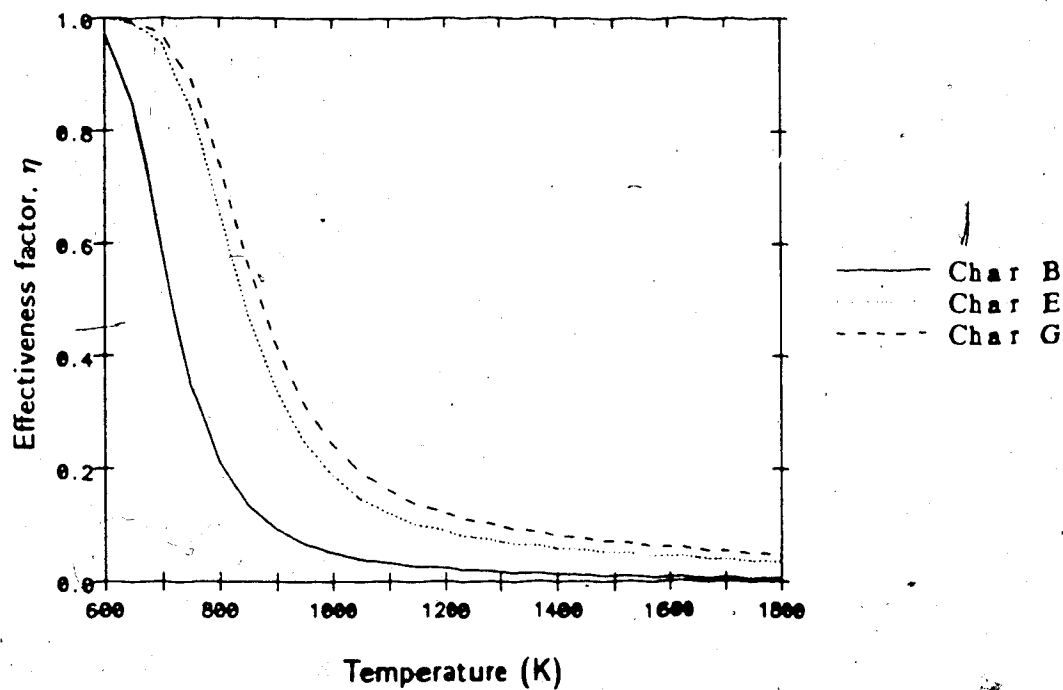


Figure 3.17: Effect of Temperature on Effectiveness Factor with TGA A.

Table 3.5: Comparison of Calculated and Measured Char Combustion Rates

| Char Type | Gas Temperature<br>(K) | Calculated Particle Temp.<br>(K) | Measured Reaction Rate<br>(g/cm <sup>2</sup> s) | Calculated Reaction Rate<br>(g/cm <sup>2</sup> s) |
|-----------|------------------------|----------------------------------|---|---|
| B         | 1150                   | 1400                             | 0.0040  | 0.0035  |
|           | 1390                   | 1600                             | 0.0052  | 0.0057  |
| E         | 1023                   | 1023                             | 0.0000  | 0.0001  |
|           | 1390                   | 1513                             | 0.0029  | 0.0023  |
| G         | 1097                   | 1142                             | 0.0009  | 0.0005  |
|           | 1335                   | 1420                             | 0.0016  | 0.0023  |

energy balance of the burning particles and the measured particle reaction rates per unit external surface area are shown in Table 3.5 for chars B, E and G. The calculated reaction rates from the pore diffusion model are also shown in Table 3.5. Agreement between the predicted and measured particle reaction rates was very good. The percent error was always less than 45% with very close agreement for four of the six tests.

These results highlighted the importance of pore diffusion limitations on the reaction rate of particles studied on the EFC. They also show that chars with a low internal surface structure may still have high overall reaction rates due to high chemical reactivity as measured by TGA and could burn as well as the original coal.

There were no adjustable parameters in the pore diffusion model to predict combustion rates, however, two significant assumptions were necessary; namely, constant pore structure during combustion and acceptability of TGA chemical reaction rates extrapolated using Equation 3.5 to flame temperatures. The sensitivity of combustion rates to pore structure has been described throughout this section. It is probable that significant changes in pore structure would occur during combustion, thereby affecting combustion rates. These changes should be quantified in future research work.

The acceptability of using a chemical reaction rate based on TGA data was dependent on the activation energy measured at 600 K remaining constant up to 1800 K. To test the importance of this assumption, the sensitivity of total reaction rates to chemical activation energy was calculated using the pore diffusion model. The total reaction rates for chars B, E and G were calculated using activation energies of 25,000, 31,000 and 37,000 *cal/mole*. The extreme activation energies were approximately  $\pm 20\%$  of the average  $E_c$  measured on the TGA. The values of  $A_c$  were adjusted to compensate for the variable activation energy so that the chemical reaction rate at 650 K was equal for all three values of  $E_c$ . The values of  $A_c$  for chars B, E and G with  $E_c$  equal to 25,000 *cal/mole* were 1647, 225 and 224 *cm/s*, respectively, and with  $E_c$  equal to 37,000 *cal/mole* were  $17.9 \times 10^6$ ,  $2.45 \times 10^6$  and  $2.44 \times 10^6$  *cm/s*, respectively.

The effect of variable  $E_c$  on total reaction rate for chars B, E and G at a particle temperature of 1500 K is shown in Figure 3.18. Calculated reaction rates

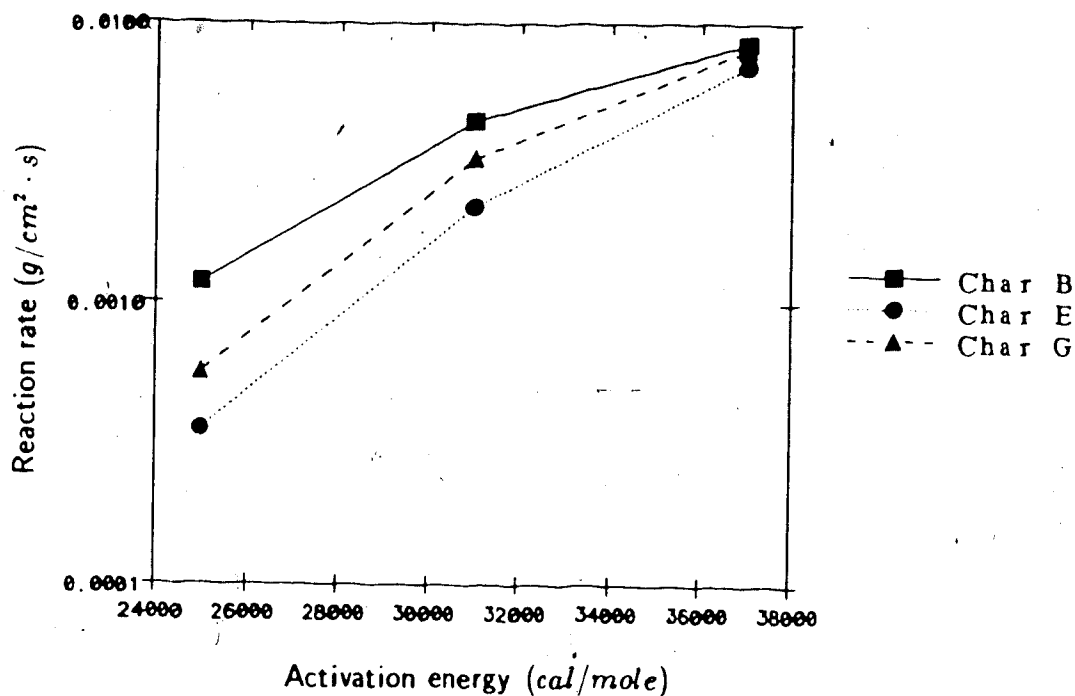


Figure 3.18: Effect of  $E_c$  on Char Reaction Rate at 1500 K

are very sensitive to activation energy. A 20% decrease in assumed activation energy resulted in a 4 – 6 times lower total reaction rate, and a 20% increase in assumed activation energy resulted in a 2 times higher rate at 1500 K particle temperature.

The good agreement between measured and calculated total reaction rates using  $E_c$  equal to 31,000 cal/mole (see Table 3.5) suggests that this is a reasonable estimate up to 1500 K. A 20% variation in assumed activation energy would result in a poorer prediction of measured burning rates.

### 3.5 Comparison with Previous Work

The high combustibility of hydropyrolysis chars generated from Alberta subbituminous coals was similar to earlier results. Subbituminous coal chars combusted by Occidental Research Corporation[30], BYU[9,27], Cogoli[33] and Young[34] were also shown to have high combustibility with no flame stability or carbon burnout problems. However, all previous subbituminous coals were pyrolysed at atmospheric pressure. The present work suggested that process conditions did not have a significant influence on the combustibility.

Although this was true for subbituminous coals, severe process conditions had a detrimental affect on the combustibility of bituminous coals. The thermoplastic behaviour of bituminous coals was probably responsible for the poor combustibility of those chars. Without volatile matter or significant internal surface area, the oxidation would be restricted to the external surface of the bituminous char particles. As suggested in Section 3.4 this would lead to much lower combustion rates.



# Chapter 4

## Conclusions

The following conclusions were made regarding the experimental procedure.

1. A systematic investigation of the physical structure, chemical reactivity and combustibility of hydrolysis chars from Alberta subbituminous coal was completed.
2. A CO<sub>2</sub> and N<sub>2</sub> gas adsorption technique was developed for samples smaller than 1 g and used to measure CO<sub>2</sub> and N<sub>2</sub> surface area of char samples.
3. A technique was developed to measure the chemical reactivity of hydrolysis chars using thermogravimetric analysis.
4. An entrained flow combustor was designed and operated to measure the combustibility of hydrolysis chars at coal flame temperature representative of a utility boiler.

Based on the experimental work completed, the following conclusions on char structure and combustibility may be made.

1. Hydropyrolysis processing had a significant effect on the physical structure of hydropyrolysis chars. Pore volume increased with hydropyrolysis temperature, pressure and residence time. Surface area increased with hydropyrolysis temperature and residence time but decreased with hydropyrolysis pressure.
2. Char intrinsic chemical reactivity was unaffected by hydropyrolysis conditions if the char volatile matter content was less than 10%. However, residual volatile matter in the char had an intrinsic reactivity one order of magnitude higher than the fixed carbon.
3. The combustibility of coal and chars with more than 15% volatile matter or a well developed pore structure was similar.
4. Neither carbon burnout nor flame stability should be a problem for hydropyrolysis chars used as a makeup fuel in a utility boiler. On this basis, it is expected that hydropyrolysis chars generated from Alberta subbituminous coals would be suitable as makeup fuels in a utility boiler.

## Chapter 5

### Recommendations

1. Combustion tests on hydropyrolysis chars should be conducted in a self-supported flame experimental rig with 15% excess air. These tests could be used to test the conclusions made in this report; namely, that the flame stability and carbon burnout of hydropyrolysis chars would be similar to the original coal.
2. Based on the encouraging results of the pore diffusion model it should be incorporated into a global char combustion model. The pore diffusion model should also be refined to account for pore growth and coalescence during particle burnout. This modelling could be supported by measuring the pore structure of partially burned coals and chars.
3. The chemical reactivity of chars at flame temperatures should be investigated to determine whether the activation energy remains constant up to 1800 K. This work would be used to support the pore diffusion model presented here.

## References

- [1] Chakrabartty S.K., du Plessis, M.P. (1981): Coal Pyrolysis: A State of the Art Review; ARC Report YCPY-1, ARC, Edmonton.
- [2] Chambers A.K., Knill K.J., Mendiuk J.J. and Ungarian D.E. (1985): Co-Generation of Electricity and Synthetic Liquids Via Hydropyrolysis of Alberta's Subbituminous Coals; presented at 13th Biennial Lignite Symposium, Bismark N.D.
- [3] Gangwal S.K., Mendiuk J.J. (1983): Flash Pyrolysis/Hydropyrolysis of Alberta Subbituminous Coals: Design, Construction, Operation and Results of a High Pressure 1 - 5 kg/hr Bench Unit; ARC Internal Report No. YCPY-8, November, ARC, Edmonton.
- [4] Box G.E.P. and Behnken D.W. (1960): Some New Three Level Designs for the Study of Quantitative Variables; Technometrics, Vol. 2, pp. 455-475.
- [5] Steam, Its Generation and Use: The Babcock & Wilcox Company, New York, 1975.

- [6] Essenhight R.H. (1982): Char Combustion and Utilization; presented at "Application of Pyrolysis Technology to the Utilization of Eastern Canadian Coals", January 5-6, Fredericton N.B..
- [7] McCann C.R., Demeter J.J., Orning A.A. and Bienstock D. (1971): Combustion of Pulverized Char; Am. Chem. Soc. Div. Fuel Chem. Preprints Vol 15, No. 2., 96-105.
- [8] Demeter J.J. McCann C.R. and Bienstock D. (1973): Further Studies of the Combustion of Pulverized Char and Low-Volatile Coal; presented at the Fuels Division of the ASME, Winter Annual Meeting, November 11-15, Detroit.
- [9] Kramer S.K., Smoot L.D. and Smith P.J. (1985): Combustion Characteristics of Residual Chars; presented at the Fall Meeting, Western States Section, The Combustion Institute, October, Davis CA.
- [10] Walchuk O.R., Bryers R.W. and Bailkin E.P. (1984): A Study of the Fireside Behaviour of Several Coal Pyrolysis Derived Chars and Their Suitability as a Fuel in a conventional Coal Fired Steam Generator; presented at the First Annual Pittsburgh Coal Conference, Sept. 17-21, Pittsburgh.
- [11] Smith I.W. (1978): The Intrinsic Reactivity of Carbons to Oxygen; Fuel, 57, 409-414.
- [12] Pershing D.W. and Wendt J.O.L. (1979): Relative Contributions of Volatile Nitrogen and Char Nitrogen to  $\text{NO}_x$  Emissions from Pulverized Coal Flames; Ind. Eng. Chem. Process Des. Dev., 18, 1, 60-67.

- [13] Pohl J.H. and Sarofim A.F. (1977): Devolatilization and Oxidation of Coal Nitrogen; presented at 16th Symposium (International) on Combustion, the Combustion Institute, Pittsburgh.
- [14] Elliot M.A. and Yohe G.R. (1981): The Coal Industry and Coal Research and Development in Perspective; Ch. 1, in Chemistry of Coal Utilization, ed. M.A. Elliot, John Wiley & Sons, New York.
- [15] Gan H., Nandi S.P. and Walker Jr., P.L. (1972): Nature of the Porosity in American Coals; Fuel, 51, 272-277.
- [16] Mahajan and Walker Jr., P.L. (1978): The Porosity of Coals and Chars, in Analytical Methods for Coal and Coal Products, vol. 1, ed C. Karr Jr., 125-162, Academic Press, New York.
- [17] Adamson A.W. (1982): Capillarity; Ch. 1, in Physical Chemistry of Surfaces, Wiley-Interscience, New York.
- [18] Dacey, J.R. (1965): Gas Adsorption; Ind. Eng. Chem. 57, 27-33.
- [19] Adamson A.W. (1982): Adsorption of Gases and Vapors on Solids; Ch. 13, in Physical Chemistry of Surfaces, Wiley-Interscience, New York.
- [20] Emmett P.H. and Brunauer S. (1937): The Use of Low Temperature van der Waals Adsorption Isotherms in Determining the Surface Area of Iron Synthetic Ammonia Catalysts; J. Am. Chem. Soc., 59, 1553.

- [21] Marsh H. and Siemieniewska T. (1965): The Surface Area of Coals as Estimated from the Adsorption Isotherms of Carbon Dioxide Using the Dubinin-Polanyi Equation; Fuel, 44, 355-367.
- [22] Lamond T.G. and Marsh H. (1964): The Surface Properties of Carbon-II The Effect of Capillary Condensation at Low Relative Pressures Upon the Determination of Surface Area; Carbon, 1, 281-292.
- [23] Dubinin M.M. (1960): The Potential Theory of Adsorption of Gases and Vapors for Adsorbents with Energetically Nonuniform Surfaces; Chem. Rev., 60, 235-241.
- [24] Parkash S., Chakrabartty S.K. and du Plessis M.P. (1984): Porosity in Alberta Subbituminous Coals, Contribution Series No. 95, Alberta Research Council, Edmonton.
- [25] Nsakala N., Walker Jr., P.L., and Essenhigh R.H. (1977): Characteristics of Chars Produced by Pyrolysis Following Rapid Heating of Pulverized Coal, U.S. Department of Energy, FE-2030-TR2, Rep. No. 2.
- [26] Ashu, J.T. and Walker Jr., P.L. (1977): Effects of Heat Treatment Conditions on Reactivity of Chars in Air, U.S. Department of Energy, FE-2030-TR3, Rep. No. 3.
- [27] Wells W.F., Kramer S.K., Smoot L.D. and Blackman A.U. (1985): Reactivity and Combustion of Coal Chars; Presented at 20th Symposium (International) on Combustion, The Combustion Institute, Pittsburgh.

- [28] Johnson J.L. (1975): Relationship Between the Gasification Reactivities of Coal Char and the Physical and Chemical Properties of Coal and Coal Char, Prep., Amer. Chem. Soc. Div. Fuel Chem., 20, 4, 85-101.
- [29] Scotti L.J. et al (1974): The Combustion Performance of COED Char; Energy Research and Development Administration Fossil Energy, Contract No. 14-32-0001-1212, R&D Report No. 73, Interim Report No. 4, Washington.
- [30] Durai-Swamy K., Knell E.W. and Jesse E. (1982): Combustion of Flash Pyrolysis Char; presented at the 1982 Spring Meeting, Western States Section, The Combustion Institute, April, Salt Lake City.
- [31] Young B.C. (1983): Combustion Reactivity of Low Rank Coal Chars; Amer. Chem. Soc., Div. Fuel Chem. Prep. Papers, Vol. 28, 4, August, Washington.
- [32] Hamor R.J. and Young B.C. (1983): Combustion Kinetics of Flash Pyrolysis Chars; Proc. 1983 Int. Conf. on Coal Science, August 15-19, Pittsburgh.
- [33] Edwards J.H., Smith I.W. and Tyler R.J. (1983): The CSIRO Flash Pyrolysis Project. Compendium of Data; Investigation Report-140, Institute of Energy and Earth Resources, CSIRO.
- [34] Cogoli J.G., Gray D. and Essenhigh R.H. (1977): Flame Stabilization of Low Volatile Fuels; Comb. Sci. & Technology, 16, 165-176.
- [35] Radovic L.R. and Walker Jr., P.L. (1984): Reactivities of Chars Obtained in Selected Coal Conversion Processes; Fuel Proc. Tech., 8, 149-154.



- [36] Radovic L.R., Walker Jr., P.L. and Jenkins R.G. (1983): Importance of Carbon Active Sites in the Gasification of Coal Chars; *Fuel*, 62, 849-856.
- [37] Laurendeau N.M. (1978): Heterogeneous Kinetics of Coal Char Gasification and Combustion; *Prog. Energy Combust. Sci.*, 4, 221-270.
- [38] Essenhigh R.H. (1981): Fundamentals of Coal Combustion; in *Chemistry of Coal Utilization*, Ch. 19, ed A.A. Elliot, John Wiley & Sons, New York.
- [39] Dutta S., Wen C.Y. and Belt R.J. (1977): Reactivity of Coal and Char. 1. In Carbon Dioxide Atmosphere; *Ind. Eng. Chem. Process Des. Dev.* Vol. 16, No. 1, 20-27.
- [40] Dutta S., Wen C.Y. (1977): Reactivity of Coal and Char. 2. In Oxygen-Nitrogen Atmosphere; *Ind. Eng. Chem. Process Des. Dev.* Vol. 16, No. 1, 31-37.
- [41] Jenkins R.G. (1981): Gasification Reactivities of Low-Rank Coal Chars; *Proc. of the Low-Rank Coal, Basic Coal Science Workshop*, December 8-9, Houston, Texas.
- [42] Soledade L.E.B., Mahajan O.P. and Walker Jr., P.L. (1978): On the High Reactivity of American Lignite Chars; *Fuel*, 57, 56-57.
- [43] Tseng H.P. and Edgar T.F. (1984): Identification of the Combustion Behaviour of Lignite Char Between 350 and 900°C; *Fuel*, 63, 385-393.

- [44] Blackwood J.D., McCarthy D.J. and Cullis B.D. (1967): Australia J. Chem., 20, 2575 referenced by Tseng H.P. (ref. 43).
- [45] Mahajan O.P., Komatsu M. and Walker Jr., P.L. (1980): Low-temperature Air Oxidation of Coking Coals. 1. Effect on Subsequent Reactivity of Chars Produced; Fuel, 59, 3-10.
- [46] Hengel T.D. and Walker Jr., P.L. (1984): Catalysis of Lignite Char Gasification by Exchangeable Calcium and Magnesium; Fuel, 63, 1214-1220.
- [47] Walker Jr., P.L., Matsumoto S., Hanzawa T., Muira T. and Ismail I.M.K. (1983): Catalysis of Gasification of Coal Derived Cokes and Chars; Fuel, 62, 140-149.
- [48] Radovic L.R., Steczko K., Walker Jr., P.L. and Jenkins R.G. (1985): Combined Effects of Inorganic Constituents and Pyrolysis Conditions on the Gasification Reactivity of Coal Chars; Fuel Proc. Tech., 10, 311-326.
- [49] Satterfield C.N. (1970): Mass Transfer in Heterogeneous Catalysts, MIT Press, Cambridge.
- [50] Walker Jr., P.L. (1980): Pore System In Coal Chars. Implications for Diffusion Parameters and Gasification; Fuel, 50, 809-810.
- [51] Walker Jr., P.L., Austin L.G. and Nandi S.P. (1966): "Activated Diffusion of Gases in Molecular Sieve Materials"; Chemistry and Physics of Carbon, 2, 257-371, Marcel Dekker, New York.

- [52] Wheeler A. (1953): Reaction Rates and Selectivity in Catalyst Pores; Adv. Catal., 3, 249.
- [53] Smith I.W. and Tyler R.J. (1972): Internal Burning of Pulverized Semi-Anthracite: the Relation Between Particle Structure and Reactivity; Fuel, 51, 312-321.
- [54] Smith I.W. and Tyler R.J. (1974): The Reactivity of a Porous Brown Coal Char to Oxygen between 630 and 1812.K; Comb. Sci. & Tech., 9, 87-94.
- [55] Mehta B.N. and Aris R. (1971): Communications on the Theory of Diffusion and Reaction-VII The Isothermal nth Order Reaction; Chem. Eng. Sci., 26, 1699-1712.
- [56] Simons G.A. and Finson M.L. (1979): The Structure of Coal Char: Part 1. Pore Branching; Comb. Sci. Tech., 19, 217-225.
- [57] Simons G.A. (1979): The Structure of Coal Char: Part II. Pore Combination; Comb. Sci. Tech., 19, 227-235.
- [58] Simons G.A. (1979): Char Gasification: Part 1. Transport Model; Comb. Sci. Tech., 20, 107-116.
- [59] Lewis P.F. and Simons G.A. (1979): Char Gasification: Part II. Oxidation Results; Comb. Sci. Tech., 20, 117-124.
- [60] Bhatia S.K. and Perlmutter D.D. (1980): A Random Pore Model for Fluid-Solid Reactions: I. Isothermal, Kinetic Control; AIChE Journal, 26, 3, 379.

- [61] Su J. and Perlmutter D.D. (1984): Evolution of Pore Volume Distribution During Gasification; *AIChE Journal*, 30, 6, 967-973.
- [62] Su J. and Perlmutter D.D. (1985): Effect of Pore Structure on Char Oxidation Kinetics; *AIChE Journal*, 31, 6, 973-981.
- [63] Srinivas B. and Amundson N.R. (1981): Intraparticle Effects in Char Combustion. III Transient Studies; *Can. Journal Chem. Eng.*, 59, 728-738.
- [64] Gavalas G.R. (1980): A Random Capillary Model with Application to Char Gasification at Chemically Controlled Rates; *AIChE Journal*, 26, 4, 577-585.
- [65] Gavalas G.R. (1981): Analysis of Char Combustion Including the Effect of Pore Enlargement; *Comb. Sci. Tech.*, 24, 197-210.
- [66] Hashimoto K. and Silveston P.L. (1973): Gasification: Part 1. Isothermal, Kinetic Control Model for a Solid with a Pore Size Distribution; *AIChE Journal*, 19, 2, 259-277.
- [67] Nelsen F.M. and Eggertsen F.T. (1958): Determination of Surface Area. Adsorption Measurements by a Continuous Flow Method; *Anal. Chem.*, 30, 1387-1390.
- [68] Haley A.J. (1963): An Extension of the Nelsen-Eggertsen Continuous Flow Method of Surface Area Measurement; *J. Appl. Chem.* 13, 392-399.
- [69] Rootare H.M. (1970): A Review of Mercury Porosimetry; in *Advanced Experimental Techniques in Powder Metallurgy*, 225-252, Plenum Press, New

York.

- [70] Knill K.J., Mendiuk J.J. and Chakrabartty S. (1983): Laboratory Evaluation of the Flash Pyrolytic Properties of Alberta Subbituminous Coal; presented at 33rd Canadian Chemical Engineers Conference, October 3-5, Toronto.
- [71] Field M.A. (1969): Rate of Combustion of Size-Graded Fractions of Char from a Low-Rank Coal Between 1200 K and 2000 K; Combustion and Flame, 13, 237-252.
- [72] Field M.A. (1970): Measurements of the Effect of Rank on Combustion Rates of Pulverized Coal; Combustion and Flame, 14, 237-248.
- [73] Nsakala N.Y., Patel R.L. and Lao T.C. (1982): Combustion and Gasification Characteristics of Chars from Four Commercial Significant Coals of Different Rank, EPRI Rep. No. AP-2601, Final Report.
- [74] Winship D. (1986): Vice President Research, Combustion Engineering Canada, Personal Communication.
- [75] Land T. and Barber R. (1956): Suction Pyrometers in Theory and Practice; J. Iron and Steel Inst., November, 269-273.
- [76] Smoot L.D., Hedman P.O., Smith P.J. and Blackham A.U. (1982): Combustion Processes in a Pulverized-Coal Combustor; EPRI CS-2490, Volume 1, Project 364-2, Final Report, July.

- [77] Cypres R., Planchon D. and Braekman-Danheux C. (1985): Evolution of Pore Structure and Active Surface Areas of Coal and Char During Hydrogenation; Fuel, 64, 1375-1378.
- [78] Jenkins R.G., Nandi P.L. and Walker P.L. Jr. (1973): Reactivity of Heat-Treated Coals in Air at 500°C; Fuel, 52, 288-293.
- [79] Knill K.J., Chambers A.K., Gangwal S.K. and Mendiuk J.J. (1984): Laboratory Evaluation on Pyrolysis Properties of Alberta Thermal Coal Regions, Alberta Research Council Report YCPY-12, Edmonton.
- [80] Walker, Jr. P.L., Austin L.G. and Nandi S.P. (1966): Activated Diffusion of Gases in Molecular Sieve Materials; in Chemistry and Physics of Carbon, ed. P.L. Walker Jr., 2, 257-371, Dekker, New York.

## Appendix A

# Statistical Analysis of Nitrogen Surface Area Technique

The nitrogen surface area technique was calibrated by running five different primary surface area standards supplied by Quantachrome Corp.. The standards had surface areas of 2.63, 7.44, 49.1, 109 and 233  $m^2/g$ . This range in surface area covered the expected range in surface area of hydrolysis chars. Twenty-three surface area measurements were made and the comparison between true and measured surface areas was shown in Figure 2.6.

The data were fitted using linear regression according to the Equation:

$$S_{N_2} = A \cdot S_{N_2} + B \quad (A.1)$$

where the coefficients, A and B, were adjusted. The final values for the coefficients are shown in Table A.1. The slope of the line was one standard deviation less than unity. The y-intercept was very close to zero. This value should equal

Table A.1: Statistical Parameters of the Surface Area Test

| Coeff. | Final Values | Standard Error | T Value | Significance Level |
|--------|--------------|----------------|---------|--------------------|
| A      | -0.985       | 0.014          | 67.99   | 0.0001             |
| B      | -0.240       | 1.195          | -0.20   | 0.8428             |

Table A.2: ANOVA Table for Surface Area Test

| Source | Sum of Squares | D.F. | Mean Square | F Value | Multiple $R^2$ |
|--------|----------------|------|-------------|---------|----------------|
| Reg.   | 89401          | 1    | 89401       | 4622    | 0.995          |
| Res.   | 406            | 21   | 19          |         |                |

zero since the line should pass through the origin. The t-value for this parameter was so low (0.2) that the significance level of the y-intercept was 0.84 and therefore, it could be neglected in the Equation.

The significance of the linear fit was very high as shown by the F value in Table A.2. For 21 degrees of freedom on the residual and one degree of freedom on the regression, the F value was 4622 corresponding to a significance level of 0.0001. The  $R^2$  regression value was 0.995 which also indicated a very good fit to the data. The residuals were plotted against the true surface area to determine whether there was systematic error in the surface area measurements. As shown in Figure A.1, the residuals were sufficiently scattered to suggest that systematic



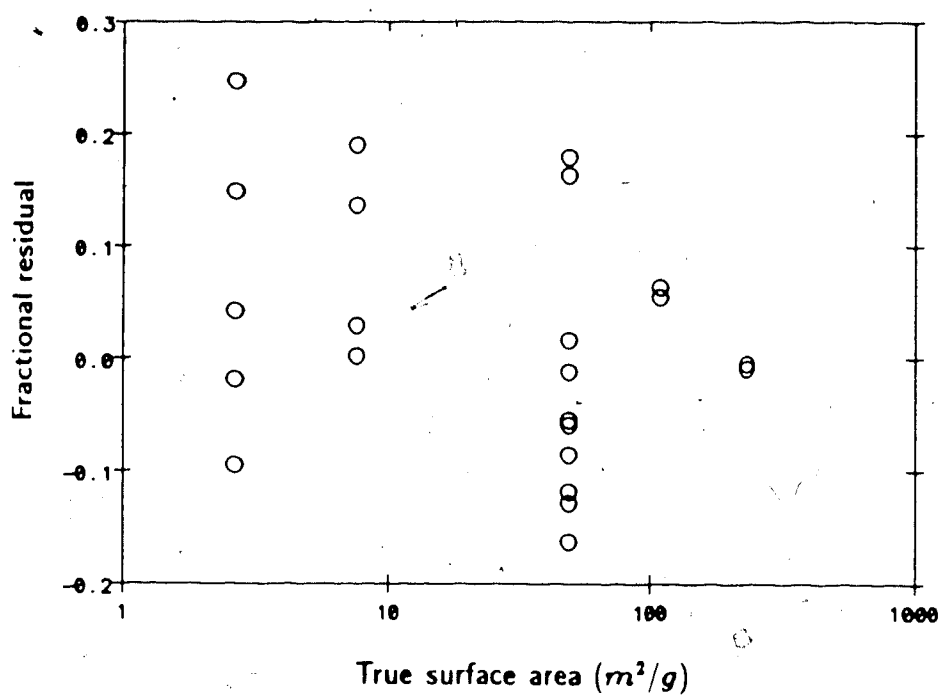


Figure A.1: Residual Plot for the Surface Area Test

error could be ignored.

## Appendix B

# Oxidant Diffusion Limitations in the TGA

The limiting rate of oxygen diffusion to a char sample contained in a pan on the arm of the thermogravimetric analyser was approximated to determine whether the limit in rate of oxidation observed on the TGA was diffusion controlled. The rate of diffusion was modelled assuming that oxygen (A) diffused into the sample and carbon monoxide (B) was the major product. Therefore, the molar flux of A,  $Q_A$ , was one-half the molar flux of B,  $Q_B$ . The sample temperature was assumed to be 950 K with an oxygen concentration in the free stream of 21%.

The rate of reactant diffusion,  $Q_A$ , was given by:

$$Q_A = -\frac{1}{2} Q_B \quad (\text{B.1})$$

$$= -c_T D_{AB} \frac{dx_A}{dz} - x_A(Q_A - Q_B) \quad (\text{B.2})$$

$$= -\frac{c_T D_{AB}}{1 - x_A} \frac{dx_A}{dz} \quad (\text{B.3})$$

where  $c_T$  was the total concentration of gas in the free stream and  $x_A$  was the fraction of oxygen in the gas phase. At any given distance above the particle surface,  $Q_A = \text{constant}$  so that:

$$\frac{d}{dz} \left( \frac{c_T D_{AB}}{1 + x_A} \frac{dx_A}{dz} \right) = 0 \quad (\text{B.4})$$

Assuming that  $c_T D_{AB}$  was independent of  $z$ , Equation B.4 was integrated twice to obtain:

$$\ln(1 + x_A) = C_1 z + C_2 \quad (\text{B.5})$$

with the boundary conditions:

$$\begin{aligned} \text{at } z = \delta & : x_A = x_{A,\infty} \\ \text{at } z = 0 & : x_A = 0 \end{aligned} \quad (\text{B.6})$$

Solving Equation B.5 with the boundary conditions gave:

$$\ln(1 + x_A) = \ln(1 + x_{A,\infty}) \frac{z}{\delta} \quad (\text{B.7})$$

Differentiating Equation B.7 and applying the definition for mass flux (Equation B.3) gave:

$$Q_A|_{z=0} = -\frac{c_T D_{AB}}{\delta} \ln(1 + x_{A,\infty}) \quad (\text{B.8})$$

At a gas temperature of 950 K the binary diffusivity of oxygen in carbon monoxide was equal to  $1.94 \times 10^{-5} \text{ gmol/cm} \cdot \text{s}$ . Assuming a boundary layer above the sample of 5 mm, the mass flux was equal to:

$$Q_A|_{z=0} = -3.86 \times 10^{-5} \ln(1 + x_{A,\infty}) \quad (\text{B.9})$$

During initial TGA experiments, the flowrate of air was maintained at 70 ml/min.

Therefore, the total molar flowrate of oxygen,  $Q_{A_T}$ , was  $8.4 \times 10^{-6} \text{ gmol/s}$ . The

mole fraction of oxygen in the gas stream was given by:

$$x_{A_{\infty}} = \frac{Q_{A_T}}{4.76Q_{A_T} + Q_{B_T}} = \frac{Q_{A_T}}{4.76Q_{A_T} + 2Q_A S} \quad (B.10)$$

where  $Q_{B_T}$  was the total molar flowrate of product and  $S$  was the cross-sectional area of the sample pan. Solving Equation B.9 gave the maximum possible mass flow to the surface:

$$Q_{A|_{z=0}} = 5.9 \times 10^{-6} \frac{\text{gmol}}{\text{cm}^2 \cdot \text{s}} \quad (B.11)$$

For a pan size of 3 mm radius, the diffusion rate was related to the carbon oxidation rate by the molecular weight of carbon,  $M_C$ , according to:

$$\dot{m}_C = M_C \cdot S \cdot Q_A \quad (B.12)$$

$$= 1.2 \text{ mg/min} \quad (B.13)$$

This calculated maximum carbon oxidation rate according to diffusion limitations, was within a factor of two of the measured maximum oxidation rate equal to 1.9 mg/min (see Figure 2.10). Therefore, it was concluded that the sample oxidation rate was limited by diffusion of oxygen to the sample.

## Appendix C

### Surface Characterization Data

Results of the surface characterization of seven hydrolysis chars representative of the full range of hydrolysis conditions are contained in this Appendix. The results for all nitrogen and carbon monoxide surface areas are given in Table C.1 and for the mercury porosimetry test are given in Tables C.2-C.9.

The mercury porosimetry measurements were made at PetroCanada laboratories in Calgary to which the Author is thankful. There is an error in the calculation of surface area in the mercury porosimetry data sheets. All surface area measurements should be multiplied by the sample weight to obtain the true surface areas of the chars. This problem in the software was later rectified.

Table C.1: Nitrogen and Carbon Dioxide Surface Area Measurements

| Char<br>Type | Surface Area                              |  |
|--------------|---|--|
|              | N <sub>2</sub><br>(m <sup>2</sup> /g daf) | CO <sub>2</sub><br>(m <sup>2</sup> /g daf) |
| A            | 16.7                                      | 435 ± 47                                   |
| B            | 4.2                                       | 332 ± 30                                   |
| C            | 22.0                                      | 269 ± 16                                   |
| D            | 13.7                                      | 317 ± 41                                   |
|              | 12.4                                      |  |
| E            | 10.2                                      | 237 ± 24                                   |
|              | 8.9                                       |  |
|              | 12.3                                      |  |
| F            | 34.0                                      | 427 ± 20                                   |
|              | 35.0                                      |  |
|              | 31.9                                      |  |
| G            | 28.7                                      | 405 ± 49                                   |
|              | 27.2                                      |  |

PAGES 146 -.153 have been removed due to  
unavallability of copies of acceptable  
print quality. These pages included  
Tables C.2 to C.9 inclusive.